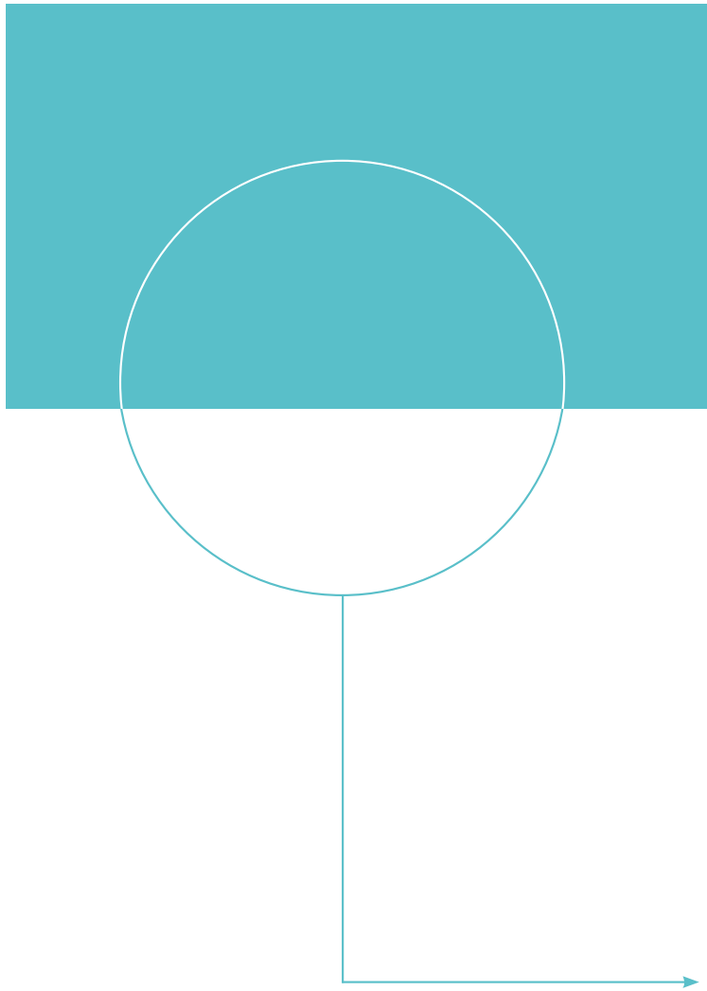

Master's thesis

2020

Daniel Ricardo Coronel Alvarez

NTNU
Norwegian University of
Science and Technology
Faculty of Engineering
Department of Geoscience and Petroleum

Daniel Ricardo Coronel Alvarez

AvO modelling constrained by burial history as an anomaly screening tool in complex geological settings

August 2020

NTNU
Norwegian University of
Science and Technology

NTNU
Norwegian University of
Science and Technology

NTNU

Norwegian University of
Science and Technology

AvO modelling constrained by burial history as an anomaly screening tool in complex geological settings

Daniel Ricardo Coronel Alvarez

Petroleum Geosciences
Submission date: August 2020
Supervisor: Per Åge Avseth

Norwegian University of Science and Technology
Department of Geoscience and Petroleum

Summary

AvO technology has been recognized to be profoundly affected by burial history because the rocks that composed the medium have recorded the different events and processes in their structure; thus, these events are recorded in the physical properties of the rocks. In the specific case of areas with complex basin development, the knowledge of their burial history provides a way to constrain the interpretation and prediction of the AvO signatures. Recent studies have aimed to integrate the general geological knowledge about the burial history with rock-physics modelling to improve the understanding of the rock properties and their effect on the wave propagation. In this work, we show how such integration can result in a powerful tool to explore the possible scenarios and their associated uncertainties, especially in unexplored areas. We show the influence that the burial history has on the sandstone and shale properties; the impact that different context for constructing shale trends have on shale properties estimation and the effect that the uplift estimation and its deviation have on the expected sandstone properties spatially. We have demonstrated that an integrated methodology allows us to describe, explore and analyze distinct geological scenarios that honour the basin evolution providing a sensitivity analysis for the different controlling factors of the AvO responses for a given basin. We have applied this methodology in the southwestern Barents Sea, showing the potential for prediction and screening of untested AvO signatures. Furthermore, the application of this methodology can be beneficial during risk assessments workflows for petroleum prospects.

Sammendrag

AvO-teknologi har blitt anerkjent for å være sterkt påvirket av begravningshistorie. Siden bergartene som bygger opp mediet har registrert de forskjellige hendelsene og prosessene i strukturen sin, blir disse hendelsene registrert i de fysiske egenskapene til bergartene. I det spesifikke tilfellet ved områder med kompleks bassengutvikling, gir kunnskapen om deres begravningshistorie en måte å begrense tolkningen og prediksjonen av AvO-signaturene. Noen nye studier har som mål å integrere den generelle geologiske kunnskapen om begravningshistorien med modellering av formasjonsfysikk for å bedre forståelsen av bergartsegenskaper og deres effekt på bølgeforplantning. I dette arbeidet viser vi hvordan en slik integrering kan resultere i et kraftig verktøy for å utforske de mulige scenariene og tilhørende usikkerhetsmomenter, spesielt i uutforskede områder. Vi viser innflytelsen som begravningshistorien har på sandsteins- og skiferegenskapene; innvirkningen som forskjellig kontekst for konstruksjon av skifertrender har på skiferegenskapsestimering og effekten som landhevings-estimater og tilhørende avvik har på de forventede sandsteinsegenskapene romlig. Vi har vist at en integrert metodikk gjør det mulig for oss å beskrive, utforske og analysere distinkte geologiske scenarier som tar bassengutviklingen i betraktning og gir en følsomhetsanalyse for de kontrollerende faktorene i AvO-respons for et gitt basseng. Vi har brukt denne metodikken i det sørvestlige Barentshavet, og viser potensialet for prediksjon og screening av uutprøvde AvO-signaturer. Videre kan anvendelsen av denne metodikken være fordelaktig under risikovurderingen av petroleumsprospekter.

Acknowledgement

I want to thank NTNU for giving me the opportunity, guidance, and tools to help me build my professional path.

I would also like to thank my supervisor Per Åge Avseth for the insightful guidance, advice, feedback and long discussions during this project. It has been a very fruitful and fulfilling time where I have gained experience through discussions. Also, I would like to thank TGS for providing the seismic and AvO data, and to the Norwegian Petroleum Directorate for providing the well data. I also want to thank Kenneth Duffaut for being always open to discussions.

I would like to thank professors Kenneth Duffaut, Andrew Carter, Arve Naess, Rune Holt and Alexey Stovas for sharing their knowledge and experience during my time at NTNU.

Finally, I would like to thank my family, my girlfriend, and my friends for always being a source of motivation and my support during my studies.

Contents

List of Tables

List of Figures

Chapter 1

Introduction

The AVO technology has been used widely in the Oil and Gas industry as a seismic assessment tool both in exploration and production of hydrocarbons. Its widespread use and popularity because the seismic amplitudes are explained in terms of physical properties. However, many factors influence the seismic reflections making AvO a non-unique problem where lithology, fluid, tuning and overburden effects that control the AvO signatures at different degrees. The significance and variations of these factors are tightly related to geological history. Acknowledging and understanding them is an essential part when interpreting the observed data and subsequent decision making based on AVO signatures.

The present-day rock properties are the result and expression of the rock evolution throughout the geological time; they record in their structure the events and conditions to which they have been exposed, including changes in mechanical and chemical nature. Rock-physics methodologies have become a bridge between the rocks and the seismic behaviour by linking information from different sources and scales (well log data, core measurements, thin sections, XRD, among others); where different physical models that include such geological constraints and assumptions about the rock microstructure and their relationship with the seismic signatures (Avseth et al., 2005). In complex geological areas, burial history constraints become especially important. Several studies have recognized the effect that diagenesis, uplift and erosion have on the properties of the sediments which influence directly wave propagation and seismic velocities (Storvoll et al., 2005; Avseth and Dræge, 2012; Dræge et al., 2014; Avseth and Lehocki, 2016; Baig et al., 2016).

In a burial history-constrained rock-physics framework, it is essential to model the diagenesis evolution and its associated porosity reduction. Walderhaug (1996) described mathematically the quartz cementation rate and resulting porosity reduction in sandstones as a function of temperature over time due to quartz precipitation. The model is also dependent on a different texture and mineralogical characteristics, such as grain diameter (surface area), clay coating and the fraction of quartz. Later, Lander and Walderhaug (1999) described a method to predict porosity by modelling both mechanical compaction and cementation. In a later work, Helset et al. (2004) introduced a diagenetic porosity loss model including both mechanical and chemical compaction and linked it to the rock-physics modelling using contact theory models proposed by (Dvorkin and Nur, 1996). Further studies demonstrated the importance of honoring the temperature and stress history, and how a joint diagenetic-rock-physics modelling can improve the understanding of the rock properties and seismic signatures (Avseth and Dræge, 2012; Dræge et al., 2014;

Avseth and Lehocki, 2016).

In this sense, this study aims to integrate uplift estimations to build a burial history-constrained rock-physics framework for reservoir properties and AvO signatures screening in the Southwestern Barents Sea. The Barents Sea represents an excellent example for complex basin development, where different uplift episodes have occurred, especially during the Cenozoic, affecting the hydrocarbon prospectivity. Doré et al. (2002) recognized the exhumation characteristics present in the hydrocarbon systems in the Barents Sea. Different authors have proposed uplift maps for the Barents Sea; such maps are estimations from different methods, including geophysical, geochemical or basin modelling information (Ohm et al., 2008; Henriksen et al., 2011a; Johansen et al., 2016; Baig et al., 2016). We intend to demonstrate the potential of integrating uplift estimations into the rock-physics workflow to estimate expected AVO classes for a particular reservoir away of the well; or inversely, provide the tools for understanding observed signatures by constraining the geological history. Additionally, it can also assist in predicting net erosion from AVO data and present constraints to velocity model building for depth conversion.

Chapter 2

Theory

This chapter provides the necessary theoretical background for building a rock-physics framework that is constrained by geological history; the processes that affect the rock properties during their depositional and diagenetic history. As well, it presents some basic notions to AvO terminology and basic mathematical expressions for reflectivity.

It is worth to mention that part of this chapter is described in the *Specialization course report* the precedes this work.

2.1 Sandstone diagenesis

Diagenesis includes the effect of different physical, chemical and biological processes that occur after sedimentation by which the sediments configuration rearranges in order to equilibrate physical and chemically with the environment conditions (Burley et al., 1985; Worden and Burley, 2009). Diagenesis includes the effect of different physical, chemical and biological processes that occur after sedimentation by which the sediments configuration rearranges in order to equilibrate physical and chemically with the environment conditions (Worden and Burley, 2009).

For the scope of this study, the diagenetic processes we study here are compaction and cementation (**Figure 2.1**).

2.1.1 Compaction

The volume reduction and pore-water expulsion within the sediments is referred to as compaction. It is the result of increasing the vertical stress when adding weight in the sediment column. It can also be the result of horizontal stresses in compressional tectonic settings. (Worden and Burley, 2009). In loose sandstones, experimental compaction with a depositional porosity span of 40-42% concludes that when exposed to stresses of 20-30 MPa, the porosity can be reduced to 35-25%, and this depends on different textural an mineralogical factors, such as grain strength and grain size (Bjørlykke and Jahren, 2010). For well-sorted sands, increasing the grain size leads to higher compaction due to higher probability of grain crushing (Fawad et al., 2011).

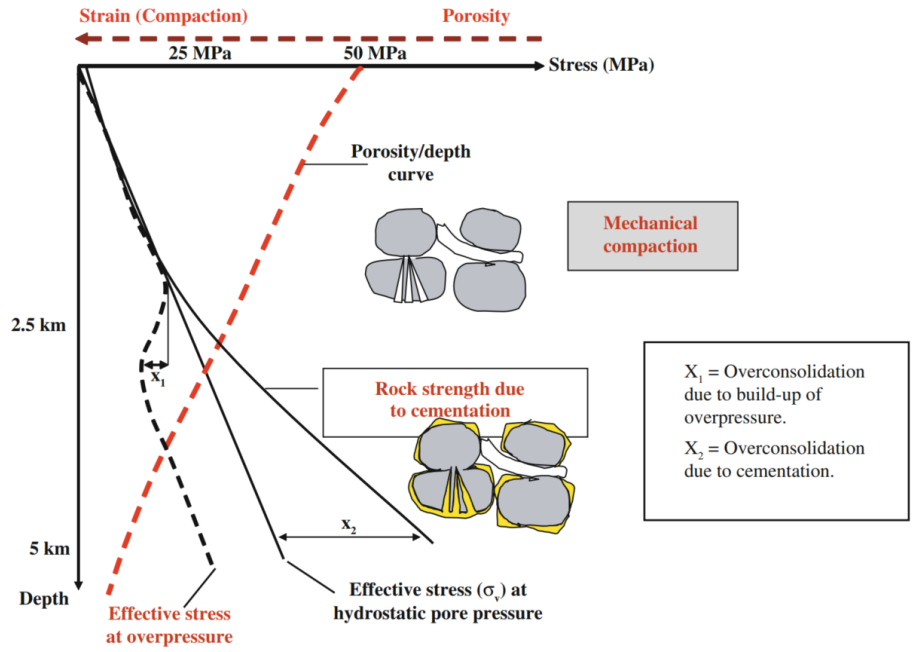

Figure 2.1: Illustration of sandstone porosity reduction as a function of depth. It highlights the two diagenetic processes, compaction and cementation.From Bjørlykke and Jahren (2010).

Additionally, overpressure prevents porosity loss due to mechanical compaction because the effective stress is reduced (Bjørlykke and Jahren, 2010).

2.1.2 Cementation

After reaching temperatures of around 70-80°C, quartz cementation inhibits the mechanical compaction by stabilizing the rock's framework and adding strength to the rock in a faster rate than the increase in the effective stress, becoming the main factor controlling the porosity reduction (Bjørlykke and Jahren, 2010) . According to Bjørlykke and Jahren (2010), after reaching these temperatures, quartz cementation will not cease until all the porosity is lost or the temperature decreases below than approximately 70%.

The amount and rate of quartz cementation is a function of the temperature, but it also depends on the sandstone's characteristics. More details about the cementation process will be discussed in section 2.2.2.

2.2 Porosity-depth trends

2.2.1 Mechanical compaction model

Lander and Walderhaug (1999) introduced a compaction function that includes the effects of grain ductility, sorting and grain size, and relates them to the effective stress. To do so, they used intergranular volume (IGV) to measure compaction indirectly to avoid measurement subjectivity, since it can be determined from point-count data. Additionally, it can include cement volumes in

the intergranular porosity to be used the simulation. The function that simulates compaction is:

$$IGV = IGV_f + (\phi_0 + m_0 - IGV_f)\exp^{-\beta\sigma_{es}} \tag{2.1}$$

where ***IGV*** represents the sum of the pore space, cements and matrix material (***fraction***), IGV_f corresponds to the stable packing configuration (***fraction***), ϕ_0 is the depositional or critical porosity (***fraction***), m_0 represents the initial proportion of matrix material (***fraction***), β in the exponential decay of ***IGV*** with increasing effective stress (MPa^{-1}) and σ_{es} corresponds to the maximum effective stress (MPa).

2.2.2 Chemical compaction model

In this study, we use Walderhaug (1996) model to simulate the quartz cementation and associated porosity reduction.Precipitation of minerals different from quartz are not included in the model, and mechanical compaction effects are assumed to stop at the onset of quartz cementation.

The volume of quartz ***Vq*** (cm^3) that is precipitated in a $1cm^3$ volume of sandstone with surface area ***A (*** cm^2***)***, at a constant temperature over a period of time ***t*** (s) can be describe as a function of the quartz molar mass, M ***(*** $60.09g/mole$***)***, the rate of quartz precipitation r ***(in*** g/cm^3***)***, and the quartz density ρ $(2.65g/cm^3)$:

$$Vq = MrAt/\rho \tag{2.2}$$

The quartz precipitation rate, **r**, corresponds to a logarithmic function of temperature ***T in*** ^oC, where ***a*** $(moles/cm^2)$ and ***b*** $(1/^oC)$ are constants:

$$r = a10^{bT} \tag{2.3}$$

If the temperature is time-dependent, ***T*** can be substituted by a linear function as follows:

$$r = a10^{b(c_n t + d_n)} \tag{2.4}$$

where c_n ***(*** $^oC/s$***)*** is the heating rate, the initial temperature is d_n ***(*** ^oC***)*** and the index ***n*** correspond to the step in the time-temperature curve.

Thus, the amount of quartz ***Vq*** that is precipitated over the time interval $t_0 - t_m$ is found by the sum of a series of integrals where each integral represents a time step (Walderhaug, 1996). This can be rewritten discretely:

$$Vq = Vq_{n-1} + \frac{Mr_{n-1}A_{n-1}dt}{\rho} \tag{2.5}$$

where ***dt*** represents the time step that is discretized. To solve equation (2.5), the initial values Vq_0, A_0 and r_0 are needed. Vq_0 is the volume of quartz cement at onset of quartz cementation, so it is assumed to be equal to 0, r_0 corresponds to the rate of quartz cementation when quartz cementation starts. A_0 corresponds to the initial grain surface area, which can be expressed as a function of the fraction of detrital quartz (***f***), the clay coating fraction (***C***) and the grain diameter (***D*** ***in*** cm) as:

$$A_0 = \frac{6(1-C)f}{D} \tag{2.6}$$

In the next time steps, the surface area A_0 is updated by following the relationship

$$A_n = A_0 \frac{\phi_n}{\phi_0} \tag{2.7}$$

where

$$\phi_n = \phi_0 - V q_n \tag{2.8}$$

2.3 Rock physics models

Dvorkin and Nur (1996) introduced rock-physics diagnostic techniques that allow inferring microstructure from porosity-velocity relationships. The idea is that a curve modelled for atheoretical effective-medium can fit a trend in the data under the assumption that the microstructure of the sediments corresponds to the model (Avseth et al., 2005). Hereunder, we present a summary of some rock-physics models based on contact theory that help to describe the different processes and scenarios, either diagenetic or sedimentological, for clean sandstones and that are used for the rock-physics depth trend modelling in this work.

2.3.1 Hashin-Shtrikman bounds

The Hashin-Shtrikman bounds represent the best bound to predict the effective elastic moduli of a mixture of grains and pores when just considering the volume of fractions of the constituents and their elastic moduli, neglecting any geometrical considerations of the phases; it also results in the narrowest range under these considerations (Hashin and Shtrikman, 1963; Avseth et al., 2005; Mavko et al., 2020).

$$K^{\pm} = K_1 + \frac{f_2}{(K_2 - K_1)^{-1} + f_1 (K_1 - \frac{4}{3} G_1)^{-1}} \tag{2.9}$$

$$G^{\pm} = G_1 + \frac{f_2}{(G_2 - G_1)^{-1} + 2 f_1 \frac{K_1 + 2G_1}{5 G_1 (K_1 + \frac{4}{3} G_1)}} \tag{2.10}$$

where f_1 and f_2 are the volume fractions of each of the constituents; K_1 and K_2 are their respective bulk moduli and G_1 and G_2 their shear moduli. We obtained either the upper or lower bound interchanging which material constitutes phases 1 or 2. Physically, these bounds are interpreted as an assembly of spheres of material 2 embedded in a shell of material 1. The upper bound results when the shell is made up of the stiffest constituent; contrarily, the lower bound corresponds to the case when it is in the core. This assemblage (figure 2.2) is composed of a diverse set of coated spheres with different size distributions filling the space (Mavko et al., 2020).

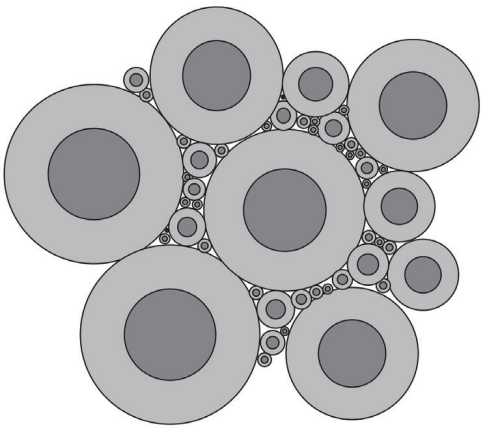

Figure 2.2: Physical representation of Hashin-Shtrikman scheme for two constituents assemblage. From Mavko et al. (2020).

2.3.2 Friable-sand model

Dvorkin et al. (1999) described a theoretical model for high-porosity unconsolidated sandstone that depends on only physical parameters. This model describes the porosity-velocity relationship as sorting deteriorates. It includes contact theory described by Mindlin (1949) and the Hashin-Shtrikman lower bound.

The Hertz-Mindlin contact theory describes the dry framework moduli K_{HM} and G_{HM}, effective bulk and shear moduli respectively, at critical porosity (ϕ_c) as the following:

$$G_{HM} = \frac{5 - 4\nu_s}{5(2 - \nu_s)} \left[\frac{3n^2(1 - \phi_c)^2 G_s^2 P}{2\pi^2(1 - \nu_s)^2} \right]^{1/3} \tag{2.11}$$

$$G_{HM} = \frac{5 - 4\nu_s}{5(2 - \nu_s)} \left[\frac{3n^2(1 - \phi_c)^2 G_s^2 P}{2\pi^2(1 - \nu_s)^2} \right]^{1/3} \tag{2.12}$$

where *P* is the effective pressure, G_s and ν_s are the shear modulus and Poisson's ratio of the solid mineral, *n* is the coordination number, which is the average number of contacts per grain. To connect this point with the mineral extreme point, the Hashin-Shtrikman Lower bound is used. Due that unconsolidated sediments are modelled, the softest arrangement of the two end-point materials is accomplished by this bound (figure 4.1). Then, the dry framework moduli can be estimated for the lower porosities:

$$K_{Dry} = \left[\frac{\frac{\phi}{\phi_c}}{K_{Hm} + \frac{4}{3}G_{HM}} + \frac{1 - \frac{\phi}{\phi_c}}{K + \frac{4}{3}G_{HM}} \right]^{-1} - \frac{4}{3}G_{HM} \tag{2.13}$$

$$G_{Dry} = \left[\frac{\frac{\phi}{\phi_c}}{G_{Hm} + Z} + \frac{1 - \frac{\phi}{\phi_c}}{G + Z} \right]^{-1} - Z \tag{2.14}$$

$$Z = \left[\frac{9K_{HM} + 8G_{HM}}{K_{HM} + 2G_{HM}} \right] \frac{G_{HM}}{6} \tag{2.15}$$

A reduction of porosity in this model is achieved by adding smaller grains in the pore space, this will result in sorting deterioration and a gentle increase in the rock stiffness (Avseth et al., 2005).

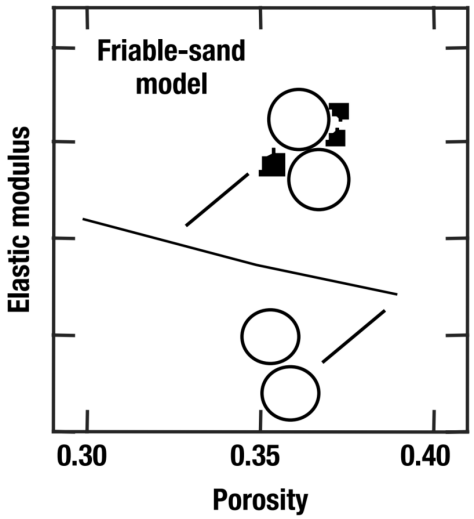

Figure 2.3: Porosity-Elastic modulus representation of the friable sand model.From Avseth et al. (2005).

2.3.3 Contact-cement model

During burial, if certain conditions are reached, sandstones can suffer cementation. The stiffening effect is more significant because the cement "glues" the grains contacts. In this model, the porosity reduction is the result of deposition of uniform cement layers that will stiffen the rock dramatically by reinforcing the grain contacts (Avseth et al., 2005) (see figure 2.4). Dvorkin and Nur (1996) proposed a mathematical model where the effective dry bulk (K_{Dry}) and shear (G_{Dry}) moduli of the rock are:

$$K_{Ddry} = \frac{n(1-\phi_c)M_c S_n}{6} \tag{2.16}$$

$$K_{Dry} = \frac{3K_{Dry}}{5} + \frac{3n(1-\phi_c)G_c S_\tau}{20} \tag{2.17}$$

$$M_C = K_c + \frac{4}{3}G_c \tag{2.18}$$

where ϕ_c is the critical porosity, *n* is the coordination number, K_c and G_c are the bulk and shear moduli of the cementing mineral, M_c is the compressional modulus of the cement. The parameters S_n and S_τ are proportional to the normal and tangential stiffnesses as follows:

$$S_n = A_n(\Lambda_n)\alpha^2 + B_n(\Lambda_n)\alpha + Cn(\Lambda_n) \tag{2.19}$$

$$S_\tau = A_\tau(\Lambda_\tau, \nu_s)\alpha^2 + B_\tau(\Lambda_\tau, \nu_s)\alpha + C_\tau(\Lambda_\tau, \nu_s) \tag{2.20}$$

where A_n, B_n, C_n, A_τ, B_τ and C_τ are functions of the normal and tangential stiffnesses, ν_s the Poisson's ratio of the framework mineral and α represents how the amount of contact cement is distributed. Two schemes were proposed by Dvorkin and Nur (1996) to described cement deposition in the pore space (Figure 2.5).

Equation 2.21 and **equation 2.22** describe the schemes 1 and 2 respectively.

$$\alpha = 2\left[\frac{\phi_c - \phi}{3n(1-\phi_c)}\right]^{\frac{1}{4}} \tag{2.21}$$

$$\alpha = \left[\frac{2\phi_c - \phi}{3(1-\phi_c)}\right]^{\frac{1}{4}} \tag{2.22}$$

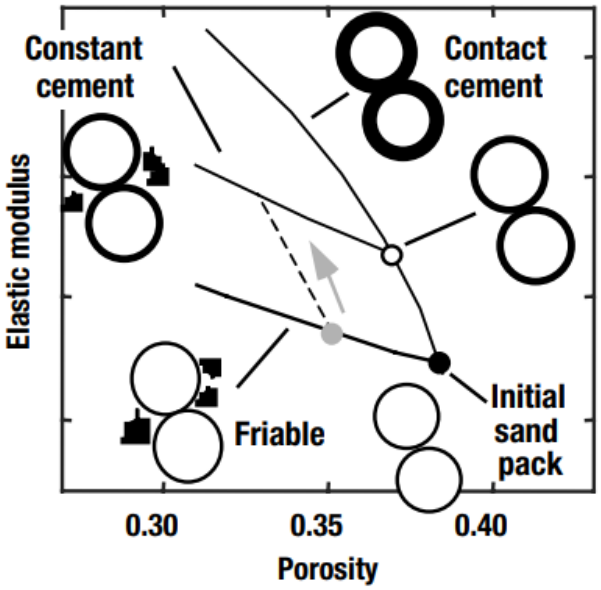

Figure 2.4: Porosity-Elastic modulus representation of the friable sand, contact cement and constant cement models. From Avseth et al. (2005).

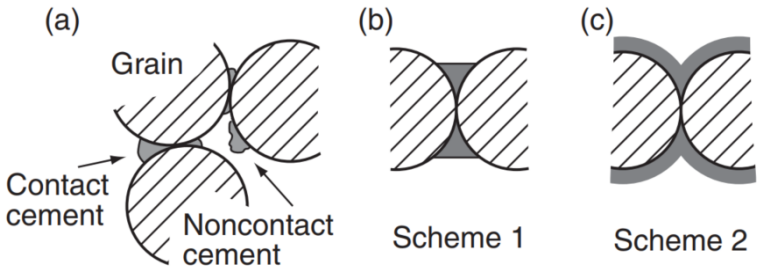

Figure 2.5: (a) Representation of the types of cement deposition.(b) All cement deposited at grain contacts.(c) Cement deposited in uniform layer around grains. From Mavko et al. (2020).

2.3.4 Constant cement model

Avseth et al. (2000) presented a rock physics model for cemented sandstones with varying sorting due solely to non-cement pore-filling material. This model introduced a way to understand the textural variation for a consolidated sandstone at a constant depth. Mathematically it is

represented as a combination of the contact-cement and the Hashin-Shtrikman lower bound and it is expressed as follows:

$$K_{Dry} = \left[\frac{\frac{\phi}{\phi_b}}{K_b + \frac{4}{3}G_b} + \frac{1 - \frac{\phi}{\phi_b}}{K + \frac{4}{3}G_b} \right]^{-1} - \frac{4}{3}G_b \tag{2.23}$$

$$G_{Dry} = \left[\frac{\frac{\phi}{\phi_b}}{G_b + Z} + \frac{1 - \frac{\phi}{\phi_b}}{G + Z} \right]^{-1} - Z \tag{2.24}$$

$$Z = \left[\frac{9K_b + 8G_b}{K_b + 2G_b} \right] \frac{G_b}{6} \tag{2.25}$$

where phi_b represents the porosity at the well-sorted end-member at constant cement (open circle in figure 2.4); K_b and G_b are the bulk and shear moduli at this porosity which are calculated with the using the contact-cement model. Then, the sorting degradation is interpolated using the Hashing-Shtrikman lower bound.

2.3.5 Shale Velocity-porosity relationships

Different authors have proposed velocity-porosity relationships for shales; each of them approaches the solution to the problem from a different perspective. Marion et al. (1992) model describes the porosity-velocity relationship in a shale with dispersed silt particles. Such a relationship is expressed by the Reuss averaging of the clay minerals (high-porosity end member) and quartz that comform the silt (low-porosity end member). Similarly, Dvorkin and Gutierrez (2001) describe a silty shale where the porosity-velocity behaviour is dependent on the clay content; the high-porosity end member represents the pure shale, while the low-porosity end member corresponds to their shaly sand model. Avseth et al. (2005) proposed the constant-clay model for shales; this model is analogue to the friable sand model, but in this case, the high-porosity endmember is dependent on the clay content, and the mineral point corresponds to the clay mineral, or in the case of silty shales to the resulting mineral mix of clay and quartz. Vernik and Kachanov (2010) proposed a generalized empirical anisotropic model for brine-saturated shales, where the two variables are porosity and volume of clay. The estimated velocity propagates in the normal direction to the bedding.

As stated above, the constant-clay model described by Avseth et al. (2005) assumes that the shales are not cemented and that the modelled shales have constant clay content. We can calculate the dry bulk and shear moduli, K_{dry} and G_{dry} by using Hertz-Mindlin and the Hashin-Shtrikmann lower bound. The saturated moduli can be calculated with the Gassmann (1951) equations. If the shales are silty, an effective mineral has to be calculated. Because the silt grains are assumed to be suspended in the clay matrix, the mineral point can be approximated by the Reuss average as follows:

$$\frac{1}{K_{mixed}} = \frac{1 - C}{K_{qtz}} + \frac{C}{K_{clay}} \frac{1}{G_{mixed}} = \frac{1 - C}{G_{qtz}} + \frac{C}{G_{clay}} \tag{2.26}$$

where K_{mixed} and G_{mixed} are the effective mineral moduli for a clay/silt mixture made up from a fraction of clay C with corresponding moduli K_{clay} and G_{clay} moduli and the quartz silt with moduli K_{qtz} and G_{qtz}. Figure 2.6 illustrates the constant-clay model for shale composed of

silt quartz grains and equal amounts of Smectite and Illite. As it is seen, the velocity is higher when the clay volume is reduced. It can be appreciated that the porosity at which each model starts is different. It is expected that in pure shales the critical porosity is higher than in their siltier counterpart.

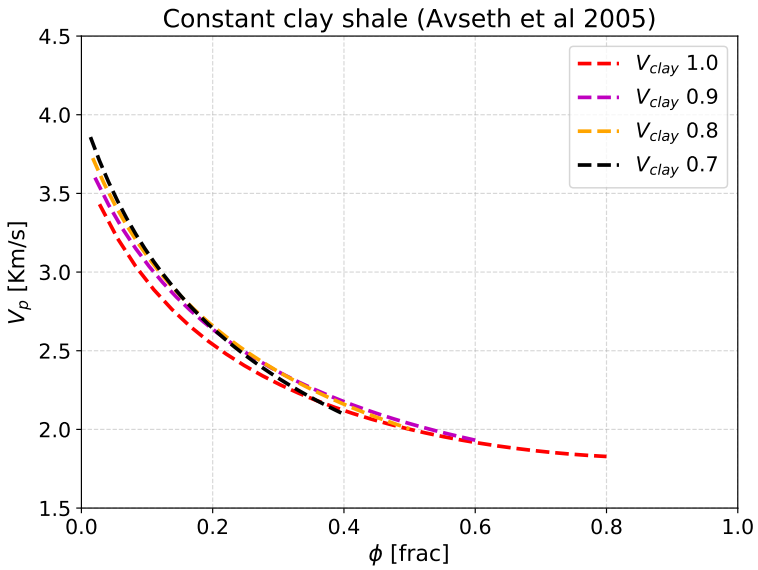

Figure 2.6: Constant clay shale model after Avseth et al. (2005). The dashed lines represent iso-clay content. The lines correspond to 25 MPa effective stress and coordination number of 4.

Vernik and Kachanov (2010) introduced a model that accounts for anisotropy and avoid the need of performing a fluid substitution in non-Gassmann rocks. The model is developed to estimate vertical velocities and it is just dependent on measurable parameters, porosity and clay content (*see figure 2.7*). The stiffness that controls the vertical P-wave velocity is C_{33} and it is proposed to be expressed as:

$$C_{33} = C_{33}(1-\phi)^k \tag{2.27}$$

where C_{33m} is the solid matrix stiffness, ϕ is the porosity and k is a factor related to the clay content:

$$k = 5.2 - 1.3V_{clay} \tag{2.28}$$

The stiffness of the matrix C_{33m} can be calculated as a mixture of a clay constituent of concentration V_{clay} and stiffness C_{33clay} with the other constituents (assumed to be quartz) with P-wave modulus M_{quartz}.

$$C_{33m} = \left(\frac{V_{clay}}{C_{33clay}} + \frac{1-V_{clay}}{M_{quartz}}\right)^{-1} \tag{2.29}$$

Then, the water-saturated shale vertical velocity is computed as:

$$V_p(0^o) = \sqrt{\frac{C_{33}}{\rho_m(1-\phi)+\rho_m\phi}} \tag{2.30}$$

where ρ_m is the density of the matrix and ρ_w the brine density. Due to expected changes in the clay minerals density with diagenesis, the following density expression intends to compensate for such changes:

$$\rho_m = 2.76 + 0.001\{(\rho_m - 2) - 230exp[-4(\rho_m - 2)]\} \tag{2.31}$$

A suggested value for C_{33clay} is $33.4GPa$ when assuming that the clay mineralogy that is predominant in advanced stages of diagenesis are illite/chlorite/kaolinite, and with wave propagation orthogonal to the shale layering.

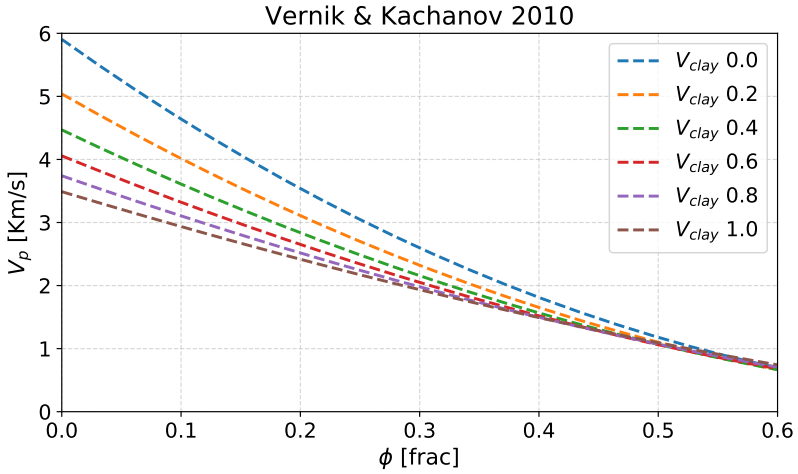

Figure 2.7: Porosity and P-wave velocity after Vernik and Kachanov (2010). The dotted lines represent iso-clay content.

2.4 Amplitude variations with offset (AvO)

As a commercial tool, AvO has been present in the O&G industry for decades.Ostrander (1984) acknowledges the variation that the angle of incidence has the P-wave reflectivity in an interface; this variation is highly related to the Poisson's ratio of the layers that made up the interface. Additionally, the application of analyzing such variations was demonstrated to differentiate the anomalies in amplitudes related to gas-bearing sands to another kind of anomalies. The technology has proven to be robust and provides the interpreter with more information than the traditional qualitative seismic interpretation. However, it also depends on several physical factors that add complexity to the amplitude interpretations. The technique has been widely used and successful; however, the interpreter has to be aware of its pitfalls and limitations (Avseth et al., 2005).

Ambiguities, when using this technique, come from the data itself during acquisition and processing. Additionally, wave propagation phenomena will present challenges to the correct AvO interpretation and the quality of its analysis, i.e. tunning, lithology, overburden effects. Nonetheless, this work is focused on how maximum burial and subsequent uplift affect the AvO signatures of sandstone reservoirs.

2.4.1 Reflectivity in isotropic media

The main advantage of this technique is the ability to understand the seismic amplitudes in physical quantities. In this sense, we present here a summary of the mathematical expressions for reflectivity dependent on angle. Zoeppritz (1919) described mathematically the reflection coefficient for plane elastic waves at a plane interface depending on the angle of incidence. The system of equations known as *Zoeppritz equations* are highly complex; thus, approximations of them have been presented by different authors (Aki and Richards, 1981; Shuey, 1985).

Aki and Richards (1981) proposed a linear approximation of the *Zoeppritz equations* under the assumption of weak layer contrast resulting in the following expression:

$$R\theta_1 \approx \frac{1}{2}(1 - 4p^2V_s^2)\frac{\triangle_\rho}{\rho} + \frac{1}{2\cos^2\theta}\frac{\triangle_{V_p}}{V_p} - 4p^2V_s^2\frac{\triangle V_s}{V_s} \tag{2.32}$$

where:

$$\begin{aligned} \triangle\rho &= \rho_2 - \rho_1 & \triangle_{V_p} &= V_{p2} - V_{p1} & \triangle_{V_s} &= V_{s2} - V_{s1} \\ \rho &= \frac{\rho_2 + \rho_1}{2} & V_p &= \frac{V_{p2} + V_{p1}}{2} & V_s &= \frac{V_{s2} + V_{s1}}{2} \\ p &= \frac{\sin\theta_1}{V_{p1}} & \theta &= (\theta_1 + \theta_2) \end{aligned}$$

These parameters represent the angle of incidence θ_1 and transmission θ_2, and the properties above and below the interface, denoted by the subscripts *1* and *2* respectively. $\triangle\rho$, $\triangle V_p$ and $\triangle V_s$ represent change of density, p-velocity and s-velocity respectively. Similarly, ρ, V_p and V_s represent the mean properties above and below the interface.

Equation 2.32 is further approximated by Shuey (1985) as follows:

$$R(\theta) \approx R_0 + G\sin^2\theta + F(\tan^2\theta - \sin^2\theta) \tag{2.33}$$

where

$$R_0 = \frac{1}{2}\left(\frac{\triangle_{Vp}}{V_p} + \frac{\triangle\rho}{\rho}\right) \tag{2.34}$$

$$\begin{aligned} G &= \frac{1}{2}\frac{\triangle V_p}{V_p} - 2\frac{V_s^2}{V_p^2}\left(\frac{\triangle\rho}{\rho} + 2\frac{\triangle V_s}{V_s}\right) \\ &= R_0 - \frac{\triangle\rho}{\rho}\left(\frac{1}{2} + \frac{V_s^2}{V_p^2}\right) - \frac{4V_s^2}{V_p^2}\frac{\triangle V_s}{V_s} \end{aligned} \tag{2.35}$$

$$F = \frac{1}{2}\frac{\triangle V_p}{V_p} \tag{2.36}$$

R_0 corresponds to the normal incidence or zero-offset incidence , *G* represents the intermediate angles (up to about 30º) and F correspond to higher angles approximating to critical angles. In practice, the available angles for AvO analysis are less than 30º-40º (Avseth et al., 2005). Hence, we only consider the first two terms from Shuey (1985), resulting in the following expression:

$$R(\theta) \approx R_0 + G\sin^2\theta \tag{2.37}$$

2.5 AVO crossplot analysis

The two term Shuey (1985) approximation are commonly referred as *Intercept* and *Gradient*, R_0 and *G* respectively. They can be interpreted in a more intuitive way when cross-plotted against each other. As seen from the equations 2.34 and 2.35, the intercept is dependent on relative changes in density and V_p. Conversely, the gradient is affected in a more complex way; the poisson's ratio, or V_p/V_s, influence strongly on its behavior. Thus, R_0 versus G provides a more flexible space for understanding the rock properties.

To ease the AvO interpretation, different authors have proposed a classification for the AvO responses for different shale/sand interfaces based on where the top of the sand would plot in the R_0 versus *G* space (Figure 2.8):

1. *Class I* are high impedance sandstones, characterized by a strong positive intercept and the reflectivity decreases with offset (negative gradient). Conversely, the V_p/V_s ratio is low in comparison to the encasing material.

2. *Class II* describes sands that has a similar impedance as the encasing shale. This results in a close to zero reflectivity at normal incidence angle. Ross and Kinman (1995) separated this class in two, *IIp* and *IIn*. The former have a positive weak intercept with a negative gradient, resulting in polarity reversal. The latter is characterized with a weak negative intercept and negative gradient, becoming more negative at further angles.

3. *Class III* corresponds to gas sands that have lower acoustic impedance than the encasing medium. Thus, they are characterized by a strong negative intercept and a negative gradient that is not generally large. These class is often associated with bright spots and soft saturated sands (Avseth et al., 2005).

4. *Class IV* was introduced by Castagna and Swan (1997) and is the product of a soft sand encased in a stiffer shale, where the shale V_p/V_s ratio are higher than in the sands, resulting in a negative intercept and positive gradient.

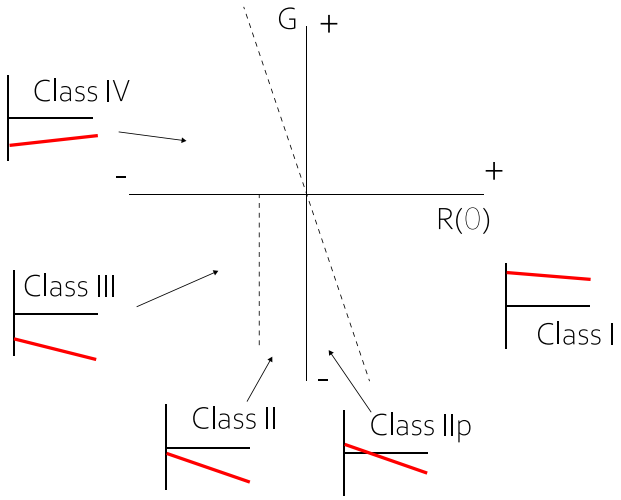

Figure 2.8: AvO classes illustration and their position in R_0 versus G space. From Simm and Bacon (2014).

Chapter 3

Data set

3.1 Geological Framework of the Barents Sea

The Barents Sea is located in the northwestern corner of the Eurasian continental shelf. Since Caledonian times this region has been affected by different tectonic episodes. Nonetheless, the intensity of the tectonic processes varies at different degrees, depending on the sector. The western part of the Barents Sea is the most affected by tectonics since Mesozoic and Cenozoic times. On the contrary, the eastern and northeastern sectors have been relatively more stable platforms since the Late Carboniferous (Gabrielsen et al., 1990). Figure 3.1 illustrates the present-day configuration of the Barents Sea, with its different basins and the major structural elements.

The Post-Caledonian evolution of the western Barents Sea was dominated by three extensional phases that occurred during the Late Devonian-Early Carboniferous, Middle Jurassic-Early Cretaceous, and a final rift stage during the Cenozoic. Two distinct geological provinces in the southwestern Barents sea are recognized. One consists of the Mesozoic basins and highs comprised by the Finnmark Platform, Hammerfest Basin, Loppa High and Fingerdjupet Subbasin. The other province consists of Cretaceous and Cenozoic basins, that are Harstad, Tromø, Bjørnøya and Sørvestsnaget basins which are separated by the Senja Ridge, Veslemøy High and Stappen High (Faleide et al., 1993).

During the late Paleozoic, the major part of the Barents Sea underwent crustal extension which was characterized by rifting migrating towards the west; well-defined rifts and pull-apart basins in the southwestern region and strike-slip faults complexes to the north. On the contrary, the Svalbard Platform and the eastern part of the regional basin haven been stable since the late Paleozoic (Faleide et al., 2010).The deposition of the Billefjorden Group, which consisted of non-marine tropical clastics started in the Late through the Early Carboniferous (Worsley, 2008). Subsequent uplift and extensional regime during the mid-Carboniferous resulted in the formation of a wide rift zone. This rifting phase resulted in the development of interconnected extensional basins, where syn-rift sediments were deposited (Faleide et al., 2010). The Gipsdalen Group sediments were deposited, first dominated by clastics sourced to the faulted graben margins. However, during the Late-Carboniferous the sea level rose in a more quiet tectonic regime, allowing the shelf to become a warm-water carbonate platform that gave place to the deposition of organic build-ups and in low-sea level times the deposition of evaporites. During the Early

Permian, a drastic change in the seawater temperature and depths resulted in the deposition of the Bjarmeland Group which consisted of cold water carbonates; the seawater temperature continues to drop to colder conditions giving place to the deposition of siliceous shales that conform the Tempelfjorden Group (Worsley, 2008).

The Triassic was characterized by high subsidence and vast amounts of sediments fed to the entire Barents shelf sourced by the Uralia highland to the east and the Baltic Shield (Faleide et al., 2010). Most of the active faults during the Early Triassic were localized along the western margin, resulting in the uplift and erosion of the Loppa High. Four lithostratigraphic units made up the Triassic succession of the Norwegian sector of the Barents Sea: Havert, Klappmyss, Kobbe (Sassendalen Group) and Snadd (Base of the Kapp Toscana Group) formations, each of them representing regressive-transgressive regional cycles (Henriksen et al., 2011b). Later, regression and erosion occurred at the Late Triassic resulting in the shoreline to being moved back to the southern and eastern parts of the SE Barents Sea (Faleide et al., 2010).

The succeeding Lower-Middle Jurassic strata are bounded at the base by a transgressive event at the Early Norian, representing the basal contact with the underlying Snadd Formation. From this period, subsidence decreased as well as sedimentation rates resulting on less dominance of progradational systems and establishment of shallow marine and coastal conditions providing more mineralogically mature coarse-grained quartz-arenites suggesting a substantial input of sediment from the proximal areas. On the other hand, the upper boundary corresponds to the Middle- Jurassicunconformity or condensed section of the overlaying Fuglen Formation; this boundary represents the onset of Mesozoic rifting in the southwestern Barents Sea (Worsley, 2008; Faleide et al., 2010; Henriksen et al., 2011b).

According to Faleide et al. (2010), the transition to the Late Jurassic is characterized by unconformities that reflect the interplay between faulting and sea-level changes. As stated by (Worsley, 2008), the limit Late Jurassic-Early Cretaceous is marked by a drop in the sea level and the development of more open marine environments. On the other hand, the structural development of the southwestern Barents Sea during the Early Cretaceous was characterized by extensional faulting. Additionally, crustal stretching and thinning led to the deposition of thick lower Cretaceous sedimentary cover in Harstad, Tromsø and Bjørnøya basins (Faleide et al., 1993). Additionally, Worsley (2008) report that the deltaic progradation from north to south during the Early Cretaceous is and an indication of uplift in the northern margin linked to the opening of the Euramerican Basin; subsequent regional sea-level rise during the Aptian resulted in a shortage of coarse-clastic sediments. The former, combined with continued uplift in the north, gave place to a thick condensed shale-dominated wedge that extends from Spitsbergen to the southwestern Barents margin (Worsley, 2008).

Subsidence continued in the southwestern Barents Sea during the Late Cretaceous as result of pull-apart settings. This subsidence is seen in the Tromø and Sørvestnaget basins, where thick sequences were deposited. On the contrary, further east, the sedimentation at this time is distinguished by condensed sections and truncation with Cenozoic and Quaternary unconformities (Faleide et al., 1993; Henriksen et al., 2011a).

The continental break up and initiation of sea-floor spreading related to the opening of the Norwegian-Greenland Sea and the formation of the sheared western Barents Sea continental

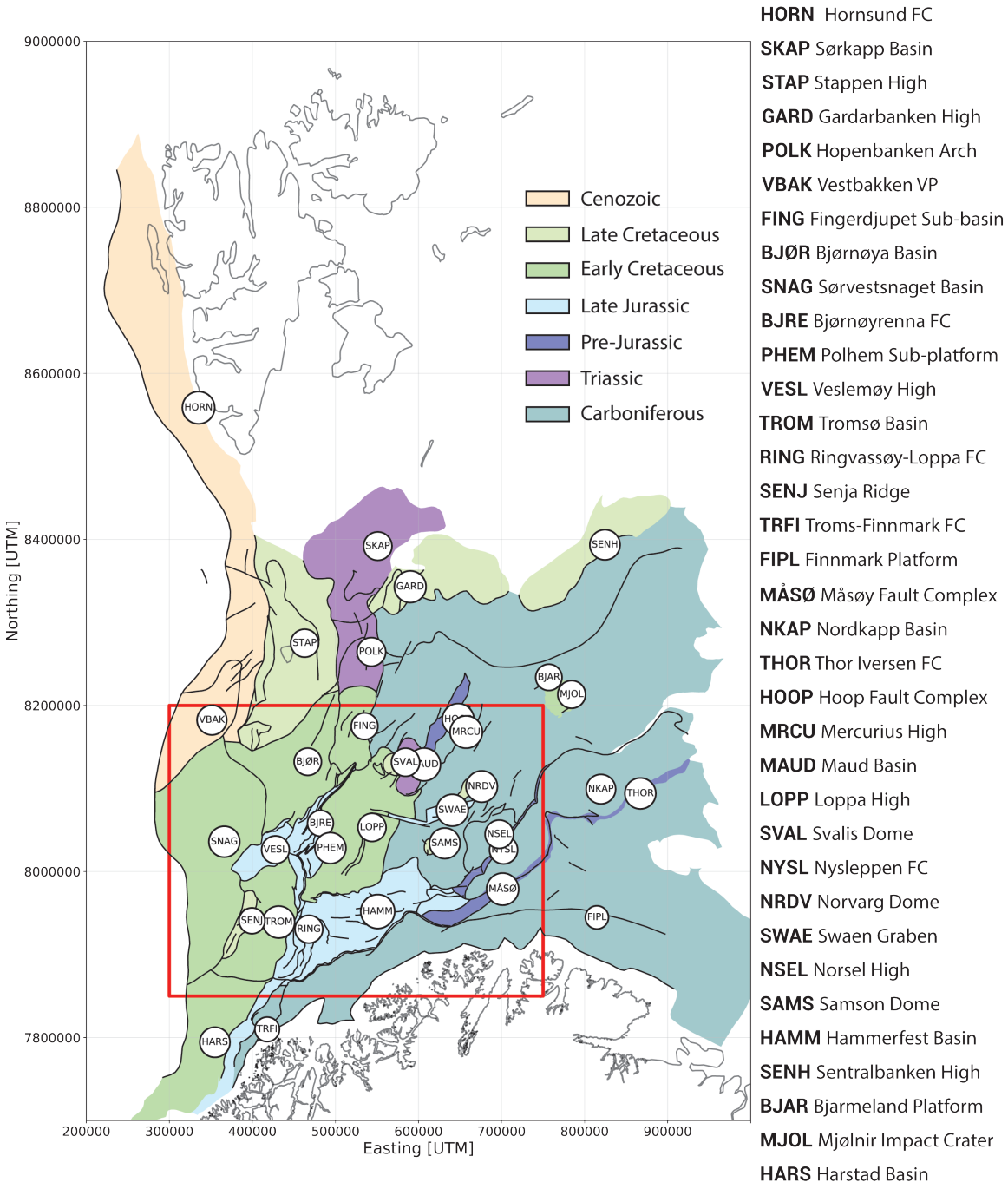

Figure 3.1: Structural elements of the Barents Sea: Basins, platforms, fault complexes, domes and other structures are included. The red square highlights the area of study.

Facie	Lithology Cutoff	Fluid Cutoff
Shale	$V_{clay} > 0.5$	
Shaly sand	$0.2 < V_{clay} \leq 0.5$	
Brine sand	$V_{clay} \leq 0.5$	
Gas sand	$V_{clay} \leq 0.2$	$SW \leq 0.8$

Table 3.1: Cutoffs established to assign lithofacies in Myrsildre, Skalle and Juksa.

margin were the main controlling factors in the development of the Barents Sea during the Paleogene (Faleide et al., 2010). The Late Paleocene was marked by rapid subsidence, and at this time, the Loppa High serves as a source of sediments to the Trømso Basin Faleide et al. (1993, 2010). The Paleocene-Early Eocene sequence is preserved in the southwestern shelf in the marine mudstone-dominated Sotbakken Group, mainly present in the Hammerfest Basin and part of the Nordkapp Basin overlaying unconformably on the Cretaceous (Worsley, 2008; Henriksen et al., 2011b).

Oceanic crust generation along the Barents Sea margin has been active since the Late Paleogene. This has been followed by the development of a clastic wedge that covers the western shelf margins and which is sourced by the uplifted Barents Sea area related to repeated subsidence and uplift due to glaciation; however, the uplift intensity has been different for the distinct areas of the Barents Sea (Faleide et al., 1993; Worsley, 2008).

3.2 Well log data

Figure 3.2 shows the location of 81 wells from different basins in the Barents Sea that were provided for this study. The log data include *CPI logs* with petrophysical information and required logs for rock physics studies (clay volume, total porosity and water saturation, density and velocities). The tops for the formation at these wells were taken from (NPD).

Three of these wells are the main focus of this study and are located on the seismic line (denoted as orange points in figures 3.2 and 3.3). They correspond to discoveries of oil or gas in the Lower Cretaceous Kolmule and Knurr Formations, Upper Jurassic Hekkingen Formation and Lower Jurassic Stø Formation. These wells correspond in NPD nomenclature as 7120/1-2,7120/2-3 S well 7120/6-3 S. For simplicity; they will be referred respectively as Myrsildre, Skalle and Juksa wells in this work (Figure 3.3).

Myrsildre and Skalle wells are located in a narrow faulted terrace south of the Loppa High; the terrace is confined by the Rigvassøy-Loppa Fault Complex (RING) to the west and the Asterias Fault Complex (AFC) to the west (Iqbal, 2016). Iqbal (2016) additionally recognized that two fault family systems interact in the terrace; one that is related to the bounding fault systems (RING and AFC) and a network of faults that occur on the shelf with preferential orientations NE-SW and NW-SE. The latter is considered to be the primary controlling mechanism for sediment transport as the different incisions and canyons are developed along these faults. Juksa, on the other hand, it is located southeast of the Loppa High into the Hammerfest Basin (HAMM).

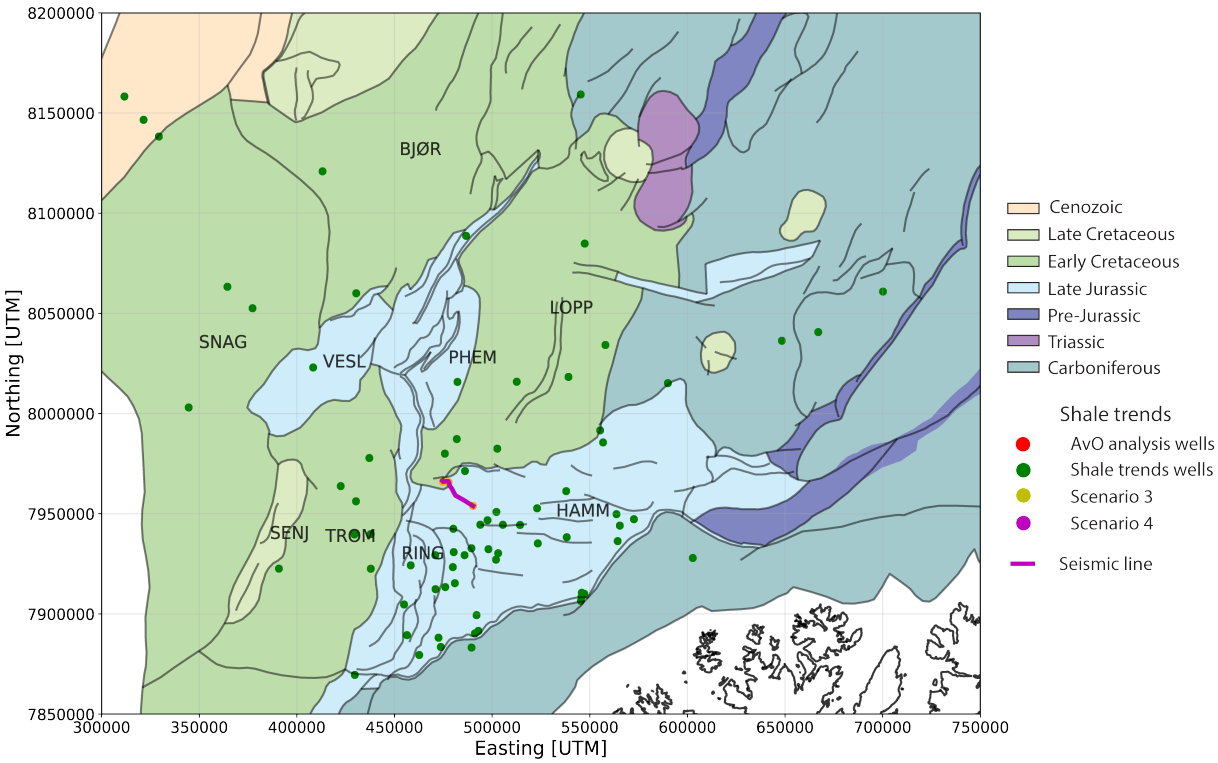

Figure 3.2: Well log and seismic data available for this study. There are two sets of wellbore data available for this study; wells that are used for estimating shale depth trends (green) and wells use of the rock-physics and AvO analysis (red).

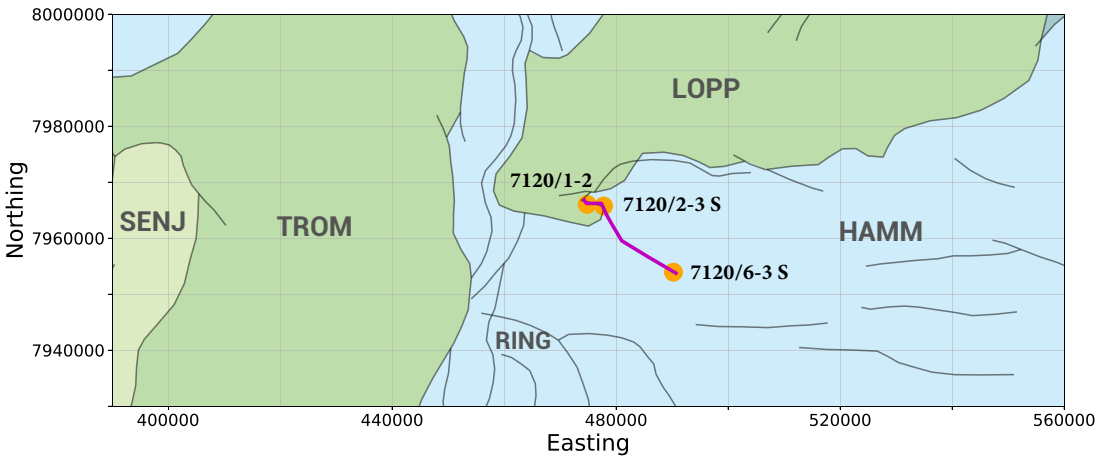

Figure 3.3: Close up to the seismic line and the three wells on it. We can recognize the main basins and structural elements of the area: *HAMM* Hammerfest Basin, *LOPP* Loppa High, *TROM* Tromsø Basin, *SENJ* Senja Ridge and *RING* Ringvassøy-Loppa Fault Complex.

3.2.1 Myrsildre discovery: Well 7120/1-2

Myrsildre well penetrated two seismostratigraphically defined Lower Cretaceous wedges with structural closure defined by a fault-bound against the Loppa High as main objectives. Wedges defined secondary objectives beneath the Base Cretaceous unconformity. Hydrocarbons were

recovered from the Upper Jurassic Hekkingen Formation and the most basal Lower Cretaceous wedge (Knurr Formation). However, the hydrocarbons demonstrated to be immovable except for the isolated sandstone from the Lower Knurr/Hekkingen Formation (Shell, 1989; NPD). Figure 3.4 displays a well panel with the petrophysical properties of this well, from the top Kolmule up to the TD. As can be seen, the best sandstones are localized in the Lower Knurr.

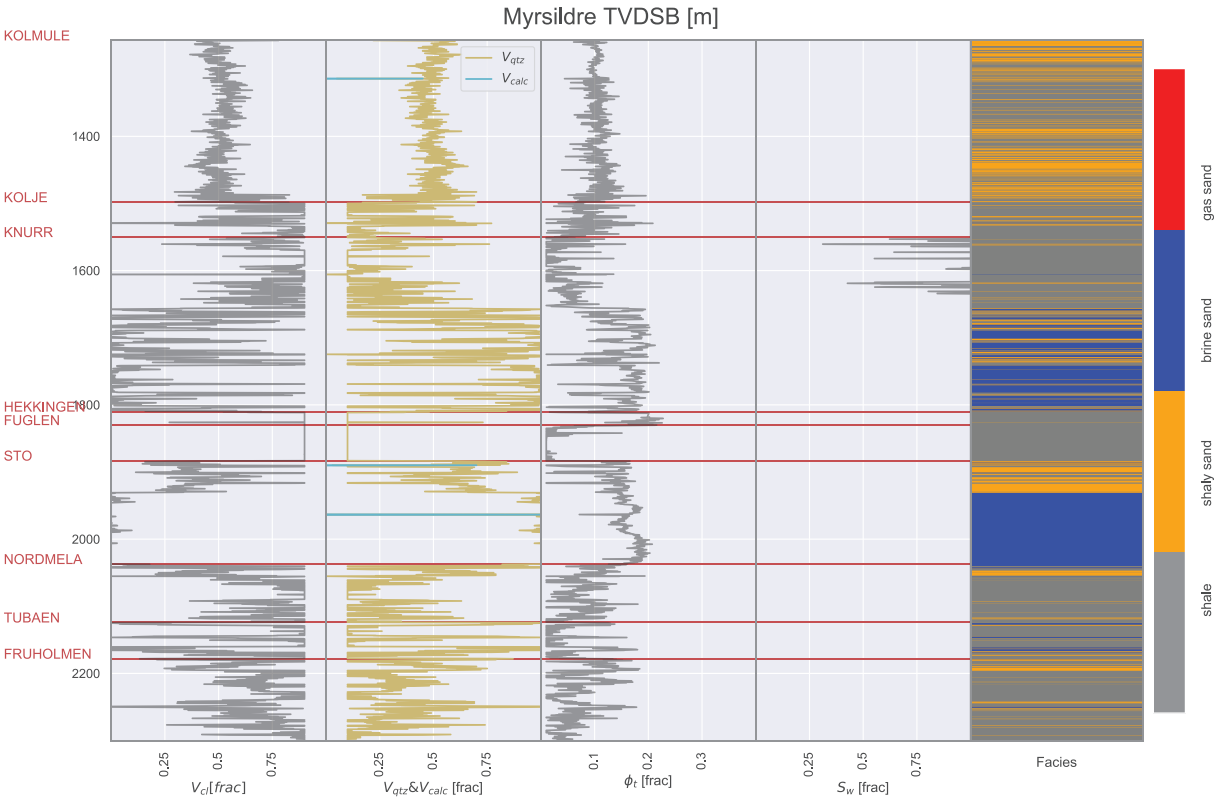

Figure 3.4: Myrsildre discovery well panel showing the petrophysical logs and facies required for rock-physics analysis. The depth datum is the sea bottom (TVDSB) in meters.

3.2.2 Skalle discovery: Well 7120/2-3 S

Skalle well proved gas at three different stratigraphic levels. The first gas column was found in sandstones and conglomerates from the Kolmule Formation; no oil shows were present at this level. A second gas reservoir was found in the thin sandstones from the Knurr Formations, with a total thickness of 6 meters, bounded below by the shales of the Hekkingen Formation. The third gas reservoir corresponds to the Stø Formation in moderate to marginal properties quality sandstones (NPD) (see figure 3.5).

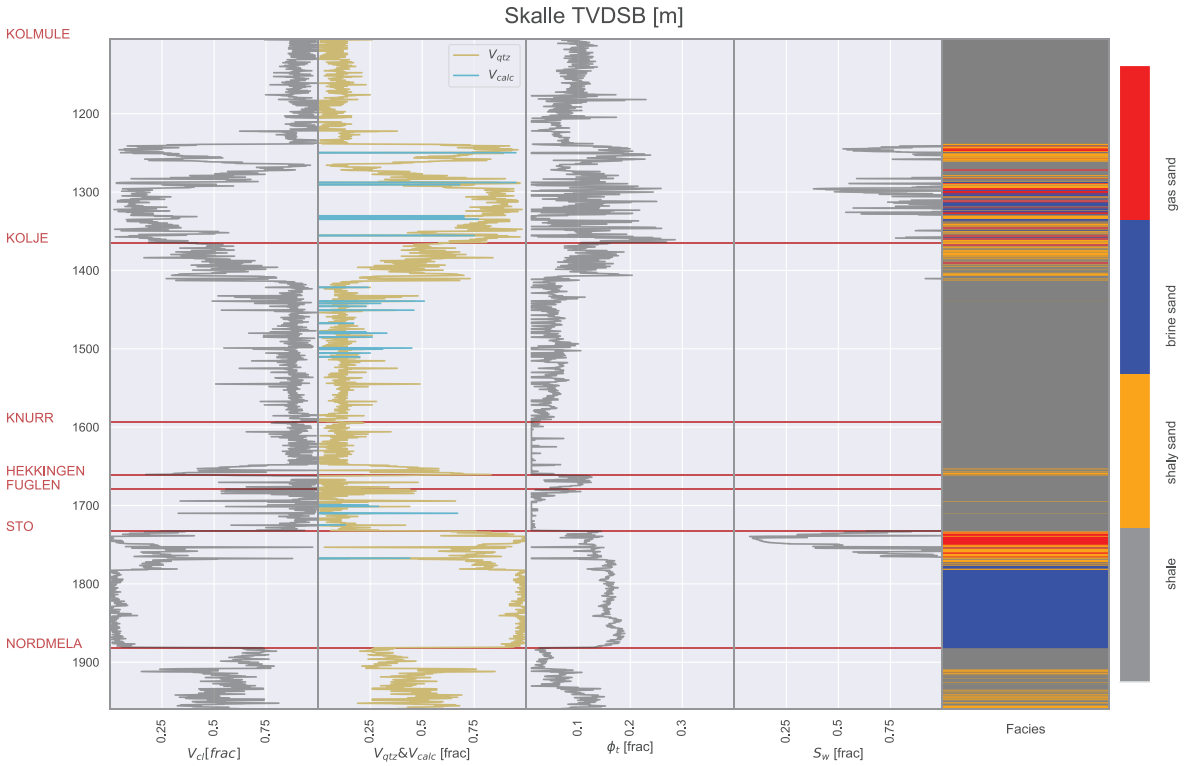

Figure 3.5: Skalle discovery well panel showing petrophysical logs and facies required for rock-physics analysis. The depth datum is the sea bottom (TVDSB) in meters.

3.2.3 Juksa discovery: Well 7120/6-3 S

Juksa well was drilled to test the basal part of the Kolmule Formation, the sandstones at the upper Hekkingen/lower Knurr Formations and sandstones of the Early-Middle Jurassic Stø Formation.The basal Kolmule Formation contained hydrocarbons shows; however, during the *RCI sampling*, only brine with traces of hydrocarbons was produced. The basal Knurr/ upper Hekkingen did not encounter sandstones nor shows where found. The Stø Formation was proven to be water-bearing with shows in sidewall cores. As a remark, two organic-rich shales were penetrated in Kolje and the basal Hekkingen Formations (NPD).

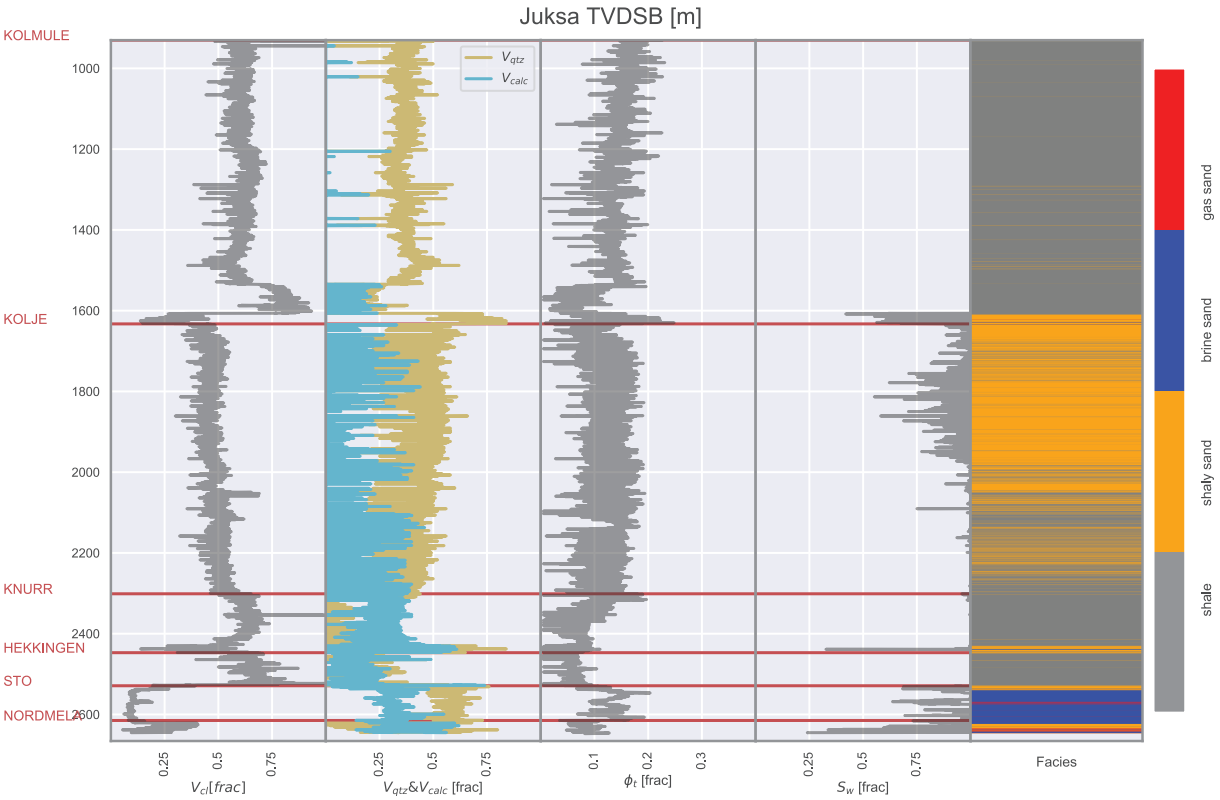

Figure 3.6: Juksa discovery well panel displaying the petrophysical logs and facies required for rock-physics analysis. The depth datum is the sea bottom (TVDSB) in meters.

Figures 3.4, 3.5 and 3.6 present the well panels for Myrsildre, Skalle and Juksa respectively. The facies are assigned based on cutoffs from the petrophysical evaluation logs V_{clay} and S_w as it is shown in figure 3.1. As it is shown, the brine sandstones and gas sandstones are characterized by being cleaner (lower V_{clay}). The fluid cutoff is not applied in the shaly sandstone facies, although some of these sands are part of the reservoir as it is the case in Kolmule and Stø at Skalle. The reason to validate the selection of this shaly facie is that the gas saturation in these lithologies is rather small for Skalle.

Figure 3.7 presents a correlation along with the wells present in the seismic line (TVDSB as datum). The sandstones, both gas- and brine-bearing are highlighted in red and blue, respectively. From the correlation, it is observable the complex changes in thickness from the northwest (Myrsildre) to the southeast (Juksa). Thickness change is more evident in the Cenozoic and Late Mesozoic (Cretaceous) units than in the Jurassic units.

3.2.4 Rock physics diagnostics

Iqbal (2016) gives an overview of the rock physics diagnostics for the Cretaceous rocks in Myrsildre and Skalle wells, acknowledging the critical effect that cement has on the rock physics properties. Additionally, provides approximates for the depths at which chemical compaction dominates the porosity reduction at each of these wells; it was proposed that the effect of quartz cementation dominates at depths of around 1500 meters in Skalle, and 1600 meters in Myrsildre, suggesting that the cemented sandstones are encountered slightly deeper in Myrsildre. These

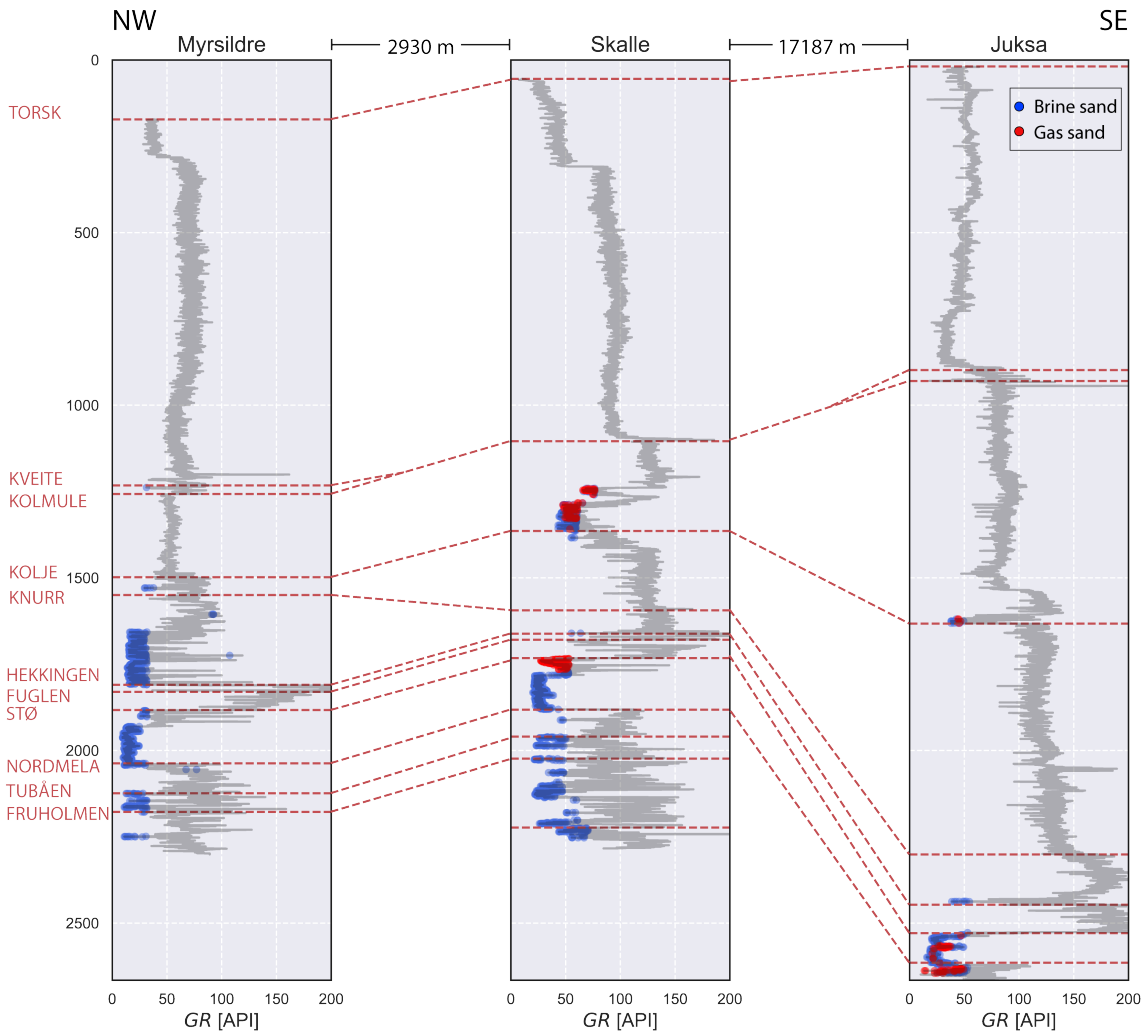

Figure 3.7: Well log correlation of the wells on the seismic line. The correlation orientation is northwest (left) to the southeast (right) direction. The sandstones, both in-situ brine- and gas-bearing are highlighted in blue and red.

observations provide a clue about the difference in burial history in even relatively small distances.

Figure 3.8 illustrates Iqbal (2016) observations for Myrsildre and Skalle. Additionally, we can observe that the velocities at Juksa are kept in a gentle gradient up to greater depths, suggesting that the more cemented and compacted rocks are encountered at greater depths than at the other wells. These differences are the product of the complex and varying burial history of this area, where diagenesis and tectonic events affect the rock properties in distinct ways, resulting in the properties that we observed today. Johansen et al. (2016) provide estimates for uplift for each of this wells based on sandstone diagenetic modelling and shale trends; the following estimates are based on sandstone diagenetic modelling: 1140 meters in Myrsildre, 1240 meters in Skalle and 875 meters in Juksa.

Figure 3.9 presents an overview of the well data for the Cretaceous and Jurassic formations Kolmule and Knurr, Hekkingen, Fuglen and Stø in the Myrsildre, Skalle and Juksa wells. The data that is plotted has been upscaled by using Backus averaging with a window of 15 meters.

Over-imposed are the rock-physics models for in-situ brine-saturated sandstones that describe the different sedimentological and diagenetic scenarios: the friable sand model at $20MPa$ (dashed black line), contact-cement model (solid red line), constant cement lines for 1% and 2% cement (dashed red lines) and the upper Hashin-Shtrikman or stiff-sand model (solid purple line). These rock-physics models allow us to identify patterns in the data when exploring the formations independently.

For the Kolmule Formation the brine sandstones are characterized by porosity ranges of 0.07-0.16 and P-wave velocities varying between 3.1-4.3 km/s. The porosity in the shaly sandstones facies fluctuate between 0.08-0.19 and P-wave velocities of ca. 3.1-4 km/s; shale porosities are found in the range of 0.06-0.16 with most of the velocities around 2.6-3.2 Km/s, and some shales with higher velocities (3.2-3.6) km/s in the porosity ranges of 0.12-0.14. On the other hand, porosity ranges between 0.15-0.19 and compressional velocities mainly in the range of 3.9-4.4 km/s are observed in the Knurr brine sands. Shaly sands in this formation are found to be in the porosity range of 0.06-0.16 with P-wave velocities of 3.7-4.2. The Knurr shales are found to have porosities between 0.01-0.11 with V_p oscillating between 3.1 and 4.1.

Regarding the Jurassic formations, the Hekkingen shales range in porosity between 0.01-0.13 and in P-wave velocity between 2.9-3.9 Km/s. In the case of Myrsildre, the rock-physics models suggest that these points (porosity of about 0.17-0.23 with velocities ranging between 3-3.6 km/s) have been erroneously classified as shales when in reality are sandstones. The Fuglen shales present porosity variations in the low-to-intermediate range (0.01-0.16) with V_p values between 3-4 Km. The Stø Formation is composed mainly of brine sandstone facies with porosity ranging between 0.11-0.19 and P-wave velocities between 4-5 km/s. The shaly sandstones facies fall in the porosity ranges of 0.07 to 0.16 with P-wave velocities in the range of ca. 3.8-4.5 km/s.

The following states and summarize some remarks from the observations described above:

1. The higher sandstone velocities in Knurr rather than in Kolmule can be a result of both quartz cementation and calcite cement, as described by Rodriguez (2015).

2. The friable sand model does not explain the brine sands at Kolmule level; the velocities indicates that cementation has occurred as they fall in the constant cement lines. Similarly, the shaly sands of Kolmule fall under these lines; these somehow high velocities could be explained either by the effect of pore-filling clay or diagenesis, or the interplay between them.

3. Shale facies also present differences between wells and formations. In the case of Kolmule, shales fall in the lower Hashin-Shtrikman bound. On the contrary, the Knurr shales at Skalle and Juksa fall under this line.

4. The Stø sandstones fall close to the stiff sand line. The sandstones at Juksa seems to have undergone more severe porosity loss due to lower porosity than their Myrsildre and Skalle counterparts.

5. The shaly sands in Stø have a lower velocity than the brine ones; this can be the effect of clay coating the grains, preventing higher degree of quartz cementation; however, this can not be said just by taking into account well logs. Additionally, at Skalle, part of the gas reservoir is made up of this shaly sandstones facies.

6. The misclassified sandstones in Hekkigen at Myrsildre coincides with the constant cement line; this is an indication of velocity and porosity being influenced by diagenesis.

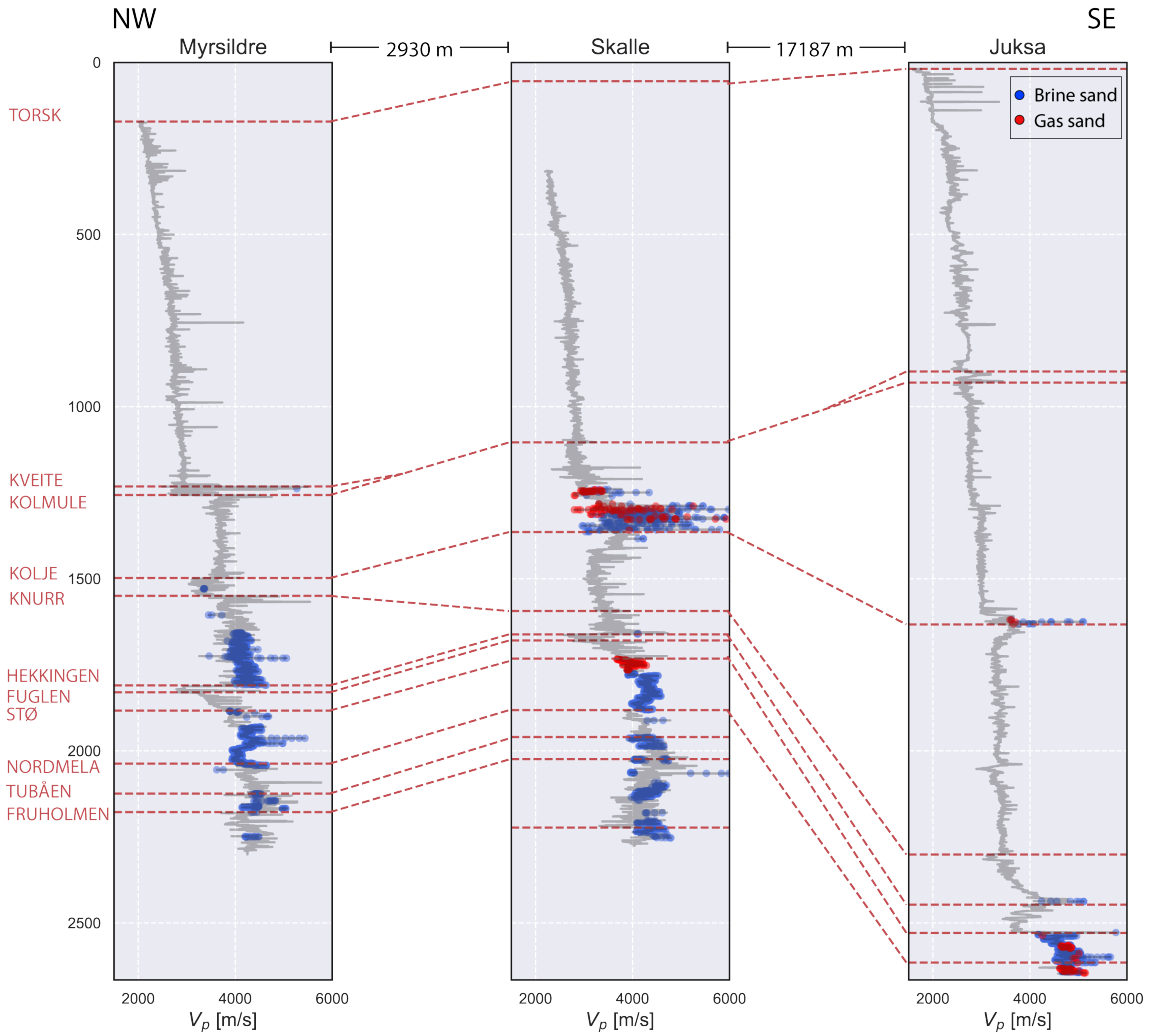

Figure 3.8: P-wave velocity for the three wells. The brine- and gas-bearing sandstones facies, as defined from the cutoffs of petrophysical logs, are highlighted in blue and red respectively. It is observed that there is a more rapid increase in velocity with depth at Myrsildre and Juksa than in Juksa. This difference is the result of diagenetic processes and uplift.

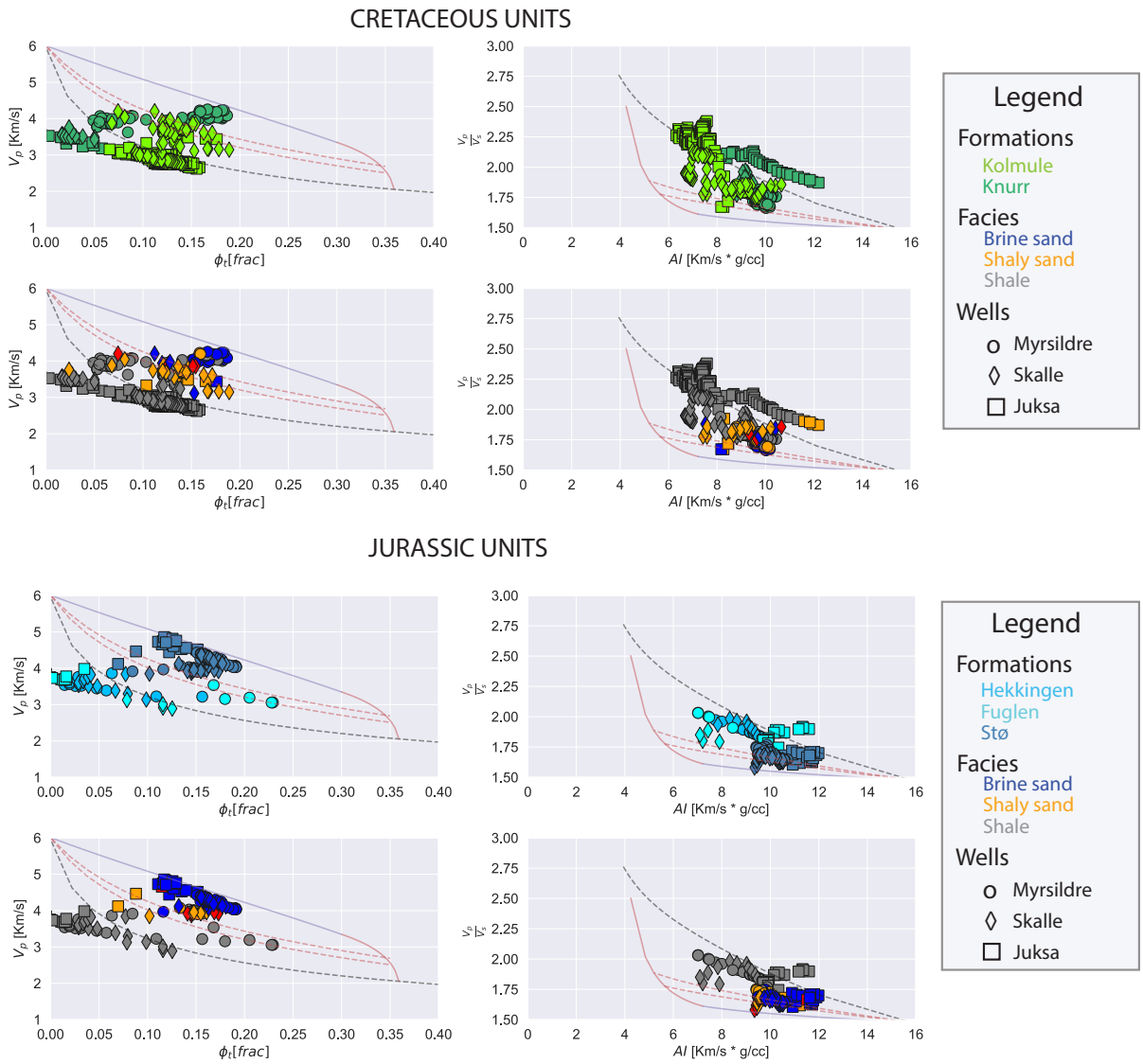

Figure 3.9: Upscaled well log data with superimposed rock physics models. The brine saturated friable sand, contact cement and stiff sand models are represented by the black dotted, red and purple lines respectively. The well log data in this does not include gas sand facies nor their fluid-substituted counterpart.

3.3 Seismic data

A provided composite seismic line in the Northeastern Hammerfest Basin with near, far, full-stack and intercept and gradient seismic data. Its location is displayed in figure 3.3, as well as the position of the wells along with the seismic. Figure 3.10 presents a quick overview of the seismic data available in this study. The seismic counts with an overall good quality, SEG normal polarity, and a frequency bandwidth of 8 to 42 Hz as illustrated in figures 3.11 and 3.12. The interpretations of the formations or intervals of interest are displayed in figure 3.12. These intervals are chosen because they represent essential elements in the petroleum system; either they conform seal or the reservoir rocks for the documented accumulations.

The composite section was made by Johansen et al. (2016) from a 3D survey. The near stack corresponds to angles from zero to ten degrees, while the far stack contains angle information between twenty to thirty degrees.The gradient was calculated by using Shuey (1985) approximation, assuming that $R(0)$ is the near stack and the far stack represent the reflectivity at 30^o (Johansen et al., 2016).

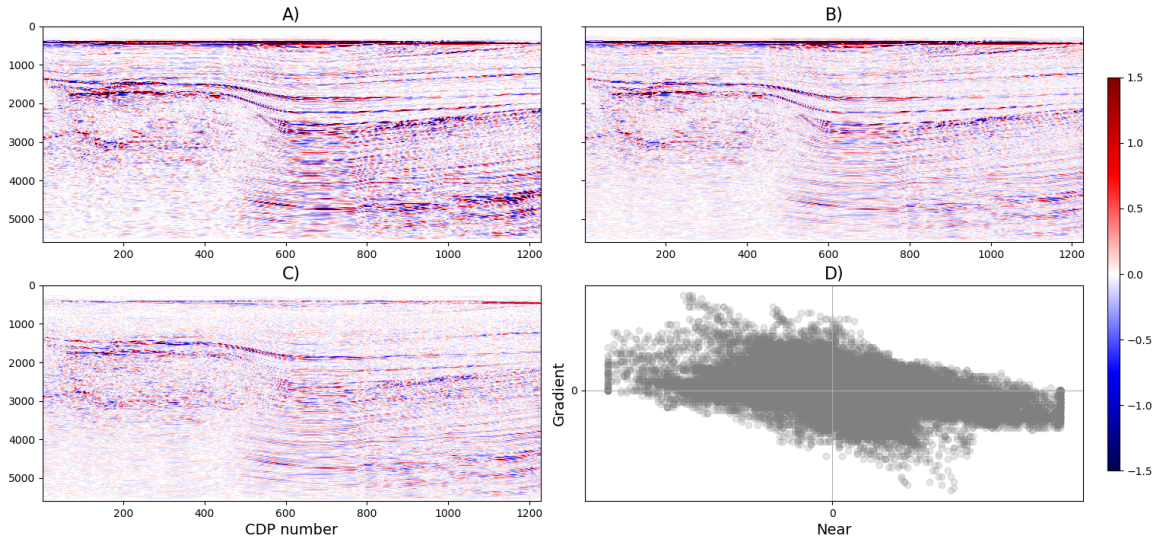

.

Figure 3.10: Seismic data available for this study. *A)* full stack, *B)* near and *C)* gradient sections. *D)* near versus gradient cross plot.

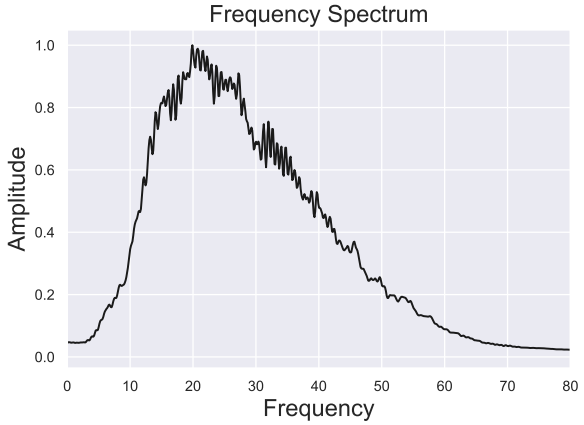

Figure 3.11: Frequency spectrum for the full stack seismic section.

3.4 Uplift estimation

Johansen et al. (2016) estimated the magnitude of uplift from an integrated analysis of shale depth trends and sandstone diagenetic modelling with seismic velocities. The uplift profile was provided along this study's seismic line, and it is displayed in figure 3.13. This profile is of a

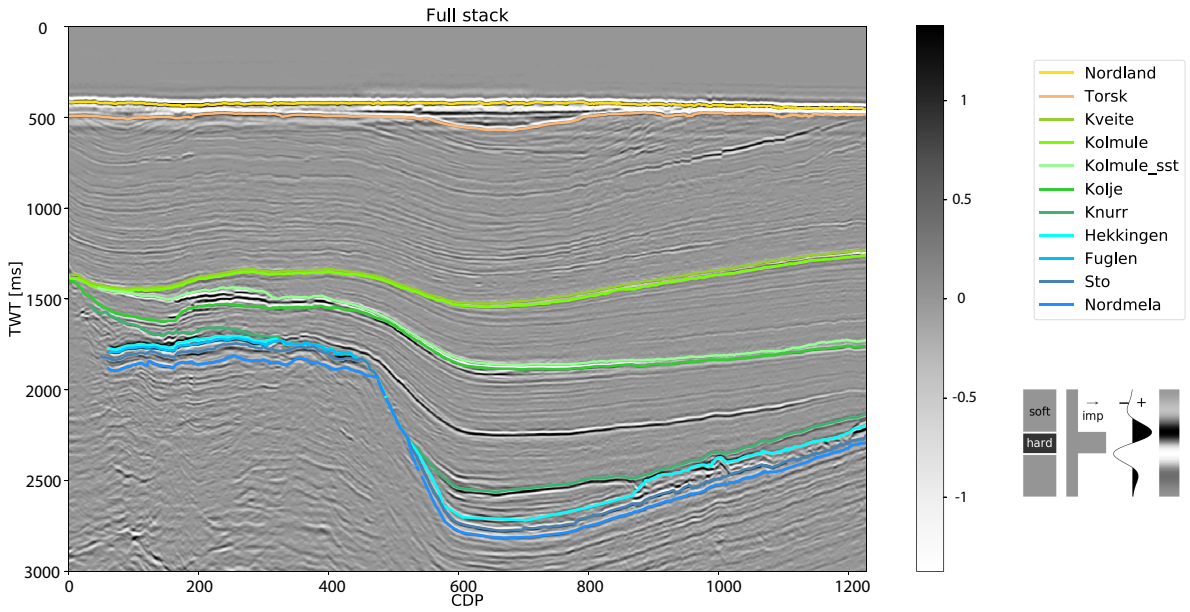

.

Figure 3.12: Full stack seismic section displaying the corresponding interpretations for the markers of interest.

critical source of information, as it provides the spatial variation for the maximum burial depth constraint in this work.

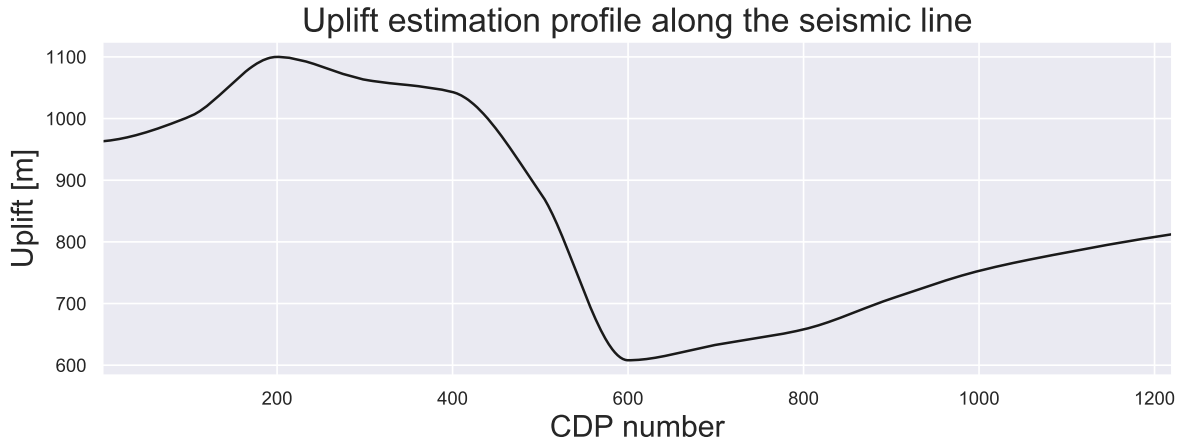

Figure 3.13: Uplift estimation profile along the seismic line from Johansen et al. (2016).

Chapter 4

Methodology

As a study case, the AvO signatures are studied along a seismic line. The impact that burial history and maximum burial depth have on these signatures represent an essential factor in complex areas as the Barents Sea. In order to reach the goal of this work, we propose an integrated workflow that takes into account information from different sources.

To model the rock properties along the CDPs in this seismic line, we use the methodology proposed by Helset et al. (2004) and Avseth and Lehocki (2016) to model sandstones. Concerning modelling shale properties, we follow a methodology similar to the one described by Storvoll and Brevik (2008). Different porosity, density and velocity shale trends were estimated at different scales in the Barents sea.

4.1 Sandstone Modelling

4.1.1 Porosity-depth trends modelling

The uplift estimation from Johansen et al. (2016) constrains the burial curves for each of the modelled formations. With this, it is possible to model the porosity-depth relationship through time. This model has to honour the different diagenetic processes that are dependent on pressure and temperature. Hence, porosity reduction due to mechanical compaction and cementation are accounted for jointly, as described by Helset et al. (2004) and Avseth and Lehocki (2016).

Section 2.2.1 describes a model for porosity loss in the mechanical compaction domain. The value of β was set to $0.06MPa^{-1}$ as Lander and Walderhaug (1999) suggested that it provides proper fitting with sandstones, IGV_f was fixed to 0.28 for all the sandstones.

Walderhaug (1996) described a kinetic model that allowed to simulate quartz cementation and the related porosity reduction after reaching the temperature of onset of quartz cementation, set to 70^oC in these models. The constants *a*, *b* in the model were set to the default values defined in Walderhaug (1996). The value for *d* in equation 2.4 was set to a default of 70^oC.The geothermal gradient was set up to $36^oC/Km$ and the temperature at the sea bottom to 5^oC based on estimations from (Johansen et al., 2016).

4.1.2 Rock physics-depth trend modelling

As it was described in **Chapter 2**, two rock-physics models were used to model the stiffness of the sandstone framework as a function of diagenesis (depth and temperature): the friable sand model (Dvorkin et al., 1999) and the contact cement (Dvorkin and Nur, 1996). By combining these two models, two trends can be captured, compaction and cementation, respectively.

In Dvorkin et al. (1999)'s model, the porosity loss is related to sorting deterioration, however, it can be assumed that the effect of mechanical compaction in grain packing is similar to changes in sorting (Florez-Nino, 2005; Avseth et al., 2010). Additionally, the friable-sand model corresponds to a constant effective stress, thus, in order for the model to be consistent with compaction, the model is calculated at different effective stresses (Blazevic et al., 2017). The effective stress is a primary rock stiffness control during mechanical compaction; this is implied from equations 2.11 and 2.12. Another important consideration is the interaction between the grains; this corresponds to friction or frictionless interactions. The former is introduced by a coefficent f (between 0 and 1), where $f = 1$ when there are perfect adhesion and $f = 0$ for frictionless contacts (Bachrach and Avseth, 2008; Mavko et al., 2020) (see figure 4.1).

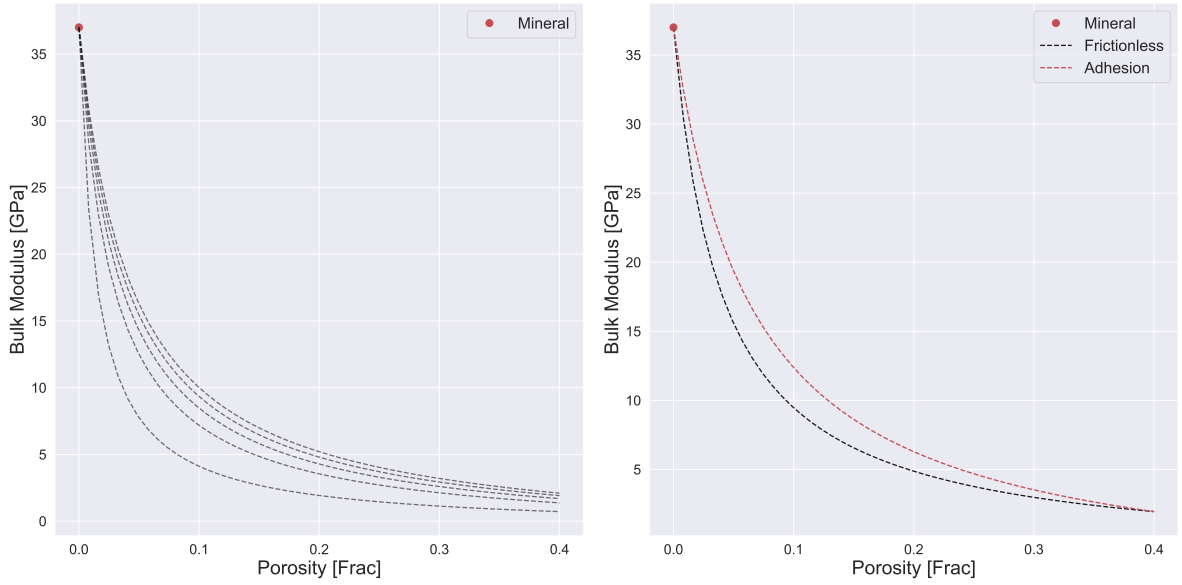

Figure 4.1: The left plot illustrates the pressure dependence of the friable sand model, and an increase in the pressure results in increasing stiffness. In the right figure, a comparison between the stiffnesses for the two-grain interactions at the contacts.

When the onset of quartz cementation is reached, the stiffness increases dramatically due to the welding effect of the cement at the grain contacts (Avseth et al., 2000, 2005). In this model, the critical porosity corresponds to the porosity when quartz cementation starts. It is crucial to have in mind that this model is valid for high-porosity sands. Thus, for modelling lower to intermediate porosities, the Hashin-Shtrikman Upper bound was used to interpolate to the mineral point (Avseth et al., 2005). Although in this work is not accounted, in the case of cracks present in the sandstones, an inclusion based model can be a more appropriate approach (Avseth et al., 2014).

Figure 4.2 illustrates the rock-physics methodology to diagnose the degree of compaction or cementation of a sandstone. This methodology intends to reproduce the effects that burial history, consequently temperature and pressure history, have on the porosity reduction and stiffness of the sandstones. The modified friable sand model (black line) represents the mechanical compaction process during burial. The model starts at critical porosity ϕ_c; in this case, 0.4, and the rock moduli are dependent on the *effective stress* as described in Hertzian contact theory . The stress is increasing as sediments are buried; thus, the velocity increases. Such an increase is characterize to be gentle. We see in the figure that this model stops when porosity reaches about 0.3. Here the temperature has reached the onset of quartz cementation, and the Hertzian theory is no longer representative of this process. The porosity at which this transition will happen is the result of the interplay of different factors since we choose to model mechanical compaction by using the IGV model proposed by Lander and Walderhaug (1999), the values chosen for the model result on this porosity value. The use of the IGV model simplifies the assumptions about the pore structure and pore-filling configuration. As it was demonstrated by Fawad et al. (2011), different mineralogical and textural (grain sizes, shape, sorting) configurations will affect the degree of compaction. From the onset of quartz cementation to porosity equal to 0.2, the moduli are modelled by the Dvorkin-Nur contact cement model (red line). This model provides a more severe increment on the moduli when the porosity is reducing during cementation. Because the contact cement model is only valid for intermediate-to-high porosity sands, the stiff sand model is used to interpolate from porosity 0.2 to the mineral point.

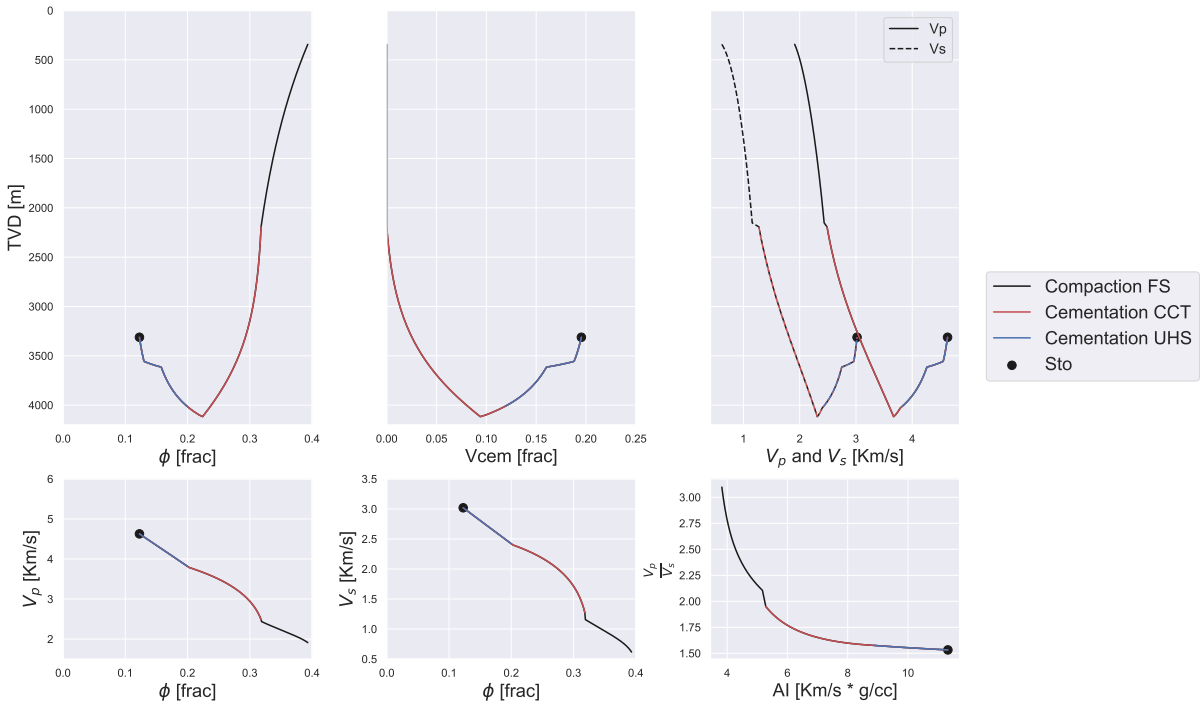

Figure 4.2: Rock physics-depth trends models. We can appreciate the porosity evolution during diagenesis (compaction and diagenesis). The diagenetic stages for which we have defined the rock-physics models are highlighted by the different colors. The velocities and elastic properties correspond to the brine-saturated case.

	$\rho[g/cc]$	K [GPa]	G [GPa]
Quartz	2.65	37	44
Gas	0.1	0.25	
Brine	1	2.5	

Table 4.1: Solid and fluid properties for estimating the dry and saturated rock modulus.

4.1.3 Stiffness of the saturated rock

The models explained above estimate the moduli for dry rocks. For being able to study the fluid effects on the moduli , hence the velocities, it is necessary to calculate the saturated bulk modulus for the modelled scenarios following the relationships described by Gassmann (1951).

The compressibility of the dry rock K_{dry} is described as the sum of the mineral (K_s) and pore space compressibility (K_ϕ) as:

$$\frac{1}{K_{dry}} = \frac{1}{K_s} + \frac{\phi}{K_\phi} \tag{4.1}$$

ϕ is the porosity. The bulk moduli for the saturated (K_{sat}) case can be expressed as:

$$\frac{1}{K_{sat}} = \frac{1}{K_s} + \frac{\phi}{K_{phi} + \frac{K_{fl}K_s}{K_s} - K_{fl}} \tag{4.2}$$

where K_{fl} is the fluid compressibility. We assumed that the saturation for both the gas or brine case was 100%, and the fluid properties for all the cases were constant. The solid and fluid properties are described in table 4.1

The saturated shear moduli (G_{sat}) will be equal to its dry counterpart (G_{dry}).

4.2 Well tie and depth conversion

In order to proceed with the depth-trend modelling, it is vital to have the seismic interpretations in the depth domain. Thus, we need to perform seismic-well ties and build a velocity model with which the horizons are depth-converted.

The three wells are tied to the seismic, from the sea bottom to the base of Stø. The wavelet estimation is statistical at the wells CDP positions. These wavelets are characterized by having zero phase, with frequencies ranging from $10Hz$ to $50Hz$ with dominant frequency at around $25Hz$ (Figure 4.3).

The synthetic seismograms generated by the convolution of the reflectivity series at well positions with the corresponding wavelet are matched to the seismic data. This procedure has been performed in Hampson-Russell software (CGG). Figure 4.4 illustrates the seismic well tie for Skalle. To do the ties, prior time-depth relationships for the Skalle and Juksa wells were available. (Figure 4.5).

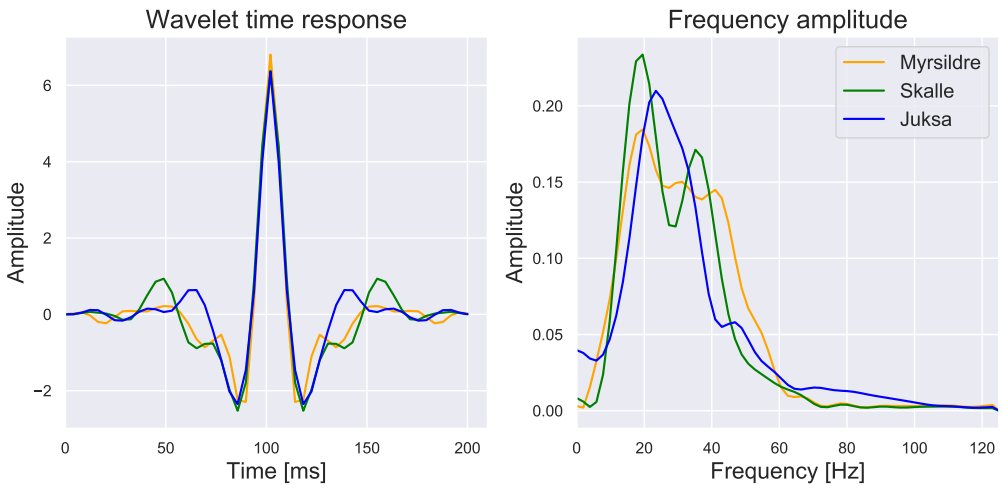

Figure 4.3: The figures illustrate the amplitude response in time and amplitude spectrum in the frequency domain for the three statistical wavelets extracted at well position (Myrsildre, Skalle, Juksa in orange, green and blue respectively).

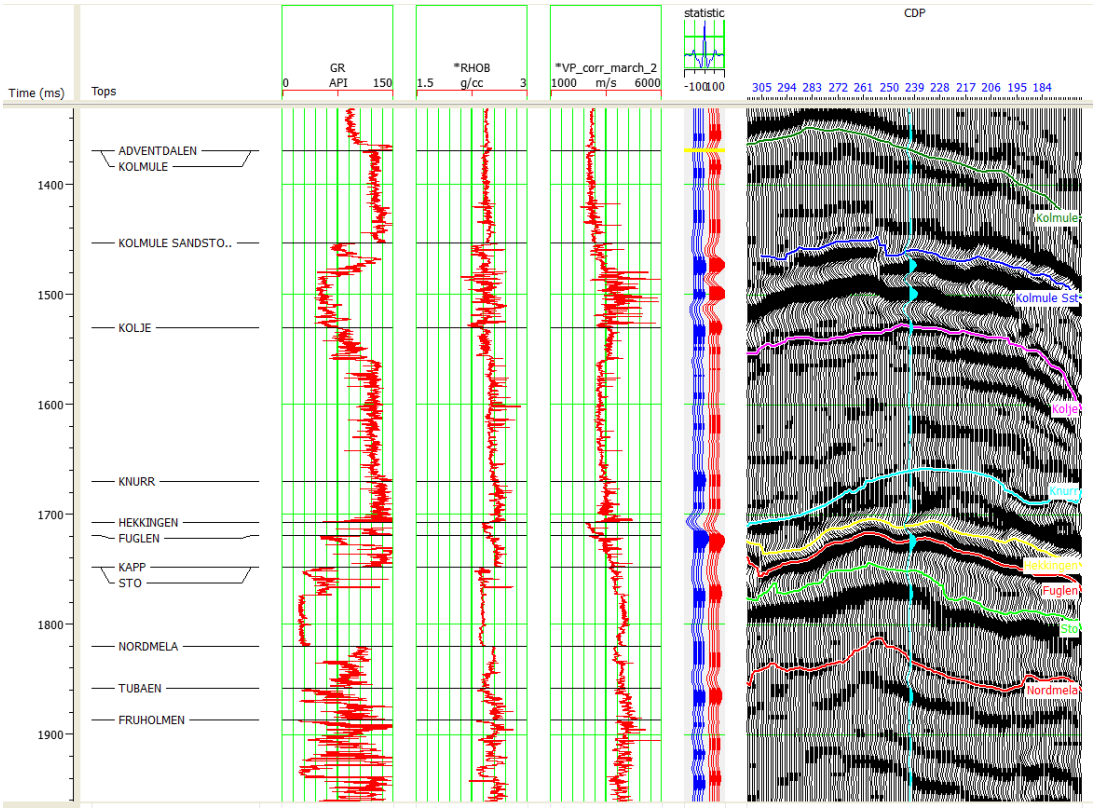

Figure 4.4: Seismic-well tie for Skalle. The cyan trace in the seismic display corresponds to the trace at Skalle CDP position.

The next step before converting the horizons to depth is to create a velocity model. Hampson-Russell allows building a model through the Strata module. The model is constrained by the seismic interpretations and the velocity model at well positions. These velocities, then, are interpolated constrained by the seismic and the interpretations statistically. The resulting interval

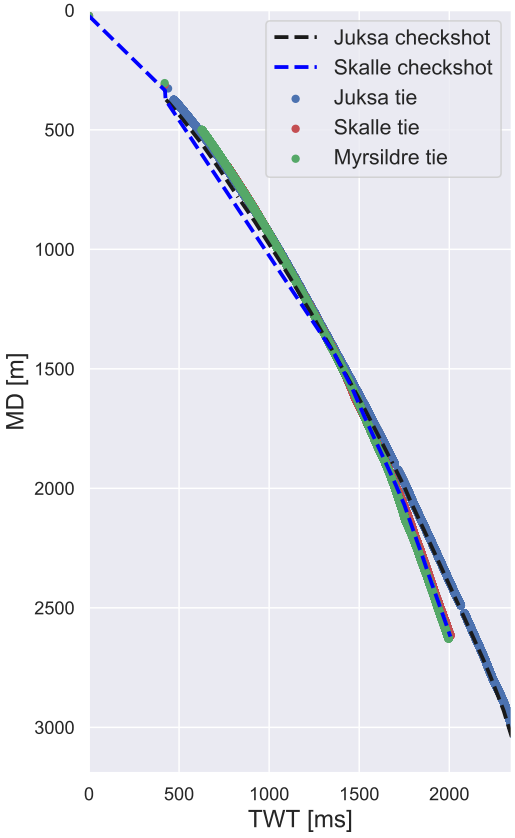

Figure 4.5: Comparison between the checkshots and the resulting time-depth relationships from the seismic-well ties.

velocity model is used for the horizon time-depth conversion (figure 4.6). This velocity field is smoothed, and a ray-tracing algorithm is used for the angle conversion.

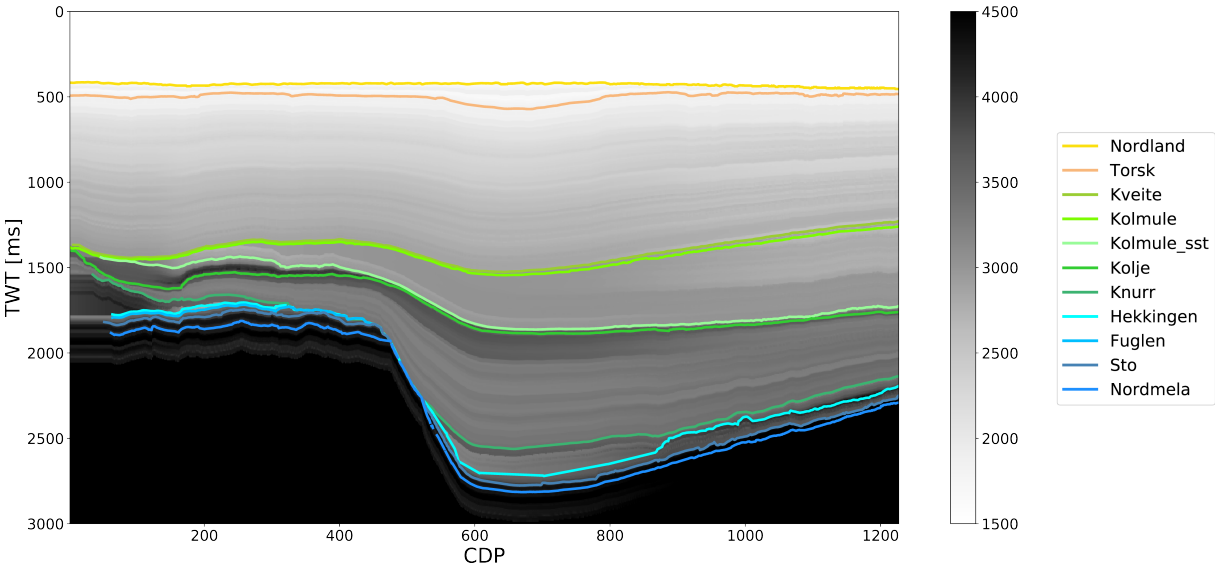

Figure 4.6: Resulting velocity model constrained by the horizons and the velocities after correction from the seismic-well ties.

4.3 Shale depth-trend modelling

Different authors have studied the effect that diagenesis (compaction and cementation) and uplift have on the physical properties of shales (for further reading see Djéran-Maigre et al. (1998); Japsen (2000); Storvoll et al. (2005); Mondol et al. (2007); Storvoll and Brevik (2008)). Mondol et al. (2007) argues that because of the complexity of mudstones and shales, the depth relationships for porosity, density and velocities can not be explained/predicted satisfactorily by a single universal relationship, and that these relationships are better represented by bands, rather than a single trend line.

For this work, we have available wells from different basins in the Barents Sea. As mentioned in chapter 3, the Barents Sea has experienced different episodes of uplift. However, there are significant differences in the magnitude depending on the geographical area.Therefore, we expect to capture different uplift effects depending on the origin of the data we analyze. In that sense, we explore the differences in the empirical shale trends depending on the scale (regional or local) included in such empirical relationships, as done previously by Storvoll and Brevik (2008). Consequently, we intend on capturing and separating the effects that regional or local burial history has on shale properties. Additionally, as there are available uplift estimations for several wells (see figure 4.7), we can observe the effect that correcting for it have on the trends. These estimations can lead to a more constrained understanding of the shale properties, resulting in better modelling, interpretation and decision making.

As mentioned above, we study the shale trends at different scales and their impact on shale properties with depth. The trends are estimated by simple linear regression; Giles et al. (1998) argues that a linear trend does not represent the curved trends at shallower depths and implies negative porosities from below a certain depth; however, since we are interested in greater depths, the linear trend assumption holds. Figure 4.7 illustrates the well locations for the corresponding scenarios used to construct the different shale trends (figure 4.8). The wells that are along the seismic line are excluded from the trends calculations; the remaining wells are grouped in 5 scenarios based on their vicinity (regional or local wells) and the correction for uplift ; thus, they are meant to capture different effects related to changes, for example, in burial history (different diagenesis) and mineralogy:

1. Scenario 0: correspond to all the wells available but the ones on the seismic line (orange dots).

2. Scenario 1: Correspond to the wells within the category of regional wells. These trends are going to be affected by differential uplift that characterized the Barents Sea. Seventy wells are in this category.

3. Scenario 2: These wells are in the vicinity of the studied seismic line and wells. The eight wells are located within the Tromsø and Hammerfest Basins.

4. Scenario 3: This scenario groups all the wells except the wells that are corrected by uplift. The trends in this scenario are estimated from fifty five wells.

5. Scenario 4: We apply the uplift correction suggested by Johansen et al. (2016) to these wells, representing an approximation of the maximum burial depth. This approach has

been done previously by Storvoll et al. (2005) for some wells in the southwestern Barents Sea.

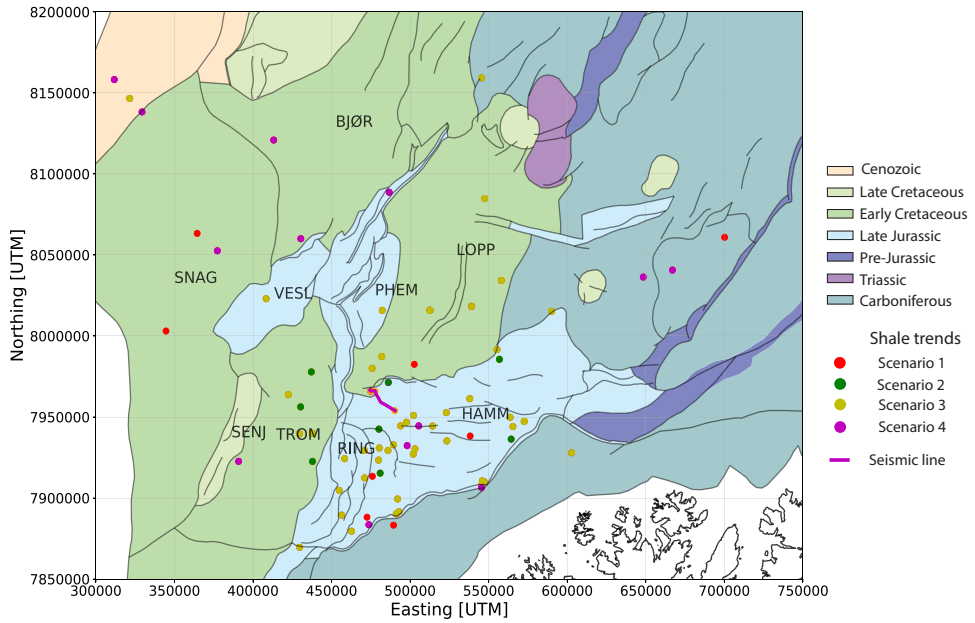

Figure 4.7: Map of the study area highlighting the wells used for each of the scenarios for the shale depth trends estimation.

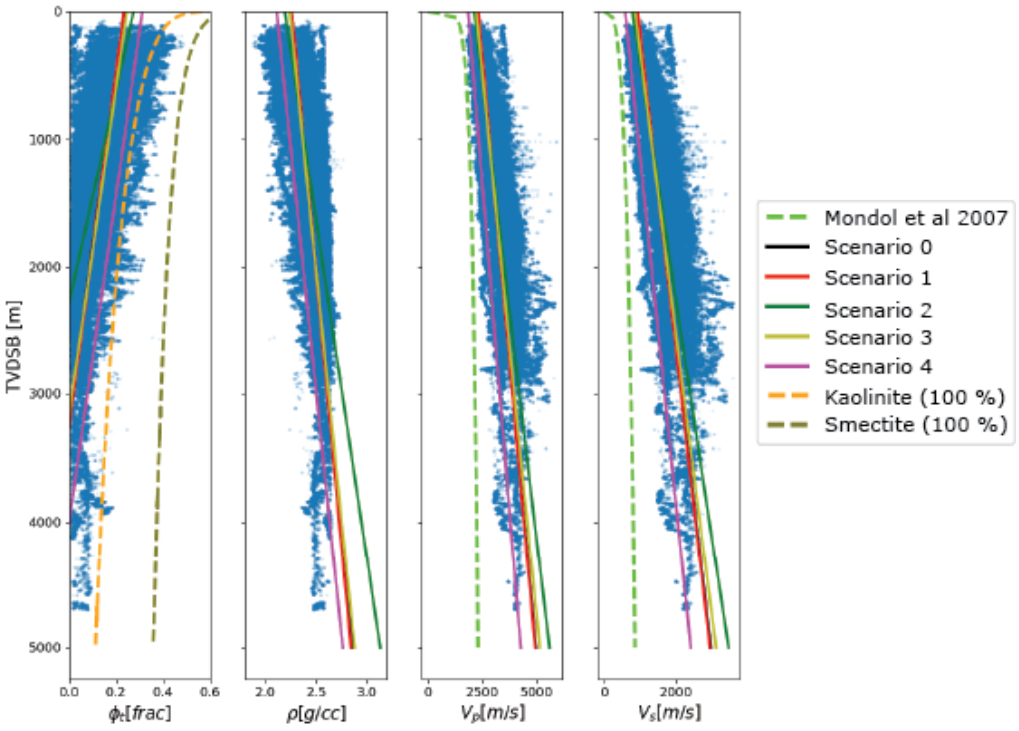

Figure 4.8: Shale properties-depth trends calculated for each of the different scenarios. Overimposed are the trends of compaction for kaolinite and smectite (porosity) and the least square approximations for velocities of brine saturated clay mixtures from Mondol et al. (2007) .

4.4 Burial history constrained rock-physics modelling

As mentioned in the introduction of this chapter, the methodology followed in this study is based on the work of Helset et al. (2004); Avseth and Lehocki (2016). The burial history of each formation constrains the models described in 2.2 and 4.1.2. The horizons studied in this work are illustrated in the present-day depth, as well as at their maximum burial in figure 4.9.

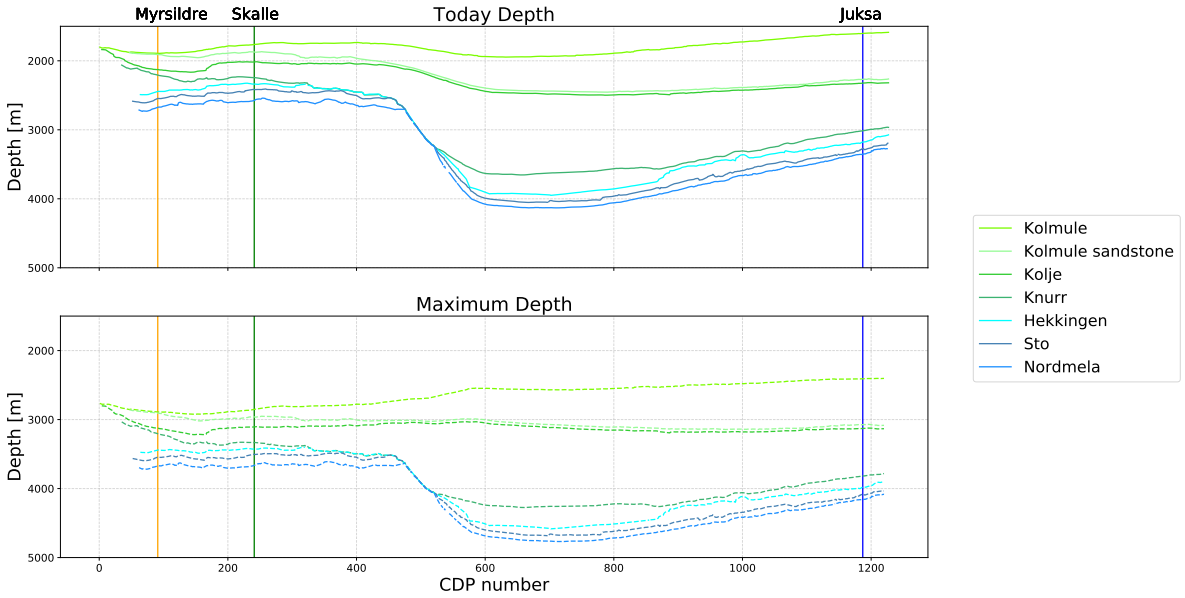

Figure 4.9: The figure above displays the depth converted horizons corresponding to the formations/interval of interest in this study. Below, these horizons are displayed at maximum burial.

Variation in the burial history can be expected as the result of differential basin development within and between the basins. In this work, we intend to honour at some degree these variations by including the uplift/net erosion estimations by Johansen et al. (2016). By doing this, the burial history is constructed in a way that honoured the maximum burial (figure 3.13). As a basis for the burial history construction for this study, we take some considerations from the work of Baig et al. (2016); it is suggested that the maximum burial in the southwestern BarentsSea may have taken place at some moment during the Oligocene, or even early as in the Eocene. Regarding the exhumation, we took into account both glacial and pre-glacial erosion. For simplicity, we assumed that magnitude of the erosion occurred evenly at each of these stages. Figure 4.10 summarizes the burial, temperature and stress history for the horizons of interest at three different locations that correspond to Myrsildre, Skalle and Juksa wells. The temperature and stress history is based on the considerations described in section 2.2. Additionally, the pressure is assumed to be hydro-static.

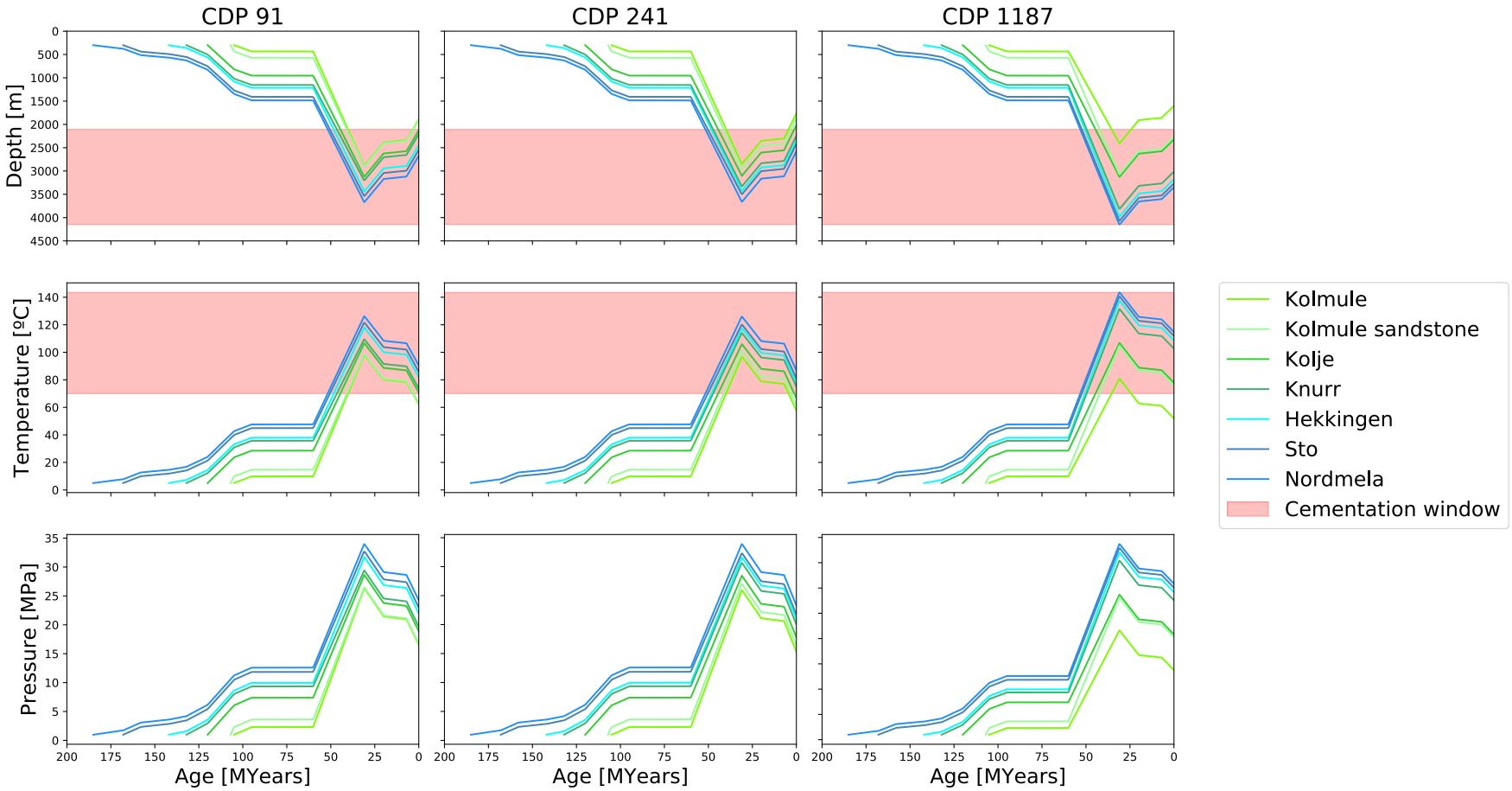

Figure 4.10: Burial, temperature and pressure evolution through time for the formations of interest at three CDPs corresponding to the studied well positions. The red area corresponds to the quartz cementation window which onset was set to 70º C.

These burial curves are required for the compaction/cementation modelling, and they are intended to constrain the rock-physics and subsequent AvO modelling. We consider some underlying assumptions when modelling sandstone and shales:

1. After cementation starts, the effect of compaction on porosity reduction is neglected (Bjørlykke and Jahren, 2010). This assumption is also valid for velocity modelling, since the contact-cement model (Dvorkin and Nur, 1996) does not account for pressure in this model.

2. Porosity reduction in sandstones is irreversible. In reality, exhumation is accompanied by a decrease in *effective stress* due to overburden unloading. Such stress relaxation could cause the rock frame to be more brittle, which can result in micro fracturing (Doré et al., 2002).

3. If the modelled sandstone underwent diagenesis and the subsequent uplift cause the temperature to drop below 70^{o}C (onset of quartz cementation), the velocities are modelled using the *stiff sand model*. However, the contact theory models do not capture the effects related to the cracks resulting from the stress relaxation. Additionally, the *stiff sand model* is not stress-dependent. Bredesen et al. (2018) provided a rock physics workflow for uplifted reservoirs that interplay contact theory and inclusion models based on the "Kite model" described by Avseth et al. (2014).

4. Shale porosity and velocities are assumed to be irreversible, which means that, in case of uplift, the properties correspond to when they are at the maximum burial. This consideration comes from having empirical relationships for shale properties and not a physical model that accounts for crack effects or the decrease in *effective stress*. We have chosen to use empirical relationships rather than physical models due to the high complexity when modelling shale compaction and diagenesis (see Mondol et al. (2007); Nooraiepour et al. (2017)). The empirical relationships are meant to capture the effects of these factors with fewer assumptions of the input data, i.e. mineralogy, clay particle arrangement, and diagenetic reactions.

Having in mind these considerations, we proceed with the modelling the rock physics properties-depth trends constrained by burial history. Figure 4.11 illustrates the modelling steps for Kolmule and Stø at the three wells CDPs locations. The three wells are plotted and their properties where up-scaled using Backus averaging of 15 meters. In this model, we assumed a mineral mixed consisting of 90% quartz, and the rest 10% equally divided between illite and smectite, the 10% of the clay is considered as clay coating for the Cretaceous formations. Conversely, for the Jurassic Formations, the mineralogy is assumed to be made up entirely of quartz. The minerals moduli and the parameters used to model the sandstones are found in tables 4.2 and 4.3. The resulting models correspond to the tops of both Kolmule sandstone and Stø formations, and the shales correspond to the overlaying Kolmule shales or to the base of either Hekkingen or Fuglen formations respectively. In this case, the sandstone velocities correspond to the brine-saturated case.

As it is seen in the figure 4.11, in the Kolmule sandstone models, the porosity and rock physics properties do not agree with the well observations. The variability can be explained by the model parameters since the modelled sandstones represent the well-sorted end member for

Mineral	K [GPa]	Gs [GPa]
Quartz	37	44
Illite	39.4	11.7
Smectite	17.5	7.5

Table 4.2: Mineral moduli constants used to model the solid for the sandstone grains.

	Ks [GPa]	Gs [GPa]	Diameter [mm]	Coating [frac]	Phic [frac]	m0 [frac]
Cretaceous	35	31	0.3	0.1	0.4	0
Jurassic	37	44	0.3	0	0.4	0

Table 4.3: Input parameters for modelling sandstones

clean sandstones as it is suggested by Avseth and Lehocki (2016) in the case for *Skalle*.Regarding the shales, the predictions underestimate the porosity slightly and overestimate the velocities. This deviation can be explained by the shales in Kolmule formation to be softer in this area; instead, the trends from which this model is derived can correspond to more compacted and stiffer shales.

In the case of Stø, it is observed that the porosity and P-velocity match nicely. The over-prediction in shear velocity can be related to the effects of cracks on shear modulus, which is not accounted for in this model (see Bredesen et al. (2018)). Concerning the shale properties, they provide a good match with the shales from the Hekkingen and Fuglen formations, that correspond to the cap rock for the Stø sandstone. In the $AI\ VpVs$ space, the modelled underestimate the $VpVs$ ratio. It is essential to notice that for this formation the cementation plays a significant role in the porosity degradation, taking the rock to the range of low to intermediate-porosity that are modelled with a modified Hashin-Shtrikman Upper bound (Avseth et al., 2005).

Now that the model assumptions and methodology is understood and calibrated, we proceed to model sandstones and shales at different CDPs along the seismic line for each formation. Under the consideration that there is a shale/sandstone interface at all the analyzed horizons, this methodology provides a screening expected signatures or a ”what if” tool for testing, understanding and predicting the different variations of properties that can be expected in an area when exploring, and assess the degree of uncertainty. Although this assumption is not strictly correct, especially for the Hekkingen and Fuglen formations that correspond to cap rocks, some lateral changes of facies can happen, giving validity for the use of this methodology.

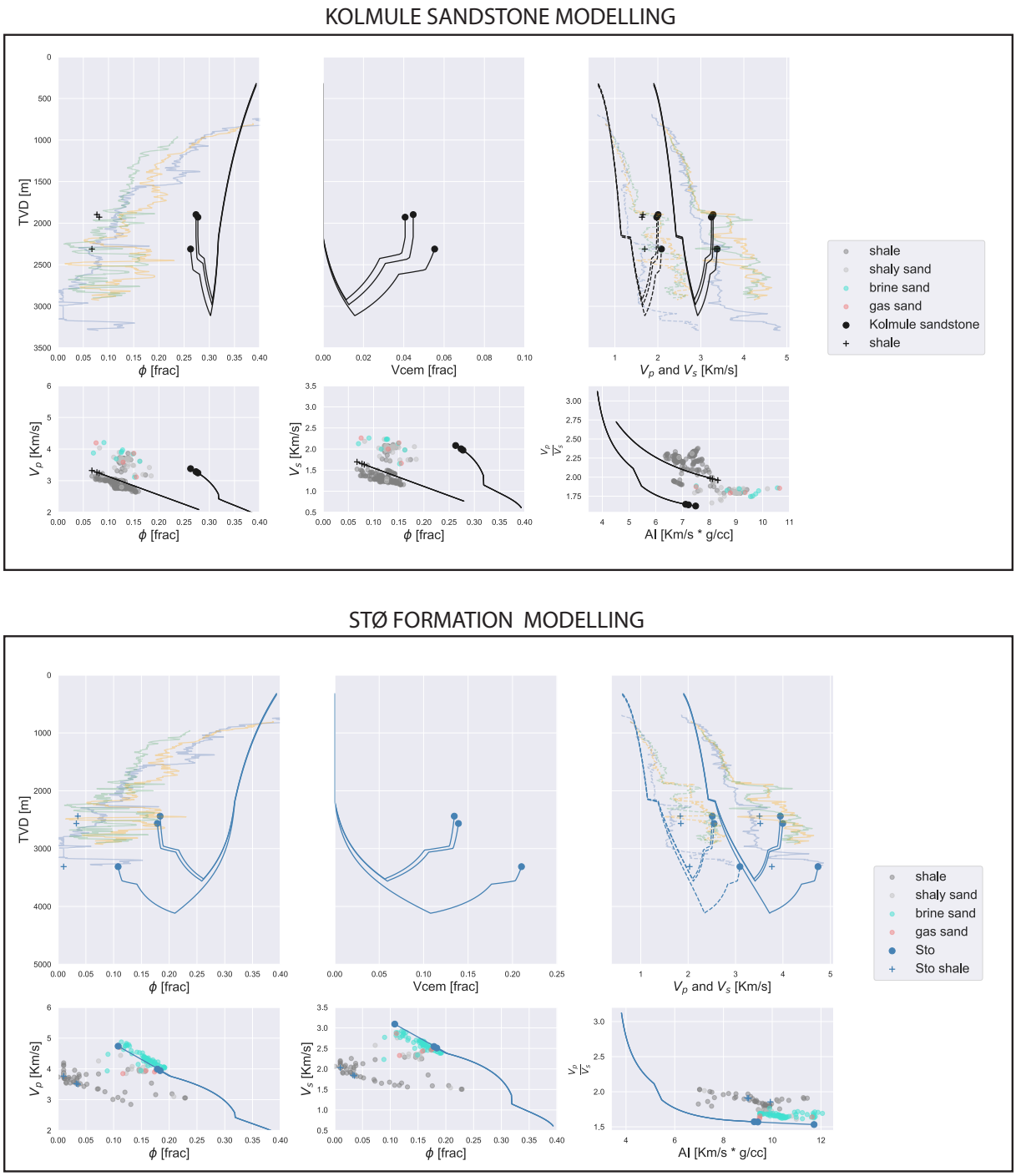

Figure 4.11: Calibration models for the lower Kolmule sandstone and Stø formations. The up-scaled well log data is plotted to compare with the models.

The next natural step after having the rock physics properties for both sandstones and shales, is to model the AvO responses for the different shale/sandstone interfaces. Figure 4.12 illustrates the expected AvO attributes and classes at the well positions in these two reservoirs. For Kolmule, *AvO class IIp* are observed at all the positions in the brine case. However, as seen in figure 4.11, the acoustic impedance is underestimated for the sandstones and overestimated for the shales. Respecting the velocities ratios, they seem to be underestimated in both facies at a similar degree. Thus, these would affect at a higher level the intercept, theoretically shifting the

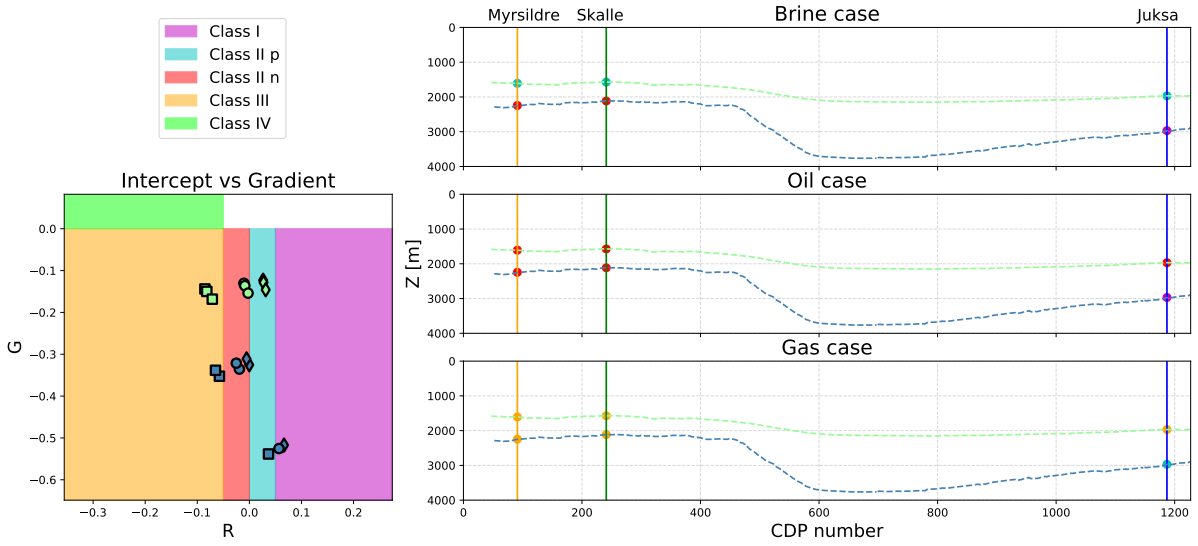

Figure 4.12: The cross-plot at the left corresponds to the intercept and gradient space. The background colors correspond to the AvO classes. The brine-, oil- and gas-bearing cases are represented by the diamond, circle and square markers respectively, for both Kolmule (green) sandstone and Stø (blue) formations at the three well locations. The three plots at the right correspond to the AvO classes varying with depth and wells CDP positions for each one of the fluid cases.

modelled interfaces towards more positive intercepts meaning that *classes I* could be expected. With regards to the other fluid cases, we see that at all three well locations, there is a shift towards negative intercepts when changing the fluid content. Thus, *classes IIn and III* are anticipated for oil and gas- saturated sandstones, respectively.

Regarding the AvO signatures for o, we see classes *I* and *II n* for the brine- and oil-bearing reservoirs. In the gas-bearing case, we observe classes *III* and *II p*. The classes *II p* are observed in Juksa, where the formation underwent higher quartz cementation, resulting in a stiff and low-fluid sensitivity reservoir. In Myrsildre and Skalle, the oil-saturated sandstones are expected to be class *II n* and the gas-bearing ones class *III*.

This methodology will be extended to most CDP positions for all the formations of interest. With this, we can predict the expected AvO class at any position along the seismic line, allowing to experiment with different sedimentological, fluid types and saturation scenarios with the aim of understanding and forecast the seismic amplitudes of the area.

4.5 AvO calibration

In order to compare the modelled AvO signatures to the seismic data, we need to match the probability density distributions (PDFs) of the seismic data and the modelled AvO data. To do so, we use a global scaler method. The script to do so was provided by Lehocki (2010).

The method consists in estimating the root mean square level of the intercept and gradient attributes for both the seismic and modelled data. Since we are interested in identifying the outliers (sandstones with different fluids), the model data used for the calibration correspond

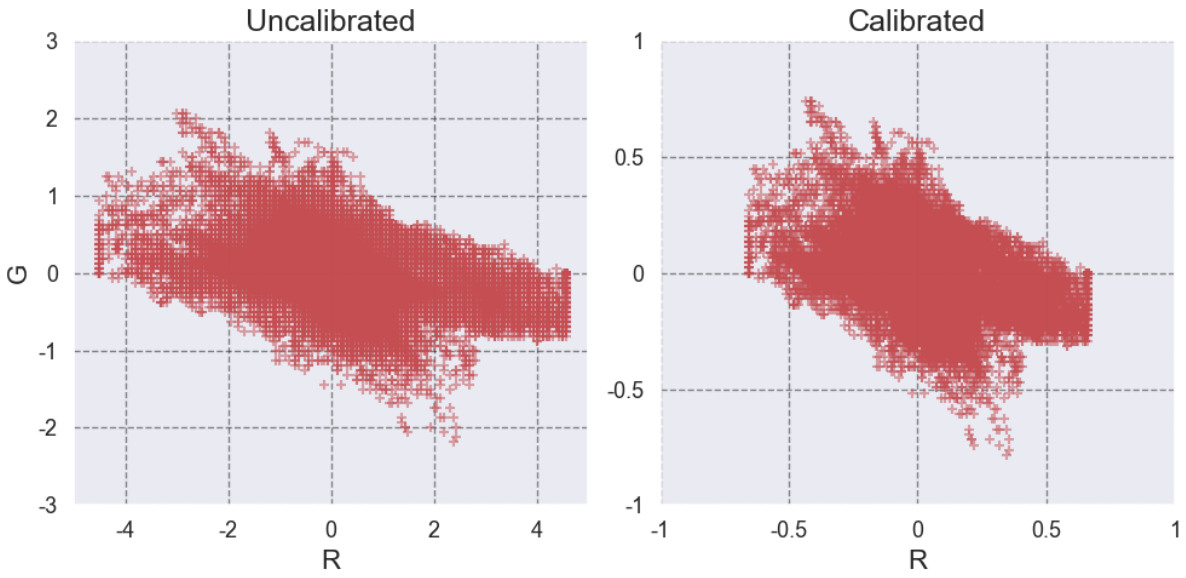

Figure 4.13: Uncalibrated and calibrated AvO data

to the background trend or shale/shale interface. Then we estimate a global scalar based on the *RMS* of the intercepts and a scalar for the gradient that includes the gradient *RMS* and the global scalar. Finally, we apply these operators to the actual intercept and gradients to obtain seismic data matching with the models. Figure 4.13 presents the uncalibrated (left) and calibrated (right) AvO data.

$$S_{global} = \frac{RMS_{Imodel}}{RMS_{Iseismic}} \tag{4.3}$$

$$S_{gradient} = \frac{RMS_{G_model}}{S_{Global} * RMS_{Gseismic}} \tag{4.4}$$

$$I_{calibrated} = I_{seismic} * S_{global} G_{calibrated} = G_{seismic} * S_{global} * S_{gradient} \tag{4.5}$$

Chapter 5

Results

5.1 Shale depth-trends

As discussed in the section above, the shale trends were estimated for the different properties under distinct scenarios. These scenarios are based upon geographical (vicinity) and geological history (uplift correction) considerations.

From the different scenarios, three sets of trends are identified; a lower bound corresponding to scenario 4 which the wells have been corrected by uplift; an upper bound represented by scenario 2 (local or wells nearby the area of interest). Lastly, the scenarios that included regional data (Scenarios 0, 1, 3), have similar depth trends for the shale properties and fall between scenarios 4 and 2 trends. In figures 5.1 and 4.8 we can observed that in the case of the upper bound (scenario 2) the changes in the properties occurs rapidly; whereas in the lower bound the property changes are more gentle. Although it might seem intuitive to use local data, it is crucial to understand the effects that regional geology has on a local scale, especially when there is lack of data and general knowledge in the vicinity and the area of interest.

A possible reason for scenarios 0,1 and 3 to fall between the bounding trends 2 and 4 might be found on the ”mix” of the different recorded events in the above scenarios. Trends 2 record anomalously low porosity and high velocities at shallow depths as they are the result of a high degree of diagenesis and subsequent uplift. On the contrary, scenario 4 correspond to the uplift corrected wells. Thus, the rocks that underwent diagenesis and subsequent uplift are now located in their maximum burial depth. This correction will provide a better understanding of the actual effects of burial in the shale properties.

Figure 5.1 compares the effect of the depth-trend modelling at the top of the Kolmule, Hekkingen and Fuglen Formations shales in Skalle and Juksa wells. The well log data for these formations is color-coded with the volume of clay values (Vclay). We see that scenario 4 is approximating the shales with higher Vclay. This observation is correct for the two intervals of interest. Because of the better agreement with the well data, from this point on, we use the trends obtained by scenario 4 to estimate the shale properties for the AvO analysis.

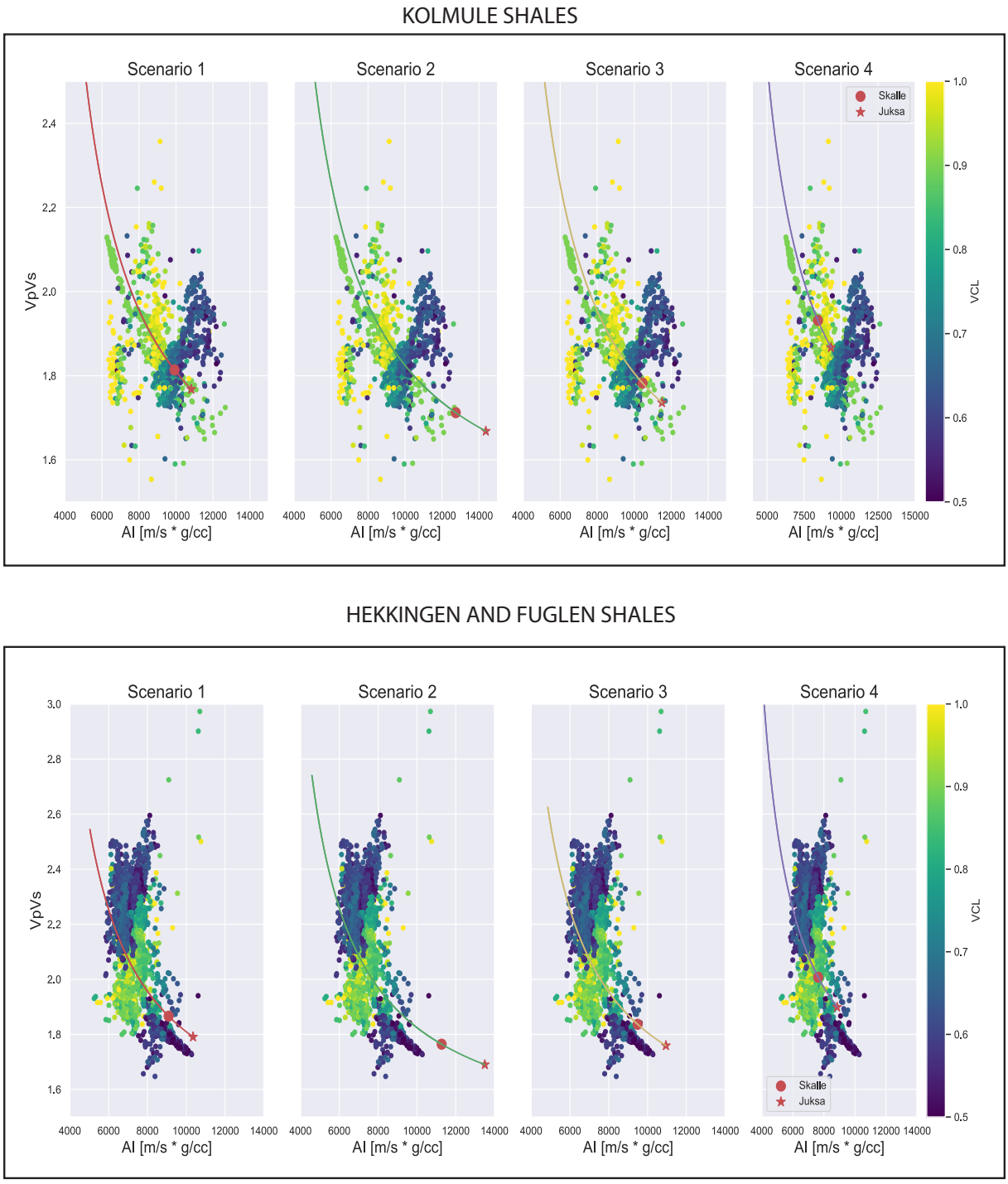

Figure 5.1: Shale trend comparison for both the capping shales for Kolmule and Stø sandstones. The lines correspond to the shale trends for the different scenarios; the star and circle represent the property estimation at the top of the sandstone/ base of shale at Juksa and Skalle, respectively. The capping formations are Kolmule (above), Hekkingen and Fuglen shales (below) at the three wells. The well measurements are plotted with clay fraction as color code.

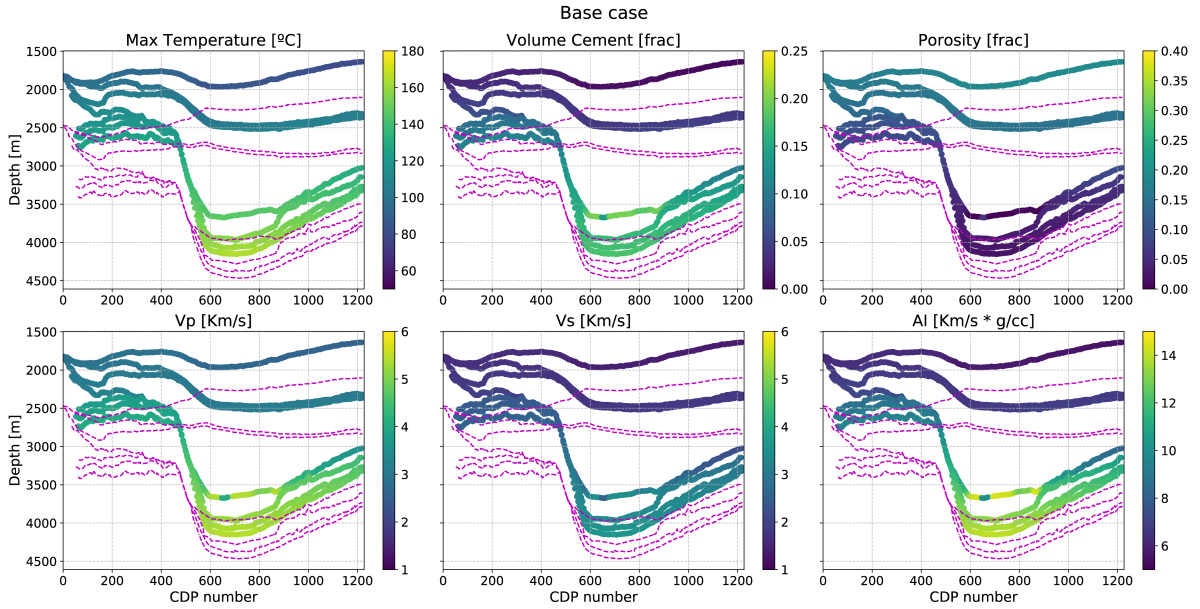

Figure 5.2: Sandstone properties for each of the horizons of interest. The properties values are represented by the color bar. The magenta dashed lines correspond to the maximum burial depth for each of these horizons.

5.2 Rock-physics and AvO modelling

From the joint diagenetic-rock physics modelling, we were able to obtained sandstone property *"sections"*; this allows depicting the spatial variation of the sandstone physical properties and their link with the burial history. We can observe the controlling role that the maximum burial (maximum temperature), have on the rock physics properties.

Figure 5.2 illustrates different properties sections along the modelled horizons, highlighting the dependency they have on burial history. This case corresponds to the provided uplift profile. We can observe the difference between the depths at which the horizons are now, and when they were a maximum burial (magenta dashed lines). This difference is especially noticeable in the Cretaceous strata where we at the first CDPs today's depth reflect a structural high and at the lasts CDPs they are found in a deeper position. However, at the maximum burial, what is now a structural high was actually at greater depths, resulting in higher compaction or even higher degree of cementation that at the other end. We will discuss later the implications that have the narrow shelf towards the Loppa High being presented as a depocenter at their maximum burial according to the uplift estimations.

The subsequent step is to model the AvO response and its classification to provide AvO classes sections. These sections show the expected variability of the AvO signatures if we assume the same lithology along the horizon. As it is appreciated in figure 5.3, there is a clear diagenetic/burial trend accompanied by decreasing fluid sensitivity. Because the Cretaceous rocks have been modelled using different parameters than the rocks of Jurassic age, their slopes are slightly different. Additionally, to compensate for the overestimation in the Cretaceous shale properties, as mentioned in chapter 4, the modelled density has been reduced by 25%.

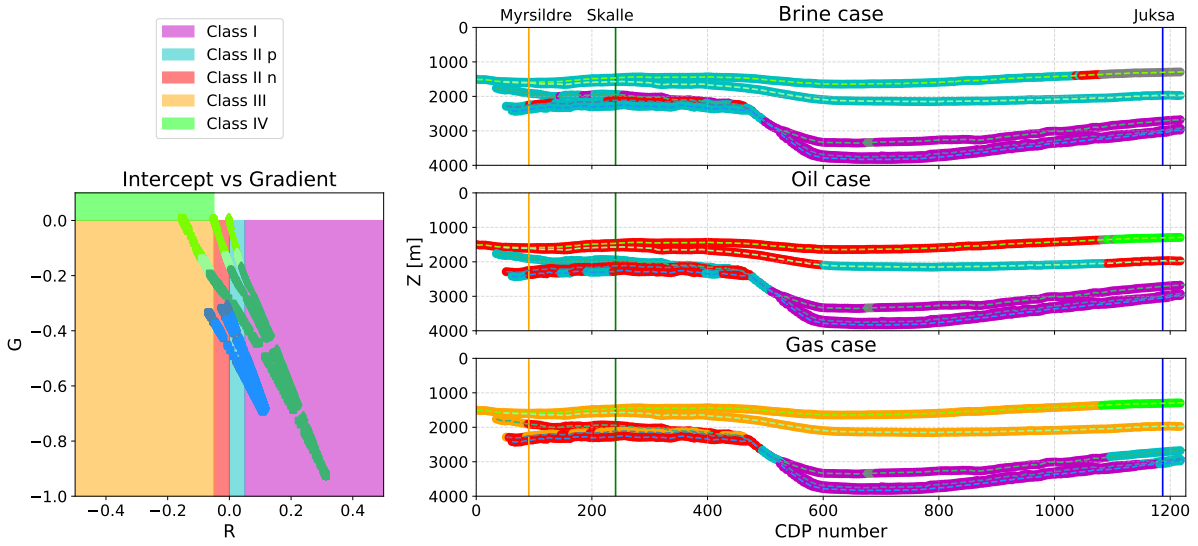

Figure 5.3: The crossplot in the left corresponds to the AvO attributes for all the formations at different positions. The colors of these points correspond to the colors assigned to each formation (see figure 3.12). Additionally, the brine-, oil- and gas-bearing cases are represented by the diamond, circle and square markers respectively. To the right, the expected AvO classes for the three different fluid scenarios.

The gradient goes from weak positive in top Kolmule to strong negative at the top of Nordmela; the intercept, on the contrary, goes from negative to positive. This trend is accompanied by a decreasing fluid sensitivity with increasing burial. We observe that weaker gradients and higher fluid sensitivity mostly characterize the Cretaceous strata. The exception to this is the Knurr Formation. The top Kolmule displays mainly class IIp for the brine saturated case and variations to class IIn and III for oil- and gas-bearing sandstones. For Lower Kolmule the brine case provides a general class IIp; the oil case present classes IIn to the west and the east, and IIn in the middle of the section; a class III is expected for the gas case. The Knurr Formation corresponds to the more varying fluid-sensitivity in the Cretaceous formations ranging from classes I and IIp in the brine and oil case and classes I, IIp, IIn and III in the gas case.

On the other hand, the Jurassic rocks exposed classes IIp and IIn towards the Loppa High and varying spatially towards Juksa to become classes I for the brine case; classes I are encountered in a structural depression where the maximum temperatures were reached, and the rocks have undergone more dramatic diagenesis. The expected classes for the oil case at Loppa High are IIp and IIn, and in the basin and towards Juksa classes I are expected. The gas case present variations mainly for Stø towards the Loppa High, displaying mostly classes I and minor classes IIn, towards the basin classes I dominate and becoming IIp towards Juksa. For Nordmela a similar behaviour is expected, but towards the Loppa area classes IIn are predominant.

5.2.1 Uplift sensitivity

Although we have an uplift profile estimation available, that is not always the case, especially in unexplored and unknown areas. Additionally, these estimations are not exempt from uncertainty. Therefore we modelled three additional cases to understand how sensible the properties are

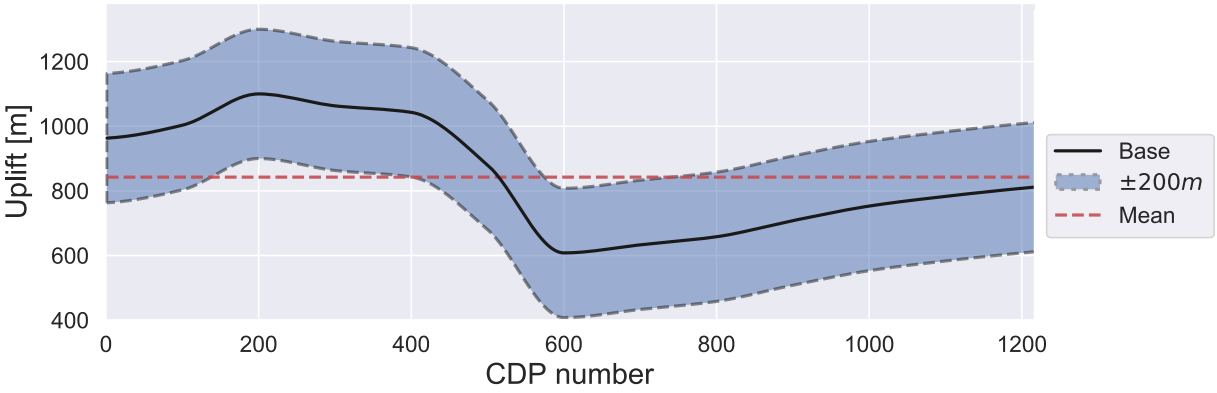

Figure 5.4: Uplift scenarios used to evaluate the sensitivity of the models. The solid black line correspond to the base case, and the uncertainty of $\pm 200m$ is represented by the grey dashed lines and the blue area. The red dashed line correspond to the mean uplift of $842m$.

to variations in uplift: one assuming a constant uplift at all locations, and two based on an uncertainty of 200 meters, resulting in 200 meters up or down of the provided uplift profile (*see Figure 5.4*); this yields a sensitivity analysis for the effect of uplift on rock properties. Figure 5.5 presents a comparison between the changes in properties relative to the base case (see figure 5.2) for each one of the alternative uplift cases. The dashed purple lines correspond to the horizons at maximum burial depth to help to understand the cause of the variations in the sandstone properties. Similarly, figure 5.6 presents the AVO sections for each of the alternative uplift cases.

In the first case (figure 5.5a), corresponding to 200 meters of uplift over-estimation, the higher variations are encountered in the top Kolmule horizon in the central part. which in the base case did not enter in the quartz cementation window.However, the added 200 meters to the maximum burial were enough for cementation to start resulting in higher velocities and impedance. In the Jurassic rocks, the higher variations are encounter towards the Loppa High, where more intense diagenesis has taken place in this scenario, although significant variations occur toward Juksa. Consequently, we see that there are variations in the AvO signatures (figure 5.6a). The most notable variations are seen in the Jurassic rocks, where the fluid sensitivity has decreased (especially at Juksa location where no change in classes occurs for the different fluid cases). Additionally, A general change in class IIp to IIn for the oil case in the Kolmule sandstone horizon is observed.

On the other hand, as illustrated in figure 5.5b, the underestimated case shows substantial variations at the top of Kolmule towards Skalle, such changes can be the result of the sandstones this depth to not being in the window for quartz cementation and experience lower effective stress. For the other Cretaceous intervals, there is a relevant difference in porosity; the velocities change are more evident in the shear velocity. Considerable variations are noted towards Juksa for the Lower Cretaceous Knurr Formation and the Jurassic rocks as a result of less cementation. Regarding AvO signatures (figure 5.6b), a significant part of the Kolmule reflection has become unclassified (the intercept is near zero with a weak positive gradient). We see that there are classes IV in the oil and gas case; this is related to sandstones being softer than the encasing shale. For Kolmule sandstone, both class IIp is seen for the brine sand. Classes IIn become more dominant in the oil case, and classes I expected when the sands are gas-saturated. For Knurr, the variations are expected in the gas case towards the northwest where classes shift from

IIn (base scenario) to I.

For the mean of the uplift case (see figures 5.5c and 5.6c), there are two trends; a general increase in porosity and decrease in velocities towards the Loppa High area, and the contrary case eastwards from the Loppa High. The more significant variations are evident towards the Loppa High, where the actual maximum uplift is expected; this translates that this area corresponds to the maximum difference in burial depth with the base case. The effect is more notorious in the Cretaceous strata were the compaction degree has been weakened, resulting in softer rocks. The Jurassic intervals are affected in a significant way, especially in the depression. The changes are related to higher temperatures than in the base case (being in this area more similar to the overestimated case). It is necessary to highlight that for the Cretaceous formations, the "paleo-topography" when maximum burial is different in comparison to the base, overestimated and underestimated cases; we see that in the other cases the Cretaceous horizons are deeper towards Loppa High, and they shallow towards Juksa. In this case, the greater depth is found in what is today the basin.

Regarding Avo signatures, although the changes in the Cretaceous sandstones, the changes in AvO classes are minor. Conversely, for the Jurassic formations, there are significant differences northwestwards. For brine-saturated sandstones, the classes shift from mainly IIp in the base scenario to IIn in this scenario. Due to lower degree of cementation, this sequence is more fluid sensitive, describing classes I for the gas case.

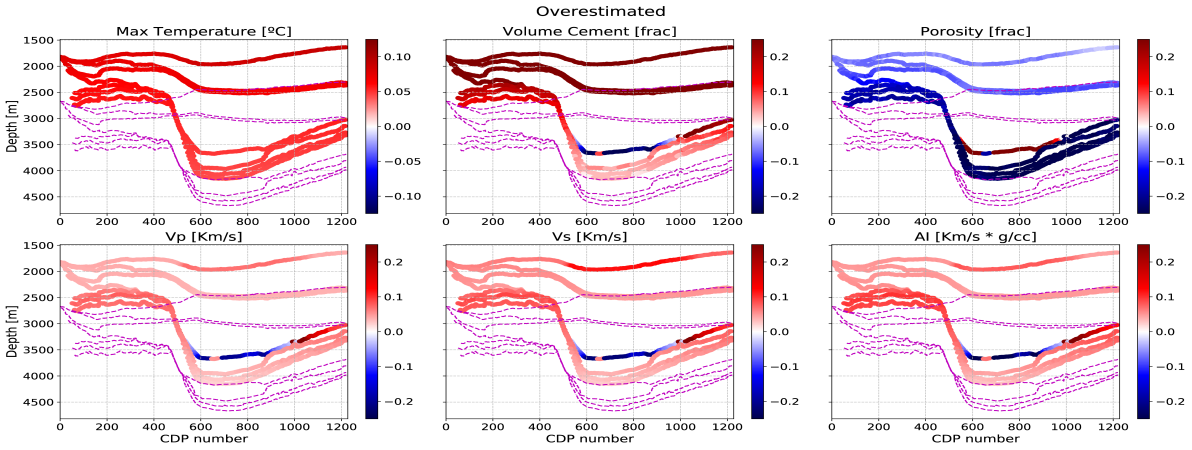

(a) Overestimated

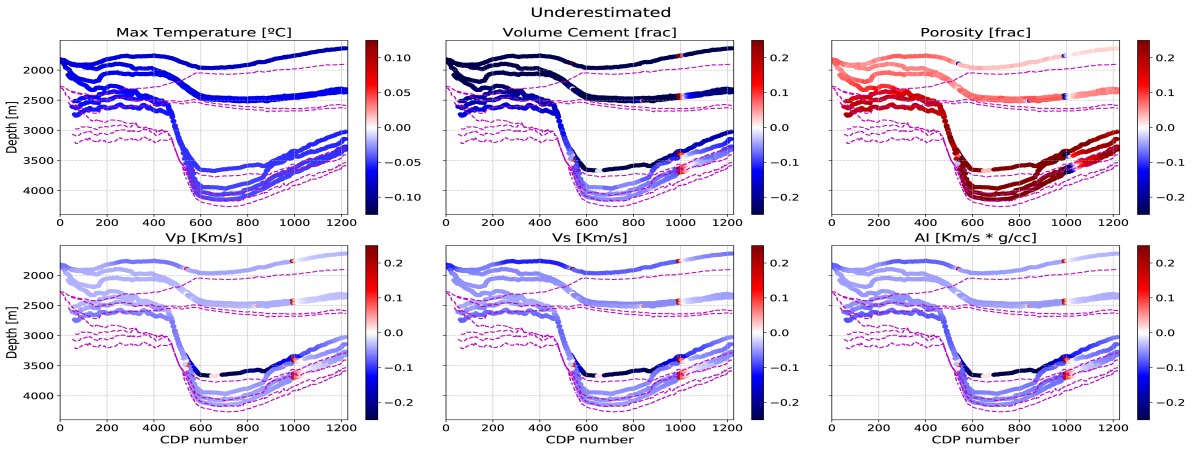

(b) Underestimated

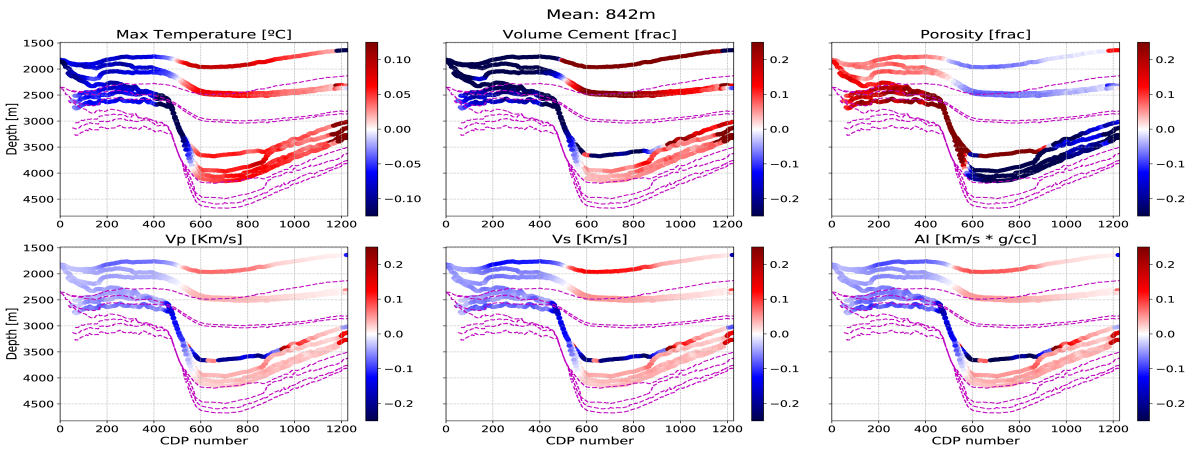

(c) Mean

Figure 5.5: Sandstone difference property sections for the three different alternative uplift cases. The warm colors represent increase in the magnitude of the property, while cold colors the decrease. The purple lines illustrates the maximum burial for each horizon at the different uplift scenario.

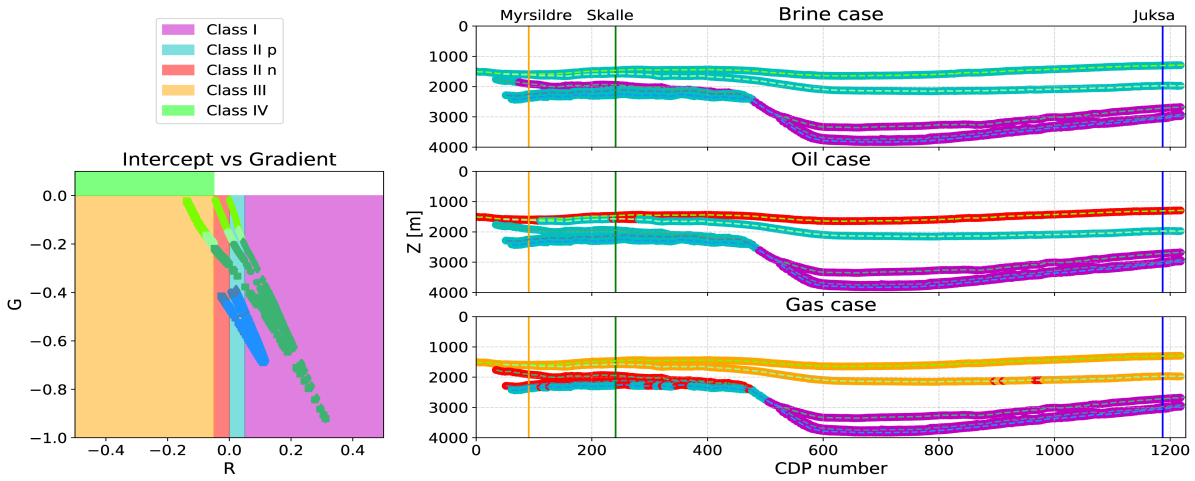

(a) Overestimated

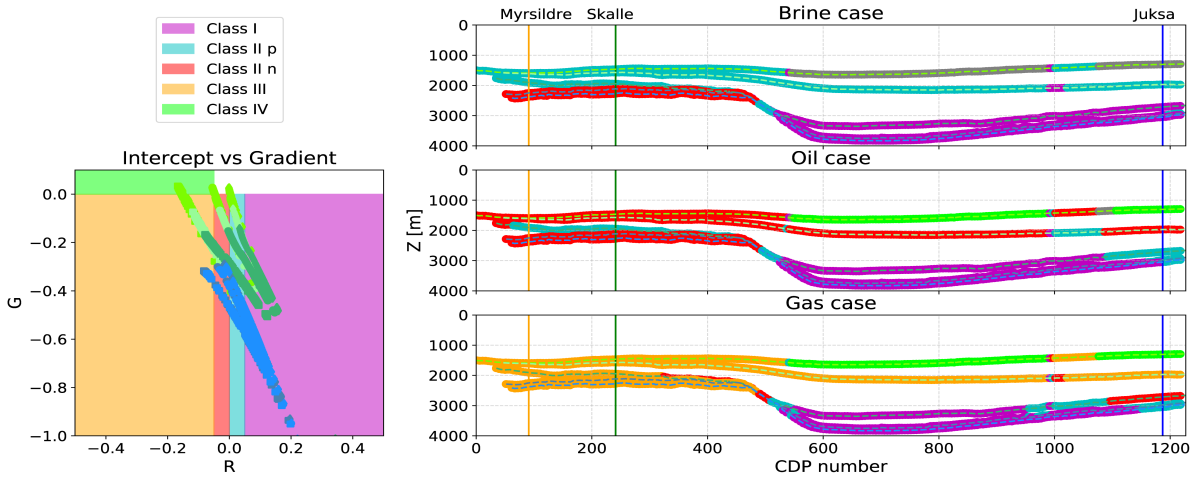

(b) Underestimated

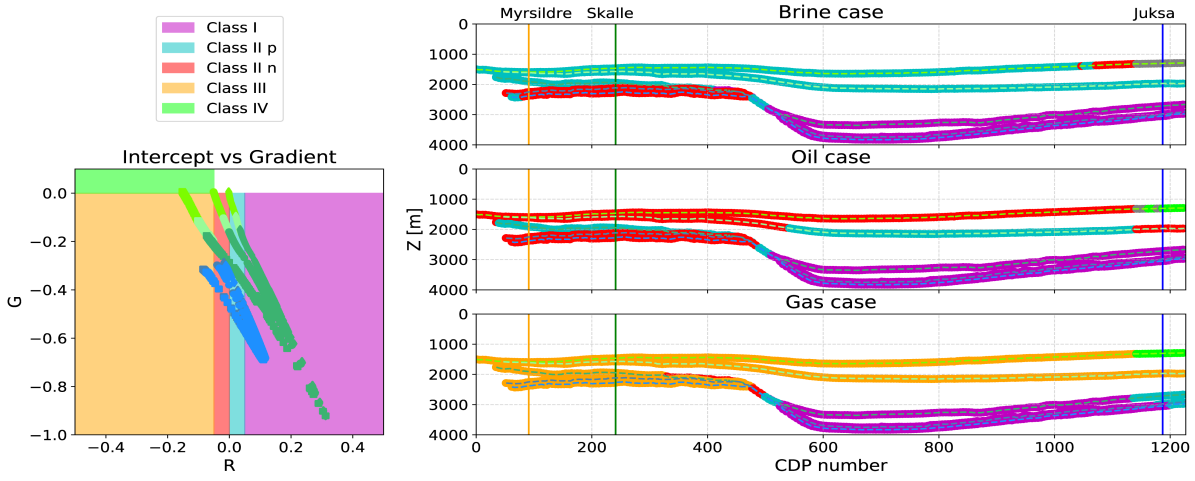

(c) Mean

Figure 5.6: AVO crossplots and sections for the different uplift scenarios apart from the base case. The colors in the intercept and gradient plot correspond to the formation color legend established in figure 3.12 .Additionally, the brine-, oil- and gas-bearing cases are represented by the diamond, circle and square markers respectively. To the right, the expected AVO classes for each fluid case.

Chapter 6

Discussion

6.1 Geological history considerations

As mentioned in chapter 4, the burial history curves were based on the work of Baig et al. (2016). These burial curves just include Cenozoic uplift and erosion and are calibrated for the Hammerfest Basin. However, evidence for Early Cretaceous uplift has been reviewed and studied by Indrevær et al. (2017).

Indrevær et al. (2017) suggest the tectonic model dates the onset for the Loppa High uplift to early Barremian times. The narrow terrace described by Iqbal (2016) is characterized as an anticline with axis parallel to the Asterias Fault complex, and it might be related to tectonic inversion (see figure 6.1). This change in the burial history will affect the rock-physics modelling in this work; the strength of this effect will depend on the magnitude of such uplift in comparison with the Cenozoic uplift. If the early Cretaceous uplift is more critical than later events, the Jurassic formations could have experimented cracking due to unloading of the overburden and subsequent burial accompanied by cementation resulting in the need for more complex and robust modelling. Nonetheless, Henriksen et al. (2011a) argue that although multiple phases of uplift have occurred in the Barents Sea, their contribution to the net erosion can be minimal, and exemplifies the Late Jurassic-Early Cretaceous events.

Furthermore, Johansen et al. (2016) estimated uplift by using the Lower Kolmule formation as a reference; such estimations can deviate if the Hekkingen and Fuglen shales are included in the analysis. Although such uplift estimations are consistent in a regional overview, including these shales could add local variability due that, in the case of an earlier uplift episode, their properties would record evidence of such event that has been neglected and does not affect the Cretaceous strata. Additionally, as mentioned in section 5.2, the Upper Cretaceous horizons form a depocenter at maximum burial. This can be the product of artefacts from the uplift estimations from Johansen et al. (2016) leading to a non existing depocenter in the narrow shelf. In figure 5.5, we can appreciate the difference in the paleo-topography at maximum burial for the three uplift estimations cases. An overestimation or underestimation of 200 meters to the uplift profile from Johansen et al. (2016) still result in a depocenter at this level. Nevertheless, when using a constant uplift the depocenter is not in the narrow shelf. A combination of uplift overestimation towards the Loppa High, and underestimation from the basin to Juksa could explain the depocenter as an artefact. Another alternative is that in fact there is a structural low in

the narrow shelf at maximum burial during the Upper Cretaceous times, however, this is outside of the scope of this work and there is not enough information to support it. This should be further investigated, as it can have tectonostratigraphic implications, as well it raises attention to pitfalls when using uplift estimates in rock-physics methodologies.

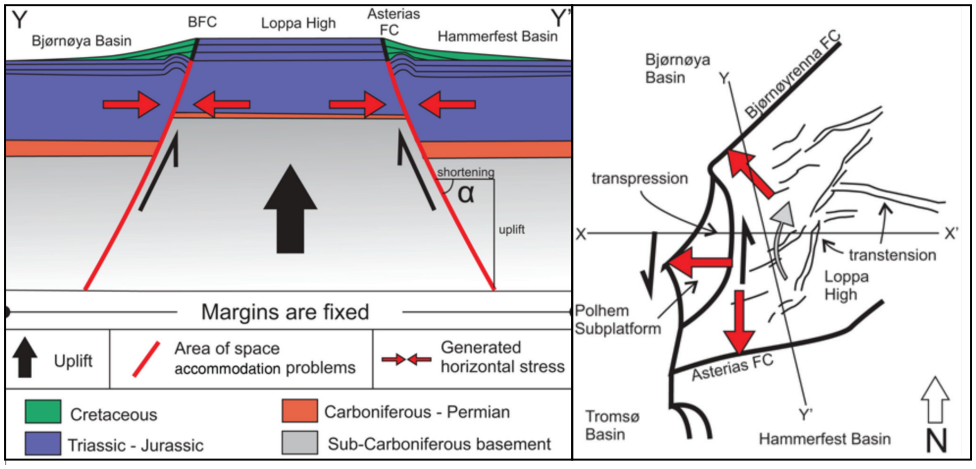

Figure 6.1: Tectonic model for the Loppa High in the Early Cretaceous and the location of the transect and the horizontal stresses resulting from the uplift. Taken from Indrevær et al. (2017).

6.2 Rock-physics considerations

6.2.1 Shale rock-physics models

As stated in the previous chapters, the shale properties in this work have been estimated from linear regressions of well measurements. Although, there are published shale properties-depth relationships, as Mondol et al. (2007, 2008), they are restricted to mechanical compaction, and neglect the effects that more advanced diagenesis have on them; this will result overestimations of porosity and underestimation of the velocities (see figure 4.8). Figure 6.2 compares the well measurements with the estimated shale properties from the regressions (black line, red and purple squares), the models described by Vernik and Kachanov (2010) and Avseth et al. (2005), and the least square regressions of the laboratory tests performed by Mondol et al. (2008). We see that the estimated velocities agree with the models at a given porosity; this is especially the case when comparing it with Vernik's model, where the agreement is consistent in all the porosity range. In the case of the constant-clay model, the estimations do not agree for the moderate-high porosity ranges ($\phi > 0.2$). The laboratory measurements of Mondol et al. (2008), do not agree with the data; this is related to restriction to mechanical compaction, as mentionated above.

Section 4.8 shows that there are differences in the different estimations for shale properties depending on the shale trend scenario. We see that scenario 4 estimates softer shales than the other scenarios. This difference can be the result of mineralogical variations of the shales in the wells used for each of the scenarios, relating it to provenance and diagenetic processes. For the compaction domain, Mondol et al. (2007) stated that the porosity and velocity stress-dependence is different for different clay aggregates; shales with a higher proportion of kaolinite are more compressible than if smectite is the main clay mineral, and chlorite and illite are found in between these. When temperatures are above 70 °C illitization, the transition smectite-illite takes place,

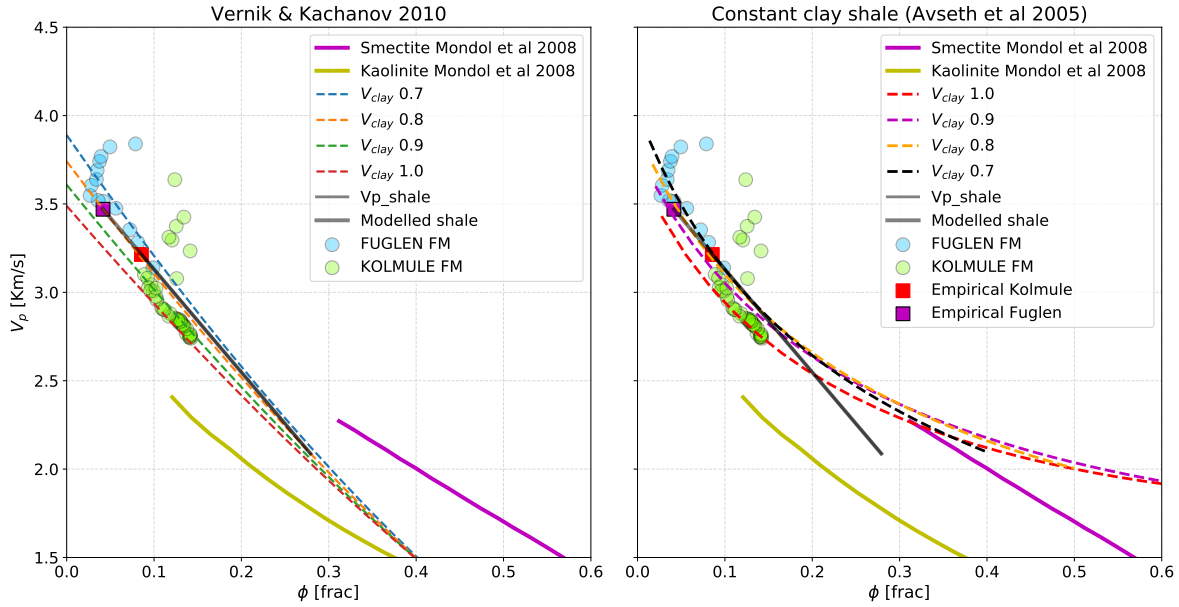

Figure 6.2: Comparison between the modelled shales using the empirical relationships used for estimating the shale properties (Scenario 4 as mentioned in section 5.1) with the models from Avseth et al. (2005), Mondol et al. (2008) and Vernik and Kachanov (2010).

and shales with the content of smectite are prone to cement. Quartz and water are a by-product of this reaction, where the former could lead to further stiffening by cementing the shales (Thyberg et al., 2009). However, the water that is generated in the reaction can cause overpressure and locally cause softening of the shales.Johansen et al. (2016) proposed a modified trend based on a combination of diagenetic and rock-physics modelling that accounts for illitization. Additionally to this effect, Dvorkin and Gutierrez (2001) model predicts that siltier shales will have higher velocities than pure shales (see figure 6.4; this could mean that the Cretaceous shales are more siltier than their Jurassic counterpart.

6.2.2 About the sandstone rock-physics models

The assumptions in the rock physics modelling described in section 4.4 are simplifications that potentially can lead to substantial differences between the models and the data. The temperature gradient, in reality, varies with time and spatially. These factors are not accounted for in the models, which can affect the results significantly, as demonstrated by (Dræge et al., 2014). Moreover, the rock parameters that are included in the diagenetic model can affect in different degree the results of the modelling. Some of such factors are, as described in sections 2.2.1 and 2.2.2, critical porosity, grain size, clay coating and quartz fraction which can be calibrated locally with different information sources (XRD, thin sections or core descriptions). Variations of these parameters are expected at different well locations due to lateral variations in facies as result of different depositional environments, sediment sources and others factor are anticipated.

Figure 6.3 presents a sensitivity analysis for the parameters related to the diagenetic models. It presents the impact that the variability of such parameters has on the sandstone properties

modelling. This analysis was done at Skalle CDP location for the Lower Kolmule (Kolmule sandstone) and Stø Formations levels. These parameters are related to the rock (IGV volume and Walderhaugh's parameters for sandstones) and the burial history (Temperature and timing of Maximum burial).

Firstly, we discuss the effect of variations in the rock parameters has on the model. We see that the critical porosity increase results in a higher porosity when starting the onset of quartz cementation and in a final higher porosity. The sensitivity to this parameter is higher in the first moments on cementation and becomes insensitive when more intense cementation has occurred. The initial matrix fraction ($m0$) is a representation of maturity and diagenesis of the sandstone, and we see that when it increases it affects primarily the starting porosity (it relates directly with the initial or critical porosity by filling the available pore space), the porosity at the onset of quartz cementation and the final porosity by reducing them. We have assumed that no cement was present before quartz cementation, such cement would increase the $m0$ resulting in a reduced span of compaction, and in some extent retard the rate of quartz cementation due to a smaller surface area (Lander and Walderhaug, 1999). The effect of clay coating is not a critical factor in these models. As we see, the inhibition effect of 10% coating compared to not coating at all is rather small. Conversely, when we go from fine-grained sandstones (0.01 cm) to a coarser grain (0.1 cm), we can expect high variations on the porosity reduction and velocity. The reason behind it is that the fine-grained sandstones have a high surface area available for quartz cementation, and they showed a more rapid cementation rate (Walderhaug, 1996).

Secondly, we have also included the parameters related to the basin evolution, temperature gradient and timing for the maximum burial. We see that the temperature gradient has a significant effect on both porosity and velocity, especially for the Stø Formation, which is buried deeper. The temperature gradient was assumed to be constant temporally and spatially; this could be improved by more robust basin analysis that includes more inputs from basin modellers as heat flow modelling. However, this is beyond the scope of this study. Regarding timing, this still is a matter of discussion, as Baig et al. (2016) pointed out. We found that the model is not sensitive to this as it is to grain size or the temperature gradient. However, the maximum difference explored here corresponds to $10MYears$, corresponding to a maximum burial at $42MYears$.

With regards to the stress regime, the wells observations show that there are not abnormal pore pressures; thus, the assumption of hydrostatic pressure holds when modelling mechanical compaction. However, certain clay mineralogy is associated with abnormal pore pressure resulting in porosity preservation and lower velocities (Storvoll et al., 2005; Mondol et al., 2007; Bjørlykke and Jahren, 2010).

The stress dependence is not accounted in the modelling after cementation starts which is a limitation of the Dvorkin-Nur model. However, (Avseth et al., 2016) introduced the *"patchy cement model"* which accounts for stress sensitivity for cemented sandstones. The model combines a nested Hashin-Strikman approach with contact theory. This nested approach consists of modelling an effective medium that comprises a binary mixture of cemented sandstones with loose unconsolidated sands. The cemented sandstone is modelled using Dvorikin-Nur model (Contact cement model) and the loose sands using Hertz-Mindlin contact theory. The moduli of the mixtures are then calculated by using equations 2.9 and 2.10.

Furthermore, we have neglected the effect of grain cracking as a result of unloading during

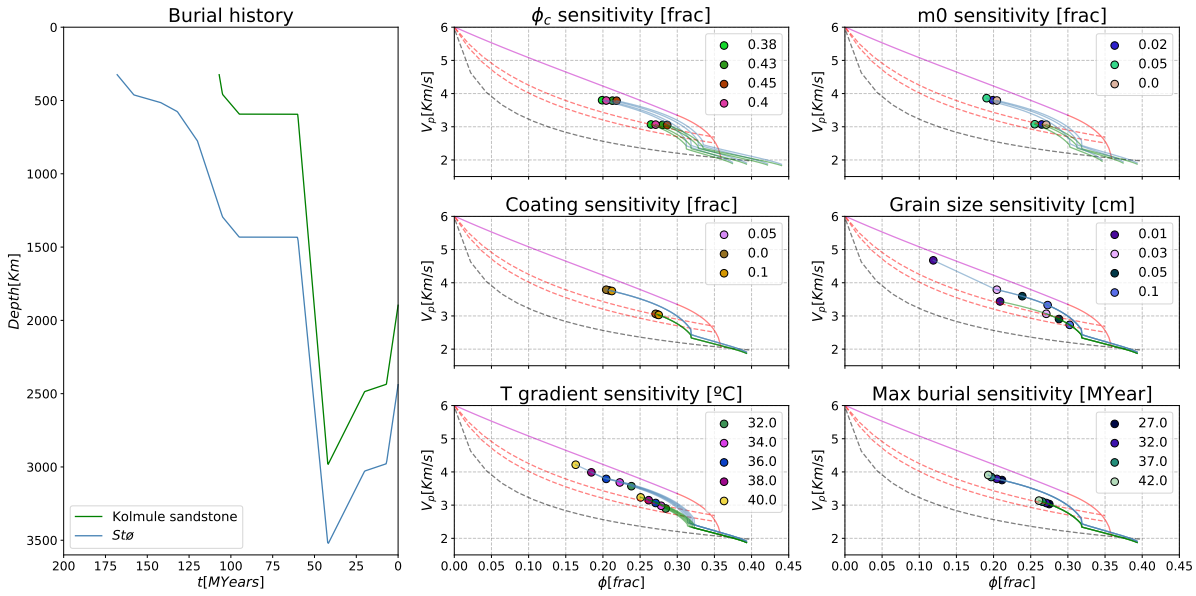

Figure 6.3: Sensitivity analysis for some of the input parameters for the burial history-constrained rock-physics modelling. The sensitivity analysis is done for the Kolmule sandstone and Stø formation at Skalle well position

uplift. The model used (modified HS upper bound) in this methodology neglects the stress dependence during uplift. Different authors have proposed models that incorporate the stress-dependence in this domain. (Bredesen et al., 2018) proposed to use a modification of the (Avseth et al., 2014) *"Kite model"* which includes a differential elastic medium. This method uses crack-like pore geometries for these inclusion models and obtained better shear moduli and velocity predictions. However, as pointed out by (Torset et al., 2020), the P-wave anisotropy sign change during unloading leading to the need to include anisotropic stress and strain fields in the rock physics modelling when dealing with uplift. Such a model can be accomplished by including an effective anisotropic medium, in this case, an implementation by (Fjaer, 2006).

As mentioned in chapter 4, the modelled sandstones correspond to well sorted and clean sandstones. Disagreements between the well log data and models are expected and strongly related to this (see figure 6.4). For the Cretaceous sandstones, these differences are higher. The well observations show that the models overestimate the porosity and underestimate the velocity. Additionally, the models underestimated the Vp/Vs ratio and acoustic impedance. We see that if we combined the model endpoint with a constant cement line, the properties are well-explained. Thus, these differences are linked to sorting in some degree.

Additionally, the shaly sand model is over imposed, illustrating that these differences can also be related to pore-filling clay particles in the sandstones. In reality, both sorting and pore-filling clay interplay to produce the observed properties. This methodology can be extended to sandstones with degraded sorting by incorporating a constant cement or shaly cement model at the endpoint of the well-sorted end member. To do so, we can use the available information from cores or thin sections and sedimentological conceptual models for a given prospect that is desired to analyze.

On the contrary, the Jurassic sandstones present a good match with the models, which can relate to the mineralogy of these sandstones. For these cases, the variations due to sorting are lower, and the main controlling factor for porosity reduction and velocity increase is diagenetic processes.

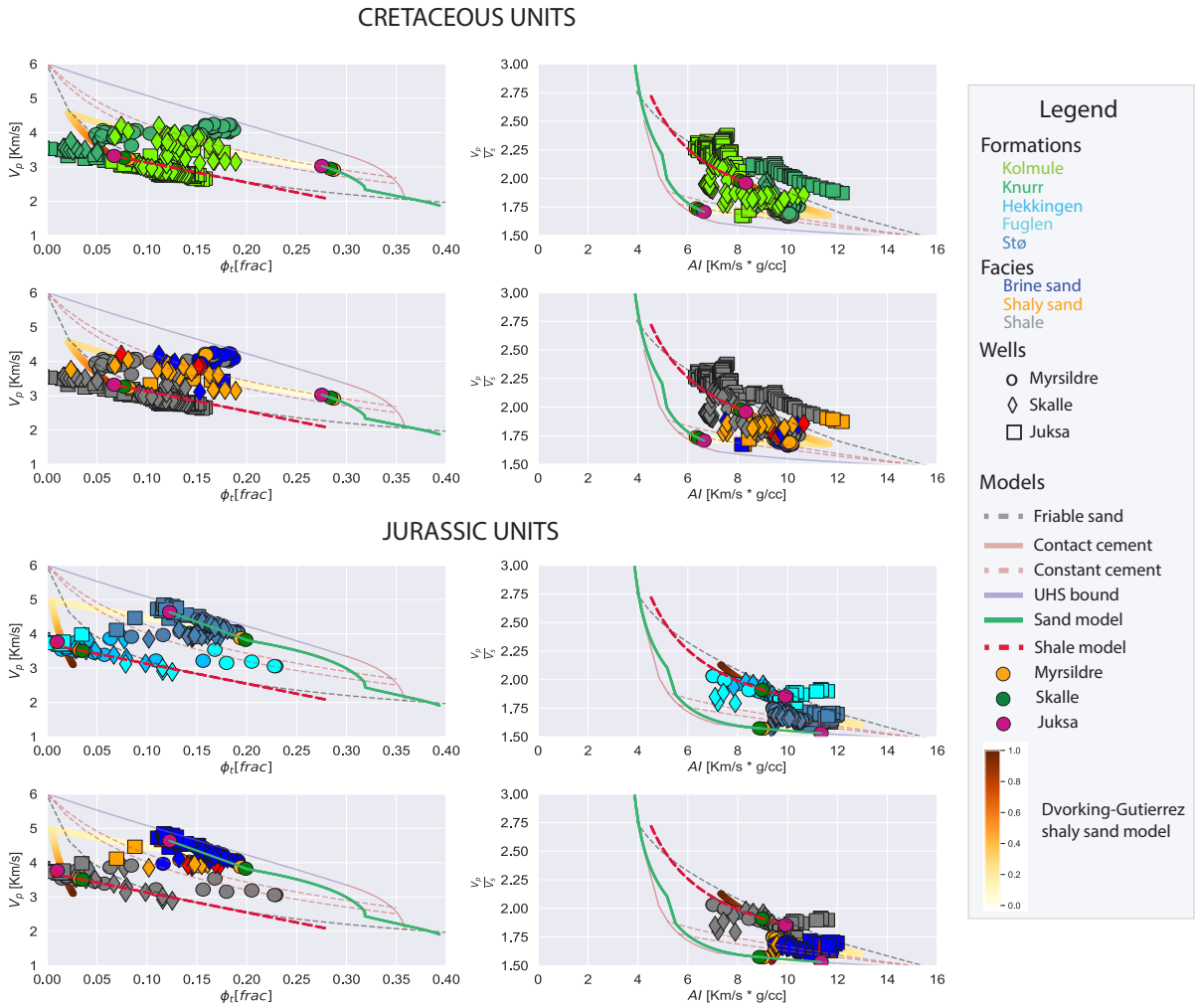

Figure 6.4: Comparison of the rock-physics models and the models result of the joint diagenetical-rockphysics modelling. Overimposed is the Dvorking-Gutierrez model for shaly sands.

6.3 Considerations regarding uplift estimations

As described in the chapter above, the uplift magnitude can have significant effects on rock properties; thus, the AvO signatures. Understating the effects due to variations in uplift estimates are, therefore, an essential factor to have into account when understanding the AvO signatures of a given prospect. For that reason, we consider that the models that intent to explain or predict these signatures include these uncertainties. The significance of these uncertainties varies spatially in areas with complex geological history where tectonic events can change drastically in a relatively reduced space.

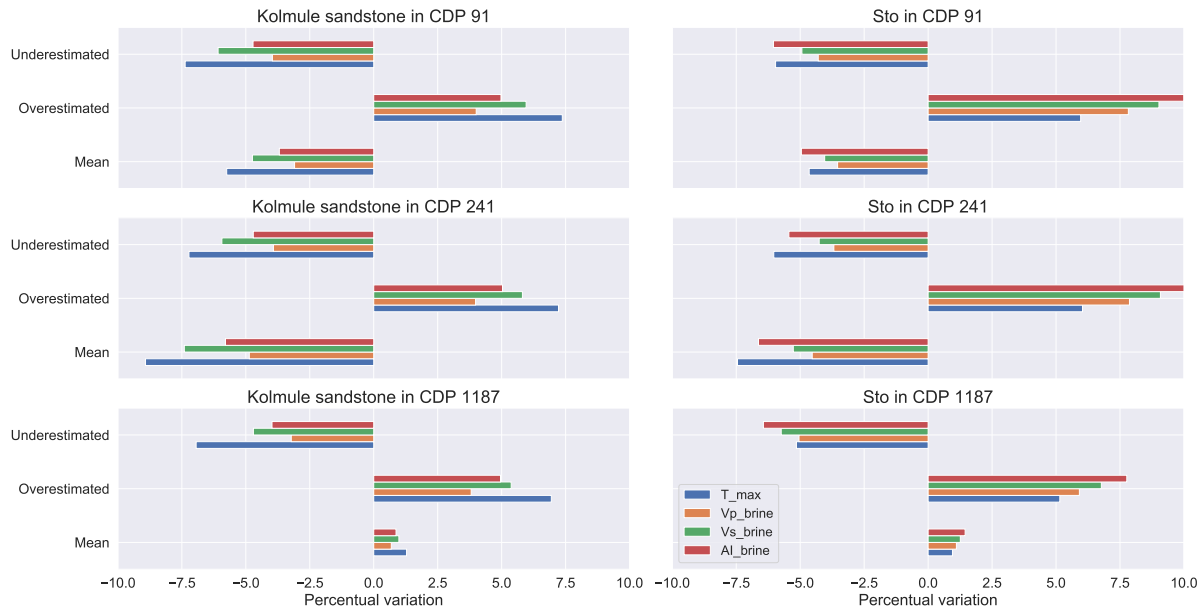

Figure 6.5: Tornado chart for the underestimated (-200 m), overestimated (+200 m) and mean (constant 842 m) uplift cases at the well locations for Kolmule Sandstone (Lower Kolmule) and Stø.

Figure 6.5 illustrates the expected changes in maximum temperature and the brine-bearing P-wave, S-wave velocity and acoustic impedance for the three cases. These differences are the result of comparing the expected values for each of the scenarios with the base case (provided uplift profile). The sensitivity analysis was carried out at the three well locations for the top of Kolmule sandstone (Lower Kolmule) and Stø. We see that in Myrsildre and Skalle, the property values decrease for both formations when the uplift is estimated to be 200 meters less or when it is constant. When the uplift is overestimated 200 meters, the velocities and impedance increase in a higher degree in Stø than in Kolmule; this is the result of very high-intensity porosity reduction resulting in a more rapid increase in velocity. In Kolmule, on the other hand, the porosity loss occurs at a lower degree; as a result, the velocities increase more gently.

Towards Juksa, the variations are similar for the underestimated case; for Kolmule the velocities and impedances are reduced in a smaller proportion than in Stø. The rocks at Lower Kolmule level are not cemented, in this case, leading them to become softer and with velocities highly depending on the effective stress; whereas, Stø sands are cemented at a lower degree, resulting in lower velocities and impedances. In contrast with Myrsildre and Skalle, the mean uplift case increased the properties for both formations; however, such increase is rather small due that the estimation in the base case at this position is very close to the mean of the whole profile. When the formations are buried 200 meters more (overestimated case), the rocks stiffen in both cases as the result of a higher degree of cementation. In figure 5.4 we see that from CDP 0-500 approximately, the mean case will underestimate the uplift significantly, resulting in lower velocities and acoustic impedance than in the base case. On the contrary, from CDP 500 to the final CDP position, the uplift is overestimated and becoming close to the base case towards Juksa. This will result in the mean case to overestimate the velocities and acoustic impedances with respect to the base case. The degree of the change in the properties depending on the transition between mechanical compaction and quartz cementation. The biggest changes are expected when in the analyzed case, the sandstone change of diagenetic domain (compaction

or cementation) with respect to the base case.

The former highlights the importance of using uplift estimates to constrain the interpretation and modelling of the rock physics properties; additionally, it brings to the attention of including its spatial variation. Figure 6.6 presents a summary of the AvO classes for the studied horizons for each case. It highlights the differences that the uplift estimations have on AvO classes and fluid sensitivity. We observe that Knurr Formation and the Jurassic formations are affected in a higher degree than the overlaying Cretaceous formations by the variations in the uplift magnitude. The fluid sensitivity to gas is more variable, resulting in more possibilities for AvO Classes.

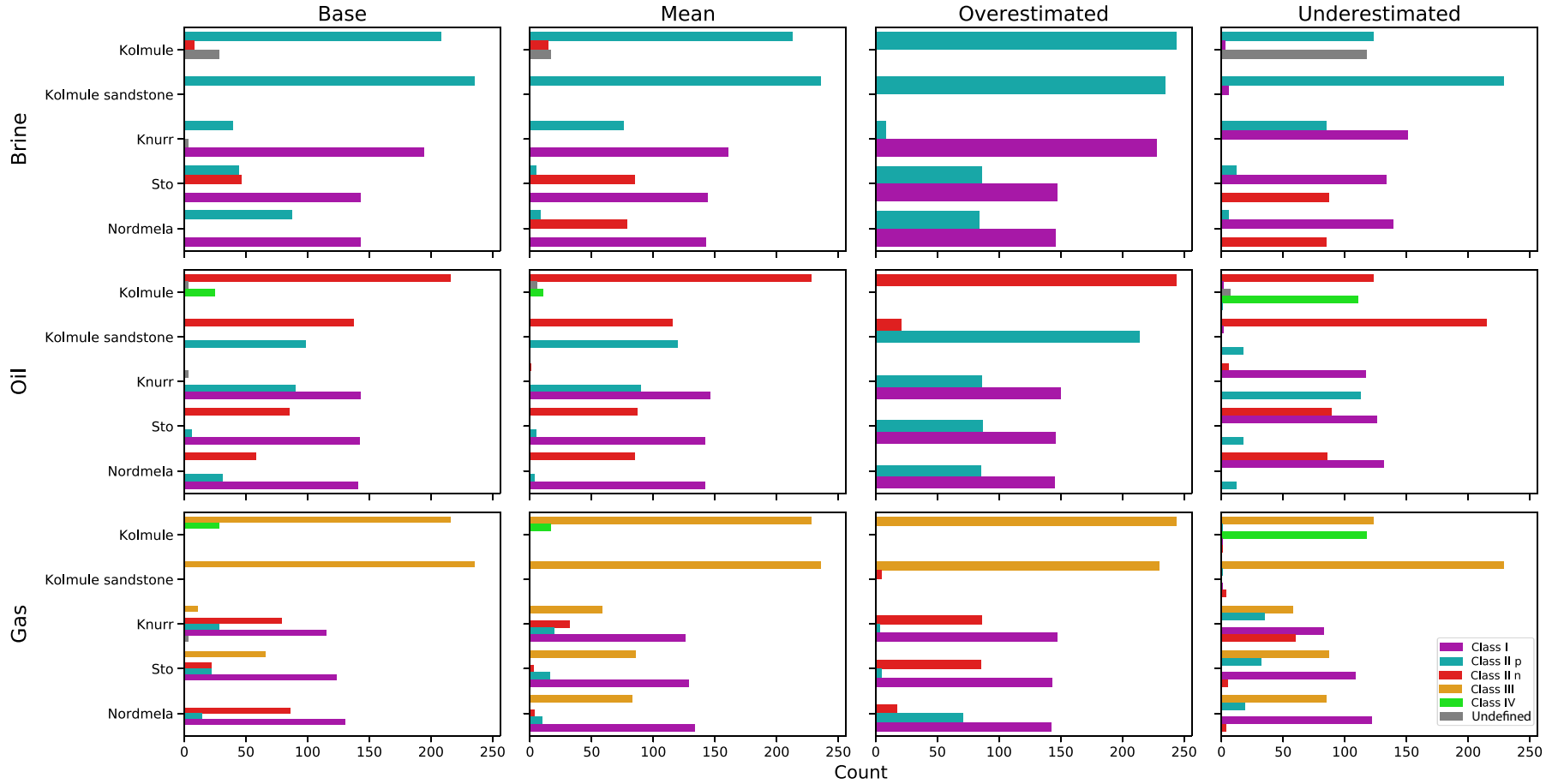

Figure 6.6: Bar plots with the AvO classes in each horizon. The plots are sorted by the uplift scenario and the fluid case. The horizontal axis corresponds to the counts for each class, whereas the vertical axis indicates the formation name.

6.4 Significance to previous works

Iqbal (2016) described and characterized the Lower Cretaceous clastic wedges presented in the Loppa area. The wedges were sorted in early-rifting stage and late-rifting stage wedges. The first category is characterized by a fall in the sea level drop that resulted in erosion in the narrow shelf, feeding with sediments the deeper basin (Iqbal, 2016). This process could also be more accentuated due to the tectonic inversion in this area (Indrevær et al., 2017). The second group consists of prograding wedges as a result of the flooding in the shelf as a response to changes in the sea level and sediment supply. The wells in this study penetrated some of these wedges (see chapter 3).

Within these wedges groups, there are identified different wedges types. In this study, we take a look at the wedges type 1 and 3 (early-rifting stage group), and wedges type 4 and 5 (late-rifting stage group). Below, we provide a summary for the interpretation of such wedges by Iqbal (2016):

1. **Type 1:** Myrsildre well (7120/1-2) penetrated this type of wedge; in this well, two different wedges corresponding to this kind are encountered one on top of the other. The upper wedge is interpreted to be slope aprons, gravity flows and ponded deposits source from the footwall. The lower wedge is interpreted as channel sands of an amalgamated fluvial system. This wedge corresponds to the Knurr Formation, and as stated in chapter 3, oil shows have been found in the lower wedge.

2. **Type 3:** This wedge type has not been penetrated. These wedges are deposited on the basin floor, displaying thickening from east to west. These wedges are interpreted as basin floor fans with associated prograding wedge. A network of channel incises on the basin floor fan feeding a submarine fan from the NE direction.

3. **Type 4:** Encountered in Myrsildre well, this wedge type is interpreted as the distal part of wave-dominated fan deltas with eroded topsets. The wedges consist of channels, levees, crevasse splays and strand plains. This wedge corresponds to the Kolmule Formation and it is mainly composed of fine-grained sediments.

4. **Type 5:** This type of wedge is suggested to be a basin floor fan that is sourced from the narrow shelf (northwest) by channels and gravity flows. However, bidirectional down lapping suggests that the fan is also source from the shelf by canyons. Although the wedge described by Iqbal (2016) have not been penetrated, the Lower Kolmule sandstones at Juksa might correspond to this type of wedge. We will refer to the wedge described by Iqbal (2016) as type 5a, and to the lower Kolmule sandstone at Juksa as type 5b.

Figure 6.9 shows the rock physics properties cross plots for each one of the wedges and incision in figure 6.7. The models correspond to the base and top of each formation at a CDP position for these facies. The overlaying well data presents a model to data comparison; however, as established before, the models represent the well-sorted sandstone end member. In this plot, we intend to illustrate the application and flexibility of this methodology, where we can test different burial history/uplift scenarios to test the influence they have on the rock physics properties spatially. Myrsildre penetrated wedges type 1 and 4,whereas Skalle penetrated the

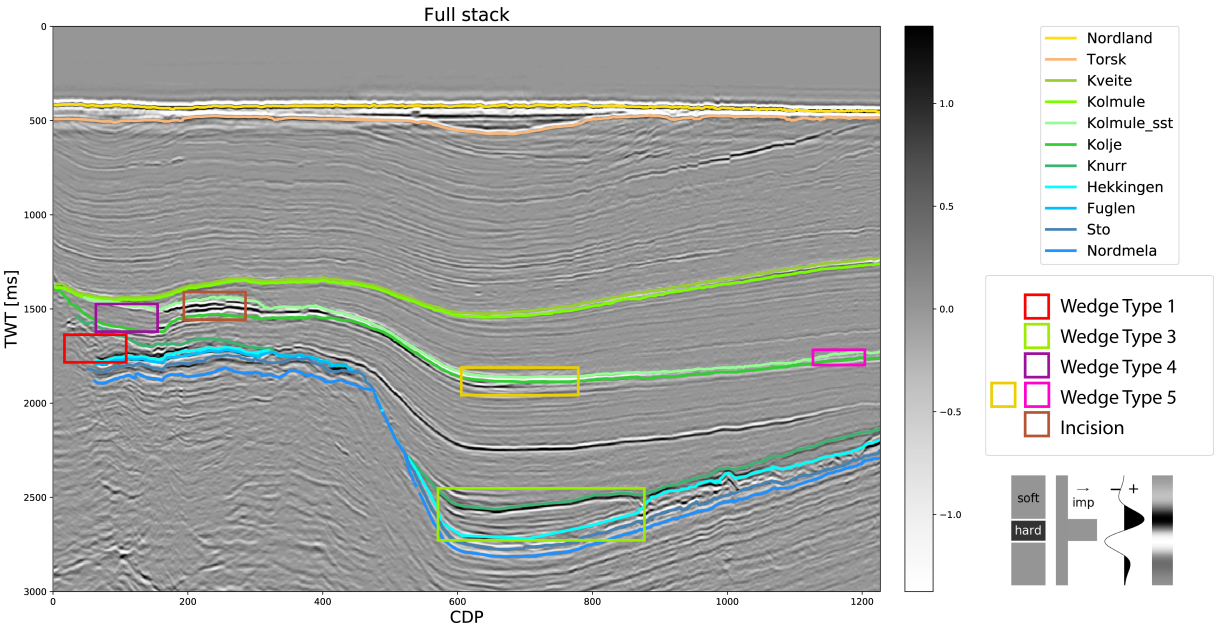

Figure 6.7: The different types of wedges on this seismic line according to Iqbal (2016).

incision and the distal part of the wedge type 4. This models generally overlap each other, suggesting similar diagenesis intensity for them. The base of wedge 1, which correspond to Hekkingen formation, does not overlap with these other models; this could be due to the higher depth difference from top to base, and that the modelling parameters are different for the Cretaceous and Jurassic. Wedge type 5 also overlap in most of the scenarios, with the exception when the uplift corresponds to the mean suggesting that if this wedge had similar sedimentological characteristics, the rock properties could be similar to the observations in the wells.

On the contrary, wedge type 3 is found on the basin floor and has been the one that most diagenesis have undergone. We see that in general, the expected properties for clean sand in this situation are highly compacted. Thus, sandstones at this level are expected to be stiff and fluid insensitive, resulting in higher risk prospects. It is important to note that the top of wedge type 3 has been affected by a numerical error in the Base case, resulting in anomalous cementation; this top is expected to be located somewhere between the top in the overestimated and underestimated counterparts.

We have extracted the AvO attributes (intercept and gradient) for each of these facies to compare them with the modelled shale/sandstone interface responses (figure 6.8). As mentioned above, oil accumulations have been found in the basal part of this wedge. The modelled AvO response predicts that the classes IIp and IIn could potentially be associated with this zone. However, the sensitivity to brine or oil is rather low. Wedge type 3 does not fall in the AvO data, which can be related to overestimations in the shear velocity of the sandstones (see section 6.2.2). Nevertheless, the fluid sensitivity for this wedge is expected to be very low, unless the porosity has been preserved by clay coating, overpressure or oil accumulations.

The wedge type 4 seem to be aligned to the background trend. We see some small deviations close to where the modelled data plot. Although the brine and oil models fall on the data, Myrsildre well did not encounter oil at this level, and this different response seen on the data

is probably related to shale/shaly or silty sands. Wedge 5a displays a broad background trend; however, in this wedge, the amplitude strength suggests coarse-grained facies (Iqbal, 2016). The modelled AvO suggests that accumulations could be present. On the other hand, the model predicts the presence of brine and oil for wedge 5b. At this level, residual oil accumulations were encountered in the well NPD.

The incision corresponds to the discovery in the Lower Kolmule Formation at Skalle. We see that in general, the model data agree and capture the outliers from the background trend. Further studies in the Extended Elastic Impedance space and the amplitude curves from the gathers could help to understand better these AvO responses. Additionally, we have assumed 100% change of fluid saturation in the fluid substitution; thus, a more robust and realistic fluid scenario should be accounted.

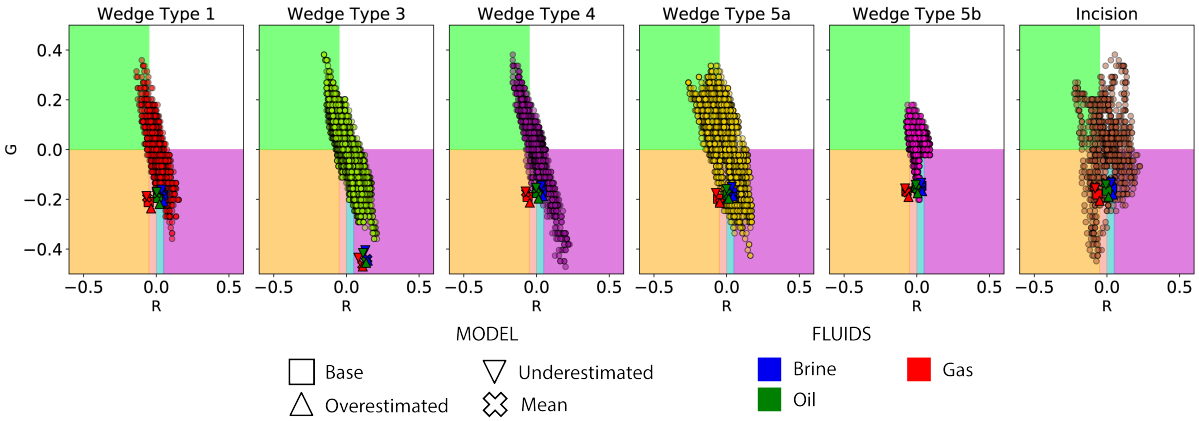

Figure 6.8: Intercept versus Gradient plot for each of the wedges defined by Iqbal (2016). The modelled AvO responses for the shale/sandstone interfaces correspond to all the uplift scenarios and the brine, oil and gas fluid cases.

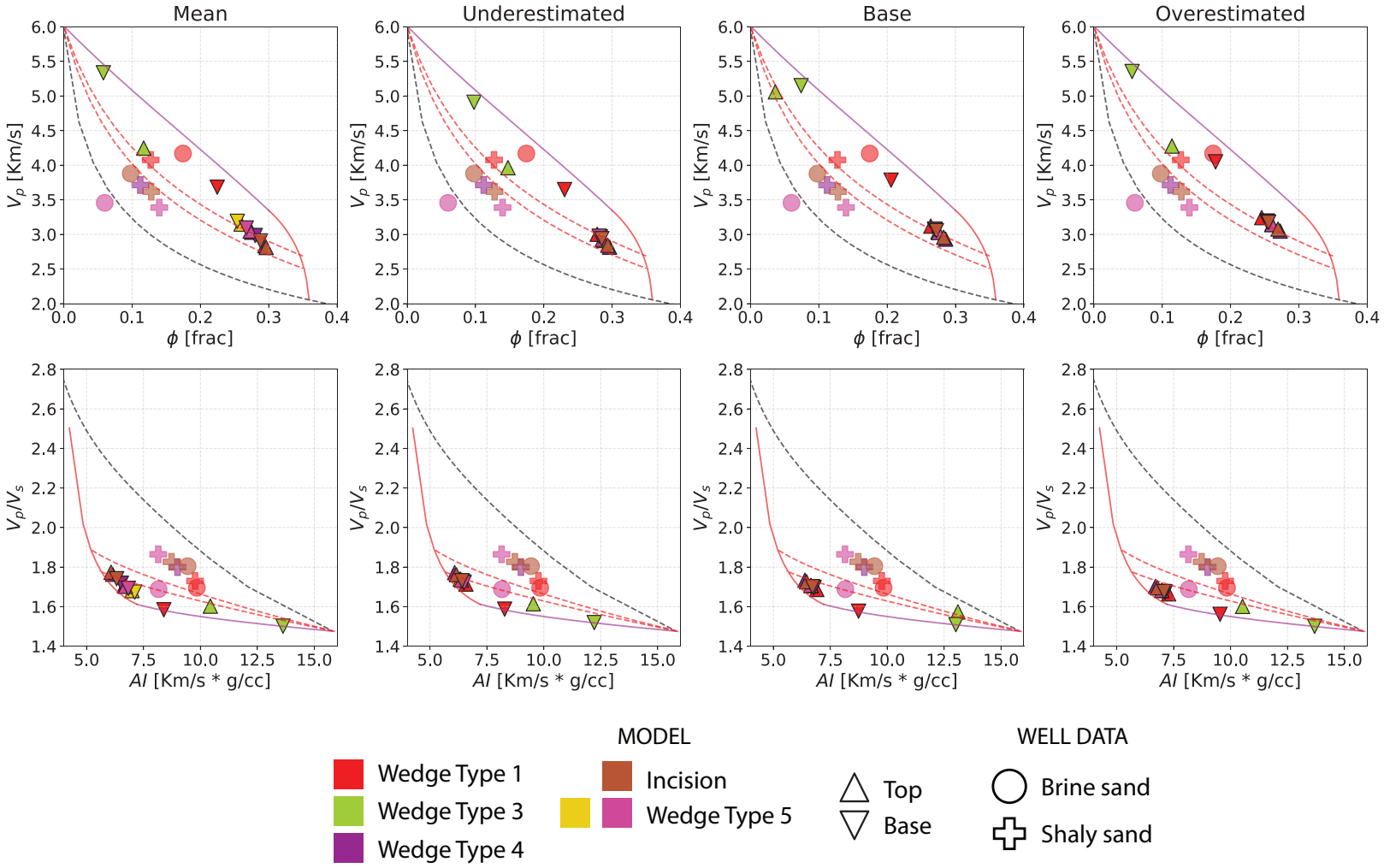

Figure 6.9: Sandstone models for each uplift scenario. The sandstones are modelled at the top (triangle facing up) and base (triangle facing down) for the CDP positions and horizons for each of the wedges (indicated by color) proposed by Iqbal (2016). The properties mean values (by facies) for the wedges penetrated by the wells is also shown to compare the models to the data. The rock-physics models are over-imposed to provide a guide for interpretation.

Chapter 7

Conclusion

The aim of this study was to demonstrated the value of integrating uplift estimations in rock-physics methodologies. The methodology has proven to provide a better understanding of the effect that the burial estimations have on the rock models, and how they potentially could influence decision-making.

This methodology allows for testing scenarios in a comprehensive way, where predictions and understanding of the rock properties and AvO signatures away from the well locations. We have been able to explore AvO responses that have not been tested more quantitatively. Although the models are subjects to the uncertainty that is inherent on their assumptions and physical limitations, they provide a starting point from which more rigorous analysis could start.

Additionally, with this methodology, we could potentially assist in explaining velocity analysis, by integrating knowledge on the basin evolution and stratigraphy; this could result in awareness during velocity model building for depth conversion or re-processing. In an inverse way, when using the methodology, it can provide elements for discussion about basin development and tectonostratigraphy, as it was discussed for the Upper Cretaceous paleo-topography.

The shale trend analysis by scenarios has demonstrated to be of great value since it allows to construct a ”band” for shale stiffness that can be tested in the rock-physics and AvO modelling. Furthermore, the shale trends were found to be consistent with the physical models, providing validity for their use.

Bibliography

Aki, K., Richards, P., 1981. Quantitative seismology: Theory and methods. Geological Journal 16, 90–90. URL: https://onlinelibrary.wiley.com/doi/abs/10.1002/gj.3350160110, doi:10.1002/gj.3350160110.

Avseth, P., Dræge, A., 2012. Memory of rocks - how burial history controls present day seismic properties. Example from Troll East, North Sea. pp. 2084–2088. URL: https://library.seg.org/doi/abs/10.1190/1.3627620, doi:10.1190/1.3627620, arXiv:https://library.seg.org/doi/pdf/10.1190/1.3627620.

Avseth, P., Dvorkin, J., Mavko, G., Rykkje, J., 2000. Rock physics diagnostic of north sea sands: Link between microstructure and seismic properties. Geophysical Research Letters 27, 2761–2764. URL: https://agupubs.onlinelibrary.wiley.com/doi/abs/10.1029/1999GL008468, doi:10.1029/1999GL008468.

Avseth, P., Johansen, T.A., Bakhorji, A., Mustafa, H.M., 2014. Rock-physics modeling guided by depositional and burial history in low-to-intermediate-porosity sandstones. GEOPHYSICS 79, D115–D121. URL: http://library.seg.org/doi/10.1190/geo2013-0226.1, doi:10.1190/geo2013-0226.1.

Avseth, P., Lehocki, I., 2016. Combining burial history and rock-physics modeling to constrain AVO analysis during exploration. The Leading Edge 35, 528–534. URL: http://library.seg.org/doi/10.1190/tle35060528.1, doi:10.1190/tle35060528.1.

Avseth, P., Mukerji, T., Mavko, G., 2005. Quantitative Seismic Interpretation: Applying Rock Physics Tools to Reduce Interpretation Risk. Cambridge University Press. doi:10.1017/CBO9780511600074.

Avseth, P., Mukerji, T., Mavko, G., Dvorkin, J., 2010. Rock-physics diagnostics of depositional texture, diagenetic alterations, and reservoir heterogeneity in high-porosity siliciclastic sediments and rocks — a review of selected models and suggested work flows. GEOPHYSICS 75, 75A31–75A47. URL: https://doi.org/10.1190/1.3483770, doi:10.1190/1.3483770, arXiv:https://doi.org/10.1190/1.3483770.

Avseth, P., Skjei, N., Mavko, G., 2016. Rock-physics modeling of stress sensitivity and 4d time shifts in patchy cemented sandstones — application to the visund field, north sea. The Leading Edge 35, 868–878. URL: https://doi.org/10.1190/tle35100868.1, doi:10.1190/tle35100868.1, arXiv:https://doi.org/10.1190/tle35100868.1.

Bachrach, R., Avseth, P., 2008. Rock physics modeling of unconsolidated sands: Accounting for nonuniform contacts and heterogeneous stress fields in the effective media approximation with applications to hydrocarbon exploration. Geophysics 73. doi:10.1190/1.2985821.

Baig, I., Faleide, J.I., Jahren, J., Mondol, N.H., 2016. Cenozoic exhumation on the southwestern Barents Shelf: Estimates and uncertainties constrained from compaction and thermal maturity analyses. Marine and Petroleum Geology 73, 105–130. URL: http://dx.doi.org/10.1016/j.marpetgeo.2016.02.024https://linkinghub.elsevier.com/retrieve/pii/S0264817216300472, doi:10.1016/j.marpetgeo.2016.02.024.

Bjørlykke, K., Jahren, J., 2010. Sandstones and Sandstone Reservoirs. Springer Berlin Heidelberg, Berlin, Heidelberg. pp. 113–140. URL: https://doi.org/10.1007/978-3-642-02332-3_4, doi:10.1007/978-3-642-02332-3_4.

Blazevic, L.A., Duffaut, K., Avseth, P., 2017. Burial induced changes in physical sandstone properties: A case study of North Sea and Norwegian Sea sandstone formations. pp. 3626–3631. doi:10.1190/segam2017-17726893.1.

Bredesen, K., Avseth, P., Johansen, T.A., Olstad, R., 2018. Rock physics modelling based on depositional and burial history of barents sea sandstones. Geophysical Prospecting 67, 825–842. URL: https://www.earthdoc.org/content/journals/10.1111/1365-2478.12683, doi:https://doi.org/10.1111/1365-2478.12683.

Burley, S.D., Kantorowicz, J.D., Waugh, B., 1985. Clastic diagenesis. Geological Society, London, Special Publications 18, 189–226. doi:10.1144/GSL.SP.1985.018.01.10.

Castagna, J.P., Swan, H.W., 1997. Principles of avo crossplotting. The Leading Edge 16, 337–344. URL: https://doi.org/10.1190/1.1437626, doi:10.1190/1.1437626, arXiv:https://doi.org/10.1190/1.1437626.

CGG, . Hampson-russell suit.

Djéran-Maigre, I., Tessier, D., Grunberger, D., Velde, B., Vasseur, G., 1998. Evolution of microstructures and of macroscopic properties of some clays during experimental compaction. Marine and Petroleum Geology 15, 109 – 128. URL: http://www.sciencedirect.com/science/article/pii/S0264817297000627, doi:https://doi.org/10.1016/S0264-8172(97)00062-7.

Doré, A.G., Corcoran, D.V., Scotchman, I.C., 2002. Prediction of the hydrocarbon system in exhumed basins, and application to the NW European margin. Geological Society Special Publication 196, 401–429. doi:10.1144/GSL.SP.2002.196.01.21.

Dræge, A., Duffaut, K., Wiik, T., Hokstad, K., 2014. Linking rock physics and basin history — filling gaps between wells in frontier basins. The Leading Edge 33, 240–246. URL: https://doi.org/10.1190/tle33030240.1, doi:10.1190/tle33030240.1, arXiv:https://doi.org/10.1190/tle33030240.1.

Dvorkin, J., Gutierrez, M.A., 2001. Textural sorting effect on elastic velocities, part II: Elasticity of a bimodal grain mixture. pp. 1764–1767. URL: https://

library.seg.org/doi/abs/10.1190/1.1816466, doi:10.1190/1.1816466, arXiv:https://library.seg.org/doi/pdf/10.1190/1.1816466.

Dvorkin, J., Nur, A., 1996. Elasticity of high-porosity sandstones: Theory for two North Sea data sets 61, 1363–1370.

Dvorkin, J., Prasad, M., Sakai, A., Lavoie, D., 1999. Elasticity of marine sediments: Rock physics modeling. Geophysical Research Letters 26, 1781–1784. doi:10.1029/1999GL900332.

Faleide, J.I., Bjørlykke, K., Gabrielsen, R.H., 2010. Geology of the Norwegian Continental Shelf. Springer Berlin Heidelberg, Berlin, Heidelberg. pp. 467–499. URL: https://doi.org/10.1007/978-3-642-02332-3_22, doi:10.1007/978-3-642-02332-3_22.

Faleide, J.I., Vågnes, E., Gudlaugsson, S.T., 1993. Late mesozoic–cenozoic evolution of the southwestern barents sea. Geological Society, London, Petroleum Geology Conference series 4, 933–950. URL: https://pgc.lyellcollection.org/content/4/1/933, doi:10.1144/0040933, arXiv:https://pgc.lyellcollection.org/content/4/1/933.full.pdf.

Fawad, M., Mondol, N.H., Jahren, J., Bjørlykke, K., 2011. Mechanical compaction and ultrasonic velocity of sands with different texture and mineralogical composition , 697–720doi:10.1111/j.1365-2478.2011.00951.x.

Fjaer, E., 2006. Modeling the stress dependence of elastic wave velocities in soft rocks.

Florez-Nino, J.M., 2005. Integrating geology, rock physics, and seismology for reservoir-quality prediction. Ph.D. thesis. Stanford University.

Gabrielsen, R.H., Faerseth, R.B., Jensen, L.N., Kalheim, J.E., Riis, F., 1990. Structural Elements of the Norwegian Continental Shelf Part I: The Barents Sea Region.

Gassmann, F., 1951. Uber die elastizitat poroser medien. Vierteljahrsschrift der Naturforschenden Gesellschaft in Zurich 96, 1–23. URL: https://ci.nii.ac.jp/naid/10017426854/en/.

Giles, M.R., Indrelid, S.L., James, D.M.D., 1998. Compaction — the great unknown in basin modelling. Geological Society, London, Special Publications 141, 15–43. URL: https://sp.lyellcollection.org/content/141/1/15, doi:10.1144/GSL.SP.1998.141.01.02, arXiv:https://sp.lyellcollection.org/content/141/1/15.full.pdf.

Hashin, Z., Shtrikman, S., 1963. A variational approach to the theory of the elastic behaviour of multiphase materials. Journal of the Mechanics and Physics of Solids 11, 127 – 140. URL: http://www.sciencedirect.com/science/article/pii/0022509663900607, doi:https://doi.org/10.1016/0022-5096(63)90060-7.

Helset, H.M., Mattehws, J.C., Avseth, P., van Wijngaarden, A.J., 2004. Combined Diagenetic and Rock Physics Modeling for Improved Control on Seismic Depth Trends, in: 66th Conference & Exhibition, EAGE. pp. 7–10.

Henriksen, E., Bjørnseth, H.M., Hals, T.K., Heide, T., Kiryukhina, T., Kløvjan, O.S., Larssen, G.B., Ryseth, A.E., Rønning, K., Sollid, K., Stoupakova, A., 2011a. Chapter 17 Uplift and erosion of the greater Barents Sea: impact on prospectivity and petroleum systems. Geological Society, London, Memoirs 35, 271–281. URL: http://mem.lyellcollection.org/lookup/doi/10.1144/M35.17, doi:10.1144/M35.17.

Henriksen, E., Ryseth, A.E., Larssen, G.B., Heide, T., Rønning, K., Sollid, K., Stoupakova, A.V., 2011b. Chapter 10 tectonostratigraphy of the greater barents sea: implications for petroleum systems. Geological Society, London, Memoirs 35, 163–195. URL: https://mem.lyellcollection.org/content/35/1/163, doi:10.1144/M35.10.

Indrevær, K., Gabrielsen, R.H., Faleide, J.I., 2017. Early Cretaceous synrift uplift and tectonic inversion in the Loppa High area, southwestern Barents Sea, Norwegian shelf. Journal of the Geological Society 174, 242–254. URL: http://jgs.lyellcollection.org/lookup/doi/10.1144/jgs2016-066, doi:10.1144/jgs2016-066.

Iqbal, J., 2016. Reservoir characterization of the Lower Cretaceous clastic wedges in the southwestern Barents Sea using seismic analysis and rock physics diagnostic. Ph.D. thesis. University of Stavanger.

Japsen, P., 2000. Investigation of multi-phase erosion using reconstructed shale trends based on sonic data. sole pit axis, north sea. Global and Planetary Change 24, 189 – 210. URL: http://www.sciencedirect.com/science/article/pii/S0921818100000084, doi:https://doi.org/10.1016/S0921-8181(00)00008-4.

Johansen, N., Avseth, P., Duffaut, K., Britt, M., 2016. Burial history and implications for seismic AVO signatures in the Western Barents Sea.

Lander, R.H., Walderhaug, O., 1999. Predicting Porosity through Simulating Sandstone Compaction and Quartz Cementation. AAPG Bulletin 83 (1999), 433–449. URL: http://search.datapages.com/data/doi/10.1306/00AA9BC4-1730-11D7-8645000102C1865D, doi:10.1306/00AA9BC4-1730-11D7-8645000102C1865D.

Lehocki, I., 2010.

Marion, D., Nur, A., Yin, H., Han, D., 1992. Compressional velocity and porosity in sand-clay mixtures. GEOPHYSICS 57, 554–563. URL: https://doi.org/10.1190/1.1443269, doi:10.1190/1.1443269, arXiv:https://doi.org/10.1190/1.1443269.

Mavko, G., Mukerji, T., Dvorkin, J., 2020. The rock physics handbook. 3rd ed., Cambridge University Press.

Mindlin, R., 1949. Compliance of elastic bodies in contact. Journal of Applied Mechanicss 16, 259–268.

Mondol, N.H., Bjørlykke, K., Jahren, J., Høeg, K., 2007. Experimental mechanical compaction of clay mineral aggregates—Changes in physical properties of mudstones during burial. Marine and Petroleum Geology 24, 289–311. URL: https://linkinghub.elsevier.

com/retrieve/pii/S026481720700027X, doi:10.1016/j.marpetgeo.2007.03.006.

Mondol, N.H., Jahren, J., Bjørlykke, K., Brevik, I., 2008. Elastic properties of clay minerals. The Leading Edge 27, 758–770. URL: https://doi.org/10.1190/1.2944161, doi:10.1190/1.2944161, arXiv:https://doi.org/10.1190/1.2944161.

Nooraiepour, M., Mondol, N.H., Hellevang, H., Bjørlykke, K., 2017. Experimental mechanical compaction of reconstituted shale and mudstone aggregates: Investigation of petrophysical and acoustic properties of SW Barents Sea cap rock sequences. Marine and Petroleum Geology 80, 265–292. URL: http://dx.doi.org/10.1016/j.marpetgeo.2016.12.003https://linkinghub.elsevier.com/retrieve/pii/S0264817216304329, doi:10.1016/j.marpetgeo.2016.12.003.

NPD, . Norwegian Petroleum Dictatoriate FactPages. http://factpages.npd.no/factpages/. Accessed: 2020-06-07.

Ohm, S.E., Karlsen, D.A., Austin, T.J.F., 2008. Geochemically driven exploration models in uplifted areas: Examples from the Norwegian Barents Sea. AAPG Bulletin 92, 1191–1223. URL: http://search.datapages.com/data/doi/10.1306/06180808028, doi:10.1306/06180808028.

Ostrander, W.J., 1984. Plane-wave reflection coefficients for gas sands at nonnormal angles of incidence. GEOPHYSICS 49, 1637–1648. URL: https://doi.org/10.1190/1.1441571, doi:10.1190/1.1441571, arXiv:https://doi.org/10.1190/1.1441571.

Rodriguez, I., 2015. Petrophysical characterization of the Lower Cretaceous clastic wedges in the northwestern Barents Sea. Ph.D. thesis. University of Stavanger.

Ross, C.P., Kinman, D.L., 1995. Nonbright-spot avo: Two examples. GEOPHYSICS 60, 1398–1408. URL: https://doi.org/10.1190/1.1443875, doi:10.1190/1.1443875, arXiv:https://doi.org/10.1190/1.1443875.

Shell, A.N., 1989. Final well report 7120/1-2.

Shuey, R.T., 1985. A simplification of the zoeppritz equations. GEOPHYSICS 50, 609–614. URL: https://doi.org/10.1190/1.1441936, doi:10.1190/1.1441936, arXiv:https://doi.org/10.1190/1.1441936.

Simm, R., Bacon, M., 2014. Seismic Amplitude: An Interpreter's Handbook. Cambridge University Press. doi:10.1017/CBO9780511984501.

Storvoll, V., Bjørlykke, K., Mondol, N.H., 2005. Velocity-depth trends in Mesozoic and Cenozoic sediments from the Norwegian Shelf. AAPG Bulletin 89, 359–381. doi:10.1306/10150404033.

Storvoll, V., Brevik, I., 2008. Identifying time, temperature, and mineralogical effects on chemical compaction in shales by rock physics relations. The Leading Edge 27, 750–756. URL: https://doi.org/10.1190/1.2944160, doi:10.1190/1.2944160, arXiv:https://doi.org/10.1190/1.2944160.

Thyberg, B., Jahren, J., Winje, T., Bjørlykke, K., Faleide, J., 2009. From mud to shale: rock stiffening by micro-quartz cementation. First Break 27. doi:https://doi.org/10.3997/1365-2397.2009003.

Torset, S., Holt, R.M., Duffaut, K., 2020. Integrating rock physics laboratory data and modelling to improve uplift characterization methodology. Geophysical Prospecting n/a. URL: https://onlinelibrary.wiley.com/doi/abs/10.1111/1365-2478.12961, doi:10.1111/1365-2478.12961.

Vernik, L., Kachanov, M., 2010. Modeling elastic properties of siliciclastic rocks. GEOPHYSICS 75, E171–E182. URL: https://doi.org/10.1190/1.3494031, doi:10.1190/1.3494031, arXiv:https://doi.org/10.1190/1.3494031.

Walderhaug, O., 1996. Kinetic Modeling of Quartz Cementation and Porosity Loss in Deeply Buried Sandstone Reservoirs. AAPG Bulletin 80, 731–745. URL: http://search.datapages.com/data/doi/10.1306/64ED88A4-1724-11D7-8645000102C1865D, doi:10.1306/64ED88A4-1724-11D7-8645000102C1865D.

Worden, R.H., Burley, S.D., 2009. Sandstone diagenesis: The evolution of sand to stone.

Worsley, D., 2008. The post-caledonian development of svalbard and the western barents sea. Polar Research 27, 298–317. URL: https://doi.org/10.1111/j.1751-8369.2008.00085.x, doi:10.1111/j.1751-8369.2008.00085.x, arXiv:https://doi.org/10.1111/j.1751-8369.2008.00085.x.

Zoeppritz, K., 1919. Erdbebenwellen vii b: über reflexion und durchgang seismischer wellen durch unstetigkeitsflächen. Nachrichten von der Gesellschaft der Wissenschaften zu Göttingen, Mathematisch-Physikalische Klasse 1919, 66–84. URL: http://resolver.sub.uni-goettingen.de/purl?GDZPPN002505290.